Recognizing Molecules and Following Reactions at Interfaces Using the Nonlinear Optical
Techniques Sum Frequency Generation and Second Harmonic Generation

by

Zhiguo Li

A thesis submitted in partial fulfillment of the requirements for the degree of

Doctor of Philosophy

Department of Chemistry

University of Alberta

Abstract

Silica has been widely used as a solid support to generate functionalized silica in material science, which plays important roles in various areas such as catalysis and disease diagnostics. The applications of functionalized silica involve the special molecular properties of interfaces, which can differ from the properties of molecules in bulk phases. Nonlinear optical techniques, including second harmonic generation (SHG) and sum frequency generation (SFG), are a class of well-defined spectroscopic techniques that are well-suited to probe interfacial molecules and to study interfacial phenomena. Owing to their surface specificity, only the molecules that are ordered at the interface are probed in the measurement while interference from molecules in bulk phases is effectively excluded.

Taking planar silica and functionalized planar silica as substrates, this thesis mainly focuses on characterizing the structure and order of molecules at these solid surfaces, and investigating the interaction between immobilized molecules and bulk phase molecules. Specifically, the binding of a model reactant 4-nitroacetophenone with amino and ureido organocatalytic monolayers on silica was investigated at the silica/acetonitrile interface using a combination of SHG and SFG, and the results reveal that the performance of immobilized catalysts is strongly affected by the local environment of surface molecules. Next, the Cu(I)-catalyzed 1,3-dipolar azide-alkyne cycloaddition (CuAAC) was followed at the silica/methanol interface using vibrational SFG; the reaction order with respect to copper catalyst was determined to be 2.1, suggesting that two coppers are involved in the rate-determining step of the interfacial reaction. Using a CuAAC attachment strategy, the thermal evolution of immobilized DNA single strands and duplexes were investigated at the silica/buffer interface using vibrational SFG. Consistent with our SHG work, the melting temperature of the immobilized $T_{15}:A_{15}$ (thymidine 15-mer:

deoxyadenosine 15-mer) duplex at the interface is found to be ~ 12 °C lower than the solution phase melting temperature, indicating immobilization on silica destabilizes the DNA duplex. Finally, as silica is a commonly used stationary phase in chromatography, the organization of acetonitrile molecules at the silica/aqueous interface was studied using vibrational SFG. For a given solution composition, increasing the solution pH is found to effectively decrease the number density of interfacial acetonitrile molecule, which we attribute to the decrease in the number density of surface silanol which can form a hydrogen bond with cyanide within the acetonitrile molecule.

Overall, these results demonstrate the study of interfacial phenomena involving self-assembled monolayers on insulated surfaces like silica using the nonlinear optical techniques SHG and SFG. The combination of these techniques represents a useful approach to explore similar systems in their relevant research areas.

Preface

This thesis is an original work by Zhiguo Li. Some of the research conducted for this thesis forms part of a collaboration with other group members in the Gibbs-Davis group, which will be stated later.

Chapter 2 of this thesis has been published as "Li Z.; Weeraman C. N.; Gibbs-Davis J. M., Ketone Binding at Amino and Ureido Monolayer/Solvent Interfaces Studied by Nonlinear Optical Techniques, *J. Phys. Chem. C*, 2014, *118*, 28662–28670." I was responsible for the data collection and analysis as well as the manuscript composition. Dr. Julianne Gibbs-Davis was the supervisory author.

Chapter 3 of this thesis has been published as "Li Z.; Weeraman C. N.; Gibbs-Davis J. M., Following the Azide-Alkyne Cycloaddition at the Silica/Solvent Interface with Sum Frequency Generation, *ChemPhysChem*, 2014, 15, 2247–2251." I was responsible for the data collection and analysis as well as the manuscript composition. I collaborated with Dr. Champika Weeraman in the preparation of SiO_2 deposited CaF_2 hemisphere. Dr. Julianne Gibbs-Davis was the supervisory author.

Chapter 4 of this thesis has been published as "Li Z.;* Weeraman C. N.;* Azam, M. S.; Osman E.; Gibbs-Davis J. M., The Thermal Reorganization of DNA Immobilized at the Silica/Buffer Interface: A Vibrational Sum Frequency Generation Investigation, *Phys. Chem. Chem. Phys.*, 2015, 17, 12452-12457." I am joint first-author of this paper with Dr. Champika Weeraman. SFG spectra of the thermal revolution of immobilized DNA at the solid/buffer (H_2O) interface were collected by Dr. Champika Weeraman, SFG spectra of immobilized DNA at the

solid/air interface were collected by me, and SFG spectra of immobilized DNA at the solid/buffer (D_2O) interface were collected by Dr. Md Azam. All DNA strands used in this project were synthesized by Eiman Osman or Dr. Weeraman, and the thermal dissociation experiments of DNA duplexes in solution phase were performed by Eiman Osman and me. I was also responsible for SFG spectral fitting, data analysis, and I co-wrote the manuscript with Dr. Julianne Gibbs-Davis.

Chapter 5 of this thesis is an original work by me. No part of this chapter has been previously published. All the SFG spectra were collected by me. I collaborated with Sun Kim in the preparation of acetonitrile/water mixture preparations and pH adjustment.

Acknowledgements

Firstly, I would like to express my sincere gratitude to my advisor Professor Julianne Gibbs-Davis for her patient guidance and precious advice throughout my entire graduate career. I feel honored and privileged to be a member of the Gibbs-Davis research group.

I would like to acknowledge my defense examination committee: Professor Yunjie Xu, Professor Alex Brown, Professor Hongbo Zeng and Professor Rob Walker. I appreciate your valuable suggestions to improve my research.

I would also like to thank all my colleagues in the Gibbs-Davis group, especially Champika Weeraman, Yimeng Li, Abu Kausar, Julian Diaz, Md Azam, Delwar Sikder, Akemi Darlington, Eiman Osman, Safeenaz Mustan, Benjamin Rehl, Sun Kim and Mike Lam. Thanks for your kind help in the daily work.

Finally, I would like to thank my family and all my friends. With your constant and selfless support, I was able to stay focused on research throughout the entire graduate career.

Table of Contents

List of Tables

List of Figures

Chapter 1

Introduction

Portions of this chapter are reproduced with permission from the American Chemical Society

(ACS), Wiley-VCH and the Royal Society of Chemistry (RSC)

1. *"Ketone Binding at Amino and Ureido Monolayer/Solvent Interfaces Studied by Nonlinear Optical Techniques"* **Li Z.**; Weeraman C. N.; Gibbs-Davis J. M, *J. Phys. Chem. C* **2014**, *118*, 28662–28670.

2. *"Following the Azide-Alkyne Cycloaddition at the Silica/Solvent Interface with Sum Frequency Generation"* **Li Z.**; Weeraman C. N.; Gibbs-Davis J. M, *ChemPhysChem* **2014**, *15*, 2247–2251.

3. *"The Thermal Reorganization of DNA Immobilized at the Silica/Buffer Interface: A Vibrational Sum Frequency Generation Investigation"* **Li Z.**;* Weeraman C. N.;* Azam, M. S.; Osman E.; Gibbs-Davis J. M., *Phys. Chem. Chem. Phys.* **2015**, *17,* 12452-12457. (*Joint first-authors.)

1.1 The Functionalized Silica/Liquid Interface

1.1.1 The Importance of Silica and Functionalized Silica

Silica, commonly existing as quartz in nature, is one of the most abundant resources in the world. In chemistry, the most commonly used silica includes fused silica, silica gel and silica colloid. Fused silica, or fused quartz, which is a type of high purity silica in non-crystalline form, has excellent thermal properties and a wide transparency range extending from the UV to the near IR, and consequently, is usually used to make lenses and other optics.[1-3] Silica gel is a type of porous silica granule, which has a strong affinity for water molecules and can be used as desiccant;[4] silica gel is also commonly used as the stationary phase in chromatography.[5] Silica colloid is a type of suspension formed by non-crystalline and nonporous silica particles dispersed in a liquid phase, which can be used as catalyst and absorbent.[6]

Other than these direct applications, silica is also an important solid support to generate functionalized silica owing to its transparency to visible light, cost effectiveness, and stability to water and organic solvents. As a result functionalized silica plays important roles in different areas. In catalysis, catalysts with well-defined structures and reactive sites can be immobilized on silica slides or silica nanoparticles to generate environment-friendly reusable catalysts.[7-11] In particular, mesoporous silica supported enzymes not only retain the biocatalytic activity, but also have increased stability compared with enzymes in solution.[12] Similarly, DNA sequences can be immobilized on planar silica to generate DNA microarray chips, which are effective tools in the diagnosis of multiple diseases.[13-15]

The application of functionalized silica usually involves the special properties of the immobilized molecules, which can differ from the properties of molecules in bulk phases.[16] Indeed, a wide range of molecular properties have been altered when they are present at an

interface.[17] Investigation of these properties will benefit the understanding of interfacial phenomena and allow functionalized silica to be optimized for its different applications.

In the research projects described in this thesis, organic monolayers were prepared on a planar fused silica surface, and the properties of these immobilized molecules at the solid/air and solid/liquid interface, such as structure and orientation, have been characterized using the nonlinear optical techniques second harmonic generation (SHG) and sum frequency generation (SFG). Related thermodynamic and kinetic parameters of processes at the solid/liquid interface were also investigated using nonlinear optical methods.

1.1.2 The Generation of Self-Assembled Monolayers on Planar Silica Surfaces

To functionalize planar silica surfaces, the most convenient and effective way is molecular self-assembly. Self-assembled monolayers of organic molecules are assemblies formed by the adsorption of molecules from solution onto the surface of a solid support.[18-22] Generally, the adsorbate has a special headgroup, which has a strong affinity for the surface of the solid support. The interaction between adsorbate headgroup and the solid surface and the interaction between adsorbates drive the adsorbates to organize spontaneously into an ordered structure. Various headgroups were found to have special binding affinities to metals, mineral oxides, and semiconductors.[19] The most famous example is the binding of thiols on metal surfaces, such as gold, silver, palladium and copper.[19, 23] For a mineral oxide solid support like silica, silanes modified with a leaving group like chloride are the most important headgroup that is used to generate self-assembled monolayers.[23-24]

The generation of self-assembled monolayers on silica surfaces using silanes involves a process called silanization.[23-24] A commonly accepted mechanism for the process of silanization

involves three stages: (1) quick adsorption of a water film on the silica surface; (2) physical adsorption of silane molecules; (3) hydration and polymerization of silane molecules (Figure 1.1).[25-26] As a result, the organofunctional groups in the silane are attached to the silica surface through covalent siloxane bonds (R-Si-O-Si-). Commonly used silanes include methoxysilane, ethoxysilane and chlorosilane, where the presence of the alkoxy group or chloride adjusts reactivity.
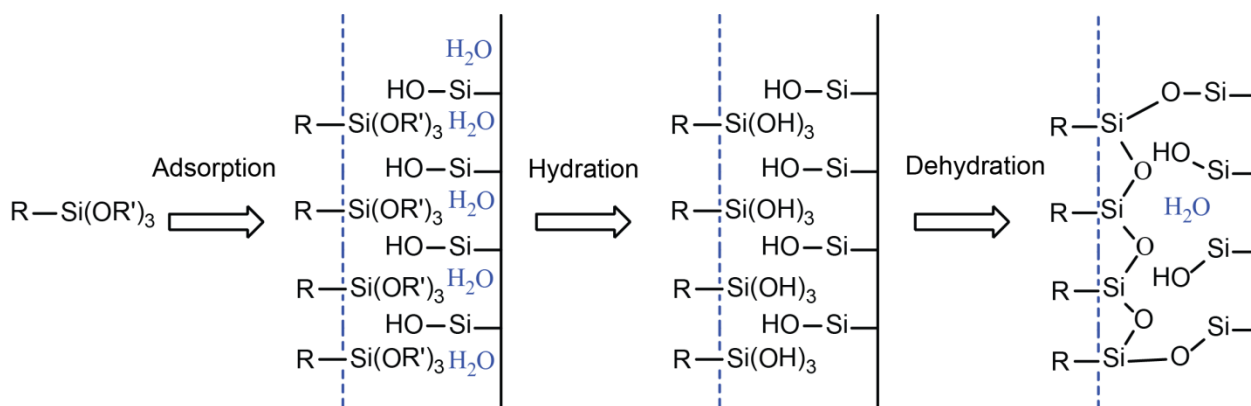
Figure 1.1 A commonly accepted mechanism describing the formation process of self-assembled monolayers through silanization.[25-26] R represents the organofunctional group in the silane molecule.

1.1.3 Characterization of Self-Assembled Monolayers

After surface functionalization, the quality of the self-assembled monolayer on the planar silica is usually characterized by a combination of several surface-sensitive techniques, such as water contact angle measurements, atomic force microscopy (AFM), ellipsometry, and X-ray photoelectron spectroscopy (XPS).

Determination of the contact angle between water and the functionalized silica is the most convenient way to confirm the presence of a new layer on the silica surface.[27] In this measurement, a drop of water with certain volume is placed on the functionalized silica surface,

and the contact angle is measured. If the water contact angle is smaller than 90°, the surface is considered to be hydrophilic; if the water contact angle is larger than 90°, the surface is considered to be hydrophobic. The bare planar silica surface is hydrophilic with a contact angle of ~ 10°;[28-29] however, after self-assembling a monolayer, the surface usually has an increased water contact angle.[28] So an apparent difference can be observed by measuring water contact angle before and after surface functionalization.

Atomic force microscopy (AFM) is often used in characterizing the morphology and roughness of planar surfaces.[30] The key unit of the AFM microscope is a cantilever with a tiny sharp tip at its end, which is usually made of silicon and used to scan the surface. When the cantilever closely approaches the functionalized surface (< 200 nm typically), forces between the sharp tip and the surface will lead to a deflection of the cantilever.[30] This deflection is recorded using a laser spot reflected from the top of the cantilever surface into photodiodes while scanning the tip over a certain area on the sample. Consequently, an image of the sample surface will be achieved, and from this the surface roughness can be calculated. For self-assembly formed by silanization, the appearance of the surface varies with the depositing conditions, such as identity and concentration of silane, composition of solvent, depositing time and temperature.[31-34] Normally, the surface roughness of a well-formed monolayer should have similar amplitude as the molecular dimension. The generation of a well-formed monolayer is the starting point of most research focused on interfacial phenomena, and therefore optimization of depositing conditions has to be done using the AFM results as a guide.

Ellipsometry is a well-defined optical technique that can be used to determine the thickness of the surface layer.[35] In ellipsometry, polarized light is shone on the sample surface, and the reflected light is collected using an analyzer and a detector. As the surface layer has different

dielectric properties than the solid support, there will be a change in the polarization of the reflected light. After acquiring the data, the change of polarization will be modeled and information about the thickness and optical constants of the surface layer can be extracted.

X-ray photoelectron spectroscopy (XPS) is a quantitative spectroscopic technique that measures the elemental composition of a surface.[36] In XPS, an X-ray beam is used to irradiate the sample surface. Electrons within the surface atoms absorb energy from the X-ray and are ejected from the surface. The kinetic energy and number of these electrons are recorded. The difference between the energy of the X-ray, which has a fixed wavelength, and the kinetic energy of the ejected electrons is equal to the binding energy of electrons in the particular chemical environment. Element identity, the number ratio of atoms and the atomic chemical environment are the most common information extracted from XPS measurements.

1.1.4 Study of Processes at Solid/Liquid Interfaces

At the buried solid/liquid interface, following interfacial processes is difficult, as the number of applicable surface analytical techniques is limited. Electron-based techniques are not applicable, as electrons cannot penetrate the buried bulk phase to reach the interface; at the same time, as silica is an insulator, commonly used surface plasmon resonance and electrochemical methods are not applicable either.

Fortunately, photon-based techniques are usually applicable, if the used light is transmissive in the bulk phase resulting in no strong absorption during light penetration. For example, IR absorbance,[37-41] Raman[42-44] and fluorescence [45-47] spectroscopy have been employed to study the properties of interfacial molecules and to follow interfacial processes in real-time. However, a disadvantage of these techniques is they cannot distinguish between interfacial molecules and

bulk molecules, so the expected signal from the interface cannot exclude possible contributions from the bulk phase.

Nonlinear optical techniques, including SHG and SFG, are a class of powerful techniques that can readily solve this trouble. They are surface-specific and are well suited to follow processes that proceed at a variety of interfaces.[48-54]

1.1.5 Advantages of Nonlinear Optical Techniques

SHG and SFG are two types of nonlinear optical processes. In SFG, two laser beams, usually of different frequencies of light, are overlapped spatially and temporally on the interface formed by two media. Two photons (one from each beam) interacting with interfacial molecules with net orientation are combined to generate a new photon, whose frequency is the sum of the original two; SHG is a special case of SFG, in which the two photons come from the same laser beam and have the same frequency.

There are many advantages of the nonlinear optical techniques second harmonic generation (SHG) and sum frequency generation (SFG). First of all, as mentioned earlier, they are surface-specific, only interfacial molecules with a certain net orientation can contribute to the signal; at the same time, they are orientation-sensitive, if the orientation of interfacial molecules changes, the signal from interface changes accordingly. Consequently, resonant-enhanced SHG has been used to study the binding affinity and mode of binding for adsorbates in solution with surfaces. Secondly, minimal labeling is needed in SHG and SFG. For SHG, resonant SHG is usually used to probe electronic transitions within interfacial molecules or atoms. When the frequency of the incident fundamental light and/or the frequency of the generated SHG light is close to one of the electronic transitions within the molecule or atom, resonance-enhanced SHG can be detected.

For non-resonant SHG, the $\chi^{(3)}$ method has been well developed to study the change of interfacial potential resulting from surface charge.[50, 55-56] In contrast, SFG is usually used to probe vibrational transitions within interfacial molecules. SFG can be generated if the interfacial molecule has a vibrational mode that is both IR and Raman active and exhibits net orientation.[57] Finally, both SHG and SFG can follow processes at various interfaces in real-time. By using time-resolved SFG and pump-probe SFG, information about vibrational dynamics and reaction dynamics also can be extracted.[58-60]

1.2 Second Harmonic Generation (SHG)

1.2.1 Reflection and Refraction of Light at an Interface

An interface is formed by two different materials or two different phases of the same material; in both cases the two phases have different refractive indices. When light arrives at an interface, interactions between the incoming light and the material include absorption, scattering (elastic and inelastic), reflection and refraction. Figure 1.2A shows the reflection and refraction of light at an interface. According to the law of reflection, the angle of incidence equals the angle of reflection, and the angle of refraction is determined by the refractive index of both phases and the angle of incidence through Snell's law.[61] Specially, when light travels from an optically dense medium with a relatively large refractive index, to an optically thin medium with a relatively small refractive index, the angle of refraction is always larger than the angle of incidence. When the angle of incidence equals the so-called critical angle, as shown in Figure 1.2B, the refracted beam will travel along the boundary between the two media. At angles of incidence larger than this critical angle, total internal reflection will happen, and there is no refraction beam.
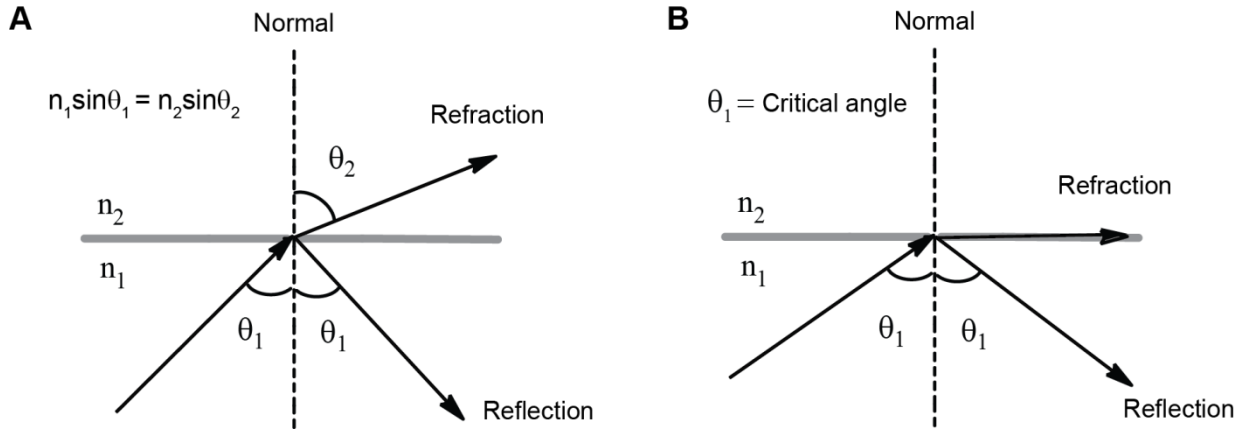
Figure 1.2 (A) The reflection and refraction of light at an interface. The angle of reflection equals the angle of incidence, and the angle of refraction is governed by Snell's law. n_1 and n_2 represent the refractive index of a material with greater and lesser optical density, respectively. (B) The reflection and refraction of light at the critical angle. The refracted beam travels along the boundary between the two media.

1.2.2 Induced Polarization upon the Interaction of Light with Medium

As electromagnetic radiation, light can induce a polarization when it interacts with an material. When the electric field of the light is weak, the response of the material system to the field depends in a linear manner on the strength of the field; however, when the electric field of light becomes strong, the dependence of the response on the strength of the field becomes nonlinear. Generally, in an applied electric field E, the induced polarization of a system, P, can be written as a power series in E:[61-64]

$$P = P^{(1)} + P^{(2)} + P^{(3)} + ...$$
$$= \varepsilon_0 \left(\chi^{(1)} E + \chi^{(2)} EE + \chi^{(3)} EEE + ... \right)$$

$$(1.1)$$

where $P^{(1)}$ is the linear polarization, $P^{(i)}$ ($i = 2, 3...$) is the ith-order nonlinear polarization and $\chi^{(i)}$ is the ith-order susceptibility of the system. In the equation, $P^{(1)}$ is related to linear optical effects, and the higher order terms are related to nonlinear optical effects. For example, the

9

second-order susceptibility $\chi^{(2)}$ describes processes such as second harmonic generation (SHG) and sum frequency generation (SFG), which will be discussed in the thesis, and the third-order susceptibility $\chi^{(3)}$ describes processes such as coherent anti-stokes Raman spectroscopy (CARS) and coherent anti-Stokes two-photon spectroscopy (CATS).[65]

1.2.3 Theoretical Background for SHG

SHG is a typical example of nonlinear optical processes, in which two photons with the same frequency interacting with a nonlinear crystal or interface are combined to generate new photons with twice the frequency. Under the electric-dipole approximation, SHG is only allowed in a non-centrosymmetric environment.[54, 62, 64] In other words, for a medium within which for every point (X, Y, Z) there is an indistinguishable point (-X, -Y, -Z), SHG is not allowed. This property can be easily understood from the following line of reasoning:[64] SHG is related to the second-order susceptibility $\chi^{(2)}$ through the equation $P^{(2)} = \chi^{(2)}EE$, where the intensity of SHG is proportional to the square of $P^{(2)}$. For a centrosymmetric system, the electric field and induced polarization transform as $E \rightarrow$ -E and $P \rightarrow$ -P under the action of inversion. However, according to the principle of Neumann, as a physical property of a centrosymmetric system, the sign and magnitude of $\chi^{(2)}$ should not change after the transformation,[64] i.e., $\chi^{(2)} \rightarrow \chi^{(2)}$. So $P^{(2)} = \chi^{(2)}EE$ transform into $-P^{(2)} = \chi^{(2)}(-E)(-E)$ and $\chi^{(2)}$ must be zero.

Figure 1.3A illustrates the geometry of SHG generated at an interface for reflection geometry. SHG is generated in both the reflection beam and refraction beam, and therefore the SHG signal can be collected in either beam depending on the experimental set-up. Figure 1.3B shows the energy level diagram describing SHG. In the diagram, the solid line represents the

ground state within the atom or molecule present at the interface, and the dashed lines represent virtual levels. These virtual levels are not energy eigenlevels of the atom or molecule, but represent the combined energy of one of the energy eigenstates and one or more photons of the radiation field.[62]
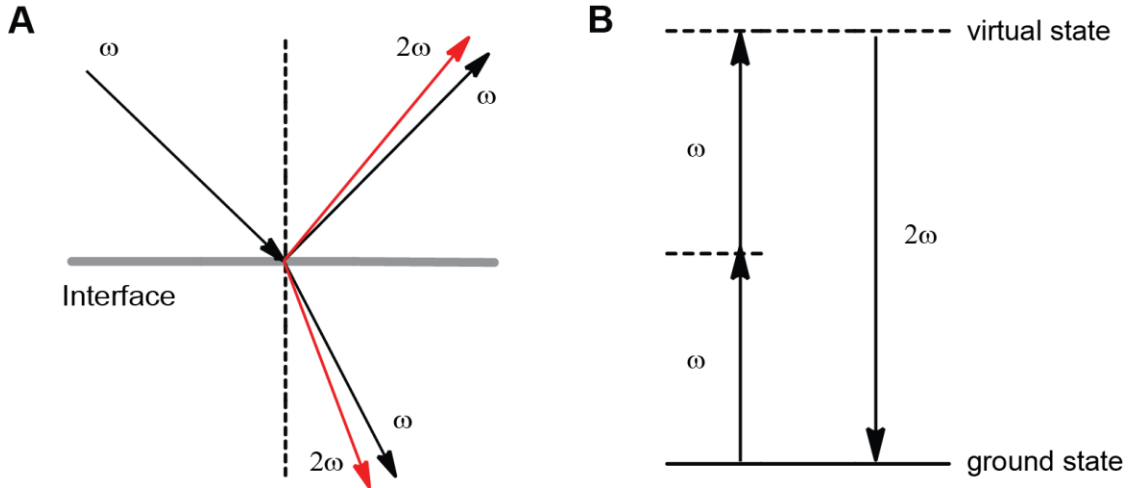
Figure 1.3 (A) Geometry of SHG generated at an interface. SHG is generated in both the reflected beam and refracted beam. (B) Energy level diagram describing non-resonant SHG. Solid line represents the atomic or molecular ground state, and dashed lines represent virtual states.

The second-order nonlinear susceptibility, $\chi^{(2)}$, is a third order tensor, which has 27 tensor elements. The relationship between the induced second-order polarization and the second-order nonlinear susceptibility can be expressed in another manner, which highlights the tensor property of $\chi^{(2)}$.[54] As shown in equation 1.2, IJK represent the Cartesian coordinates in the laboratory frame, $P_I^{(2)}$ is the component of the induced polarization vector along the I direction, E_J is the component of the incident electric field vector along the J direction, and $\chi_{IJK}^{(2)}$ is an element of

11

the susceptibility tensor. For SHG, the magnitude of $\chi^{(2)}_{IJK}$ describes the efficiency of generating

I-polarized SHG for driving electric fields polarized along the *J* and *K* laboratory axes.

$$P^{(2)}_I = \sum_{J,K} \chi^{(2)}_{IJK} E_J E_K \qquad (1.2)$$

For a rotationally isotropic interface formed by a silica hemisphere in contact with a liquid phase in a sample cell, the symmetry of the interface is C$_{\infty v}$, and the laboratory coordinate system is defined as shown in Figure 1.4. Specifically, the surface normal is defined as the laboratory *Z* direction, and the other two axes *X* and *Y* lie in the interface plane, which is perpendicular to surface normal.
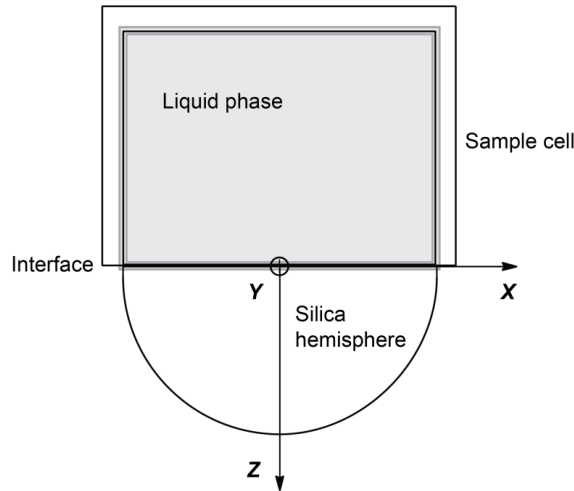
Figure 1.4 A rotationally isotropic interface formed by a silica hemisphere and a liquid phase in sample cell. Laboratory coordinate frame *X, Y* and *Z* are defined as shown in the diagram.

Although $\chi^{(2)}$ has 27 tensor elements, only a small quantity of them are non-zero due to the symmetry of the interface. All the tensor elements can be examined by imposing the symmetry element to the system using the following method.[64]

For example, if plane XZ is one of the mirror planes of the interface, then the interface is indistinguishable under the reflection of plane XZ. Imposing mirror plane XZ to the system, the coordinates transform as:

$X \rightarrow X, Y \rightarrow - Y, Z \rightarrow Z$

Similarly, the electric field and induced polarization components transform as:

$E_X \rightarrow E_X, E_Y \rightarrow - E_Y, E_Z \rightarrow E_Z$

$P_X \rightarrow P_X, P_Y \rightarrow - P_Y, P_Z \rightarrow P_Z$

For tensor element $\chi_{YYY}^{(2)}$, under the operation of reflection through the XZ plane, $P_Y^{(2)} = \chi_{YYY}^{(2)} E_Y E_Y$ transforms into $\left(-P_Y^{(2)}\right) = \chi_{YYY}^{(2)}\left(-E_Y\right)\left(-E_Y\right) = \chi_{YYY}^{(2)} E_Y E_Y$ indicating $\chi_{YYY}^{(2)}$ has to be zero.

$$
\begin{bmatrix}
\chi_{XXX} & \chi_{XXY} & \chi_{XXZ} & \chi_{XYX} & \chi_{XYY} & \chi_{XYZ} & \chi_{XZX} & \chi_{XZY} & \chi_{XZZ} \\
\chi_{YXX} & \chi_{YXY} & \chi_{YXZ} & \chi_{YYX} & \chi_{YYY} & \chi_{YYZ} & \chi_{YZX} & \chi_{YZY} & \chi_{YZZ} \\
\chi_{ZXX} & \chi_{ZXY} & \chi_{ZXZ} & \chi_{ZYX} & \chi_{ZYY} & \chi_{ZYZ} & \chi_{ZZX} & \chi_{ZZY} & \chi_{ZZZ}
\end{bmatrix}
$$

$\xrightarrow{\text{Examine symmetry}}$
$$
\begin{bmatrix}
0 & 0 & \chi_{XXZ} & 0 & 0 & 0 & \chi_{XZX} & 0 & 0 \\
0 & 0 & 0 & 0 & 0 & \chi_{YYZ} & 0 & \chi_{YZY} & 0 \\
\chi_{ZXX} & 0 & 0 & 0 & \chi_{ZYY} & 0 & 0 & 0 & \chi_{ZZZ}
\end{bmatrix}
$$

$\xrightarrow{\text{Indistinguishable X and Y}}$
$$
\begin{bmatrix}
0 & 0 & \chi_{XXZ} & 0 & 0 & 0 & \chi_{XZX} & 0 & 0 \\
0 & 0 & 0 & 0 & 0 & \chi_{XXZ} & 0 & \chi_{XZX} & 0 \\
\chi_{ZXX} & 0 & 0 & 0 & \chi_{ZXX} & 0 & 0 & 0 & \chi_{ZZZ}
\end{bmatrix}
$$

Figure 1.5 The 3×9 matrix describing the second-order susceptibility $\chi^{(2)}$ of an interface. The matrix is much simplified when the interface is highly symmetric such as possessing $C_{\infty v}$ symmetry.

Using the same method by imposing all symmetry elements to the interface, one can determine all non-zero tensor elements of the interface. As shown in Figure 1.5, for a rotationally

isotropic interface with symmetry of C$_{\infty v}$, there are only seven non-zero tensor elements for the second-order susceptibility. When the *X* and *Y* axis are indistinguishable (the interface possesses a σ$_{xy}$ mirror plane), there are only four independent non-zero tensor elements left, which are $\chi_{ZZZ}^{(2)}, \chi_{XXZ}^{(2)} = \chi_{YYZ}^{(2)}, \chi_{XZX}^{(2)} = \chi_{YZY}^{(2)}$ and $\chi_{ZXX}^{(2)} = \chi_{ZYY}^{(2)}$.[62-64] By determining which tensor elements contribute to the observed second-order response, information about the orientation of molecules at the interface can be explored.

1.2.4 Resonant Enhanced SHG

At an interface, the intensity of generated SH light is proportional to the square of the induced second-order polarization, as described in the following equation:

$$I_{2\omega} \propto |P_{2\omega}|^2 = |\chi^{(2)}|^2 I_\omega I_\omega \qquad (1.3)$$

where $I_{2\omega}$ is the intensity of SHG light generated at the interface, $P_{2\omega}$ is the induced second-order polarization and I_ω is the intensity of the incident fundamental light.

As mentioned earlier, there are two intermediate virtual levels in the non-resonant SHG process, and corresponding transition frequencies from the electronic ground state to each level are ω and 2ω, respectively. If one or both of these two frequencies are close to the frequencies of any electronic transitions within the interfacial species, $\chi^{(2)}$ becomes large, and the intensity of generated SHG light will be strongly enhanced. In this case, it is called electronically resonant SHG. Depending on which frequency is in resonance with a molecular or atomic electronic transition, there are three types of resonant SHG as shown in Figure 1.6.
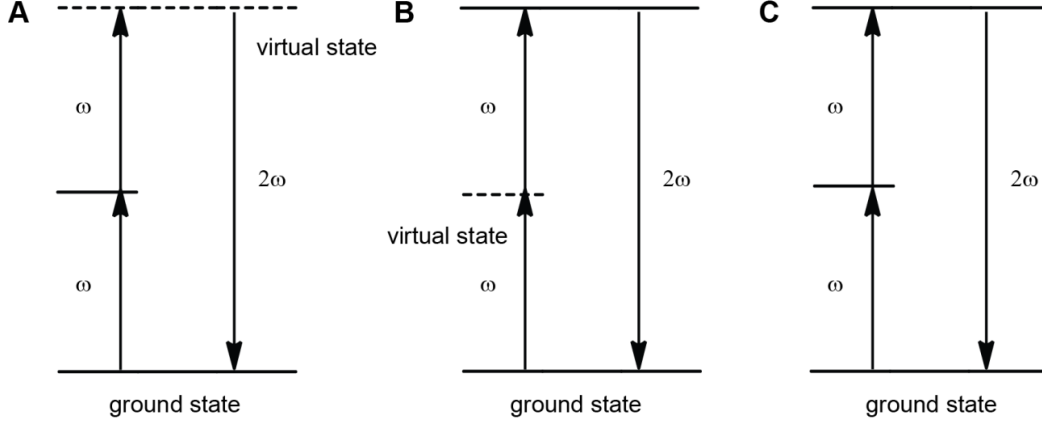
Figure 1.6 Energy diagrams for three types of electronically resonant SHG. Solid line represents an eigenstate within the interfacial molecule or atom, and a dashed line represents a virtual state.

As shown in equation 1.4, in resonant SHG, the second-order nonlinear susceptibility $\chi^{(2)}$ is usually broken into two components: one resonant component $\chi_R^{(2)}$, which comes from the interfacial species in resonance, and one non-resonant component $\chi_{NR}^{(2)}$, which comes from all the other interfacial species not in resonance. $\chi_R^{(2)}$ is much larger than $\chi_{NR}^{(2)}$, and can be related to the molecular hyperpolarizability of the interfacial molecule through equation 1.5.[50, 54]

$$\chi^{(2)} = \chi_{NR}^{(2)} + \chi_R^{(2)} \tag{1.4}$$

$$\chi_R^{(2)} = N\left\langle \beta^{(2)} \right\rangle \tag{1.5}$$

In equation 1.5, N is the number density of interfacial molecules, $\beta^{(2)}$ is the molecular hyperpolarizability of interfacial molecules, and the bracket represents an orientationally averaged value. Similar to $\chi_R^{(2)}$, $\beta^{(2)}$ is also a third-order tensor and has 27 tensor elements, which are defined in the molecular coordinate system. Therefore, Euler transformation is needed

for correlating the molecular coordinate system and the laboratory coordinate system, which will be discussed later.

In resonant SHG, for a certain incident fundamental light and a well-defined interface, the intensity of generated SHG light is mainly determined by two factors: the number density and the net orientation of interfacial molecules. Consequently, SHG is usually used to collect information about these two aspects of an interfacial process.

1.2.5 Orientation Analysis Using Resonant SHG

The molecular hyperpolarizability, $\beta^{(2)}$, is a third-order tensor with tensor elements of $\beta_{ijk}^{(2)}$ ($i, j, k = x, y, z$), where x, y and z represent axes in the molecular coordinate system. Similar to $\chi^{(2)}$, the magnitude of each $\beta_{ijk}^{(2)}$ element describes the efficiency of generating i-polarized SHG from a given molecule with driving electric fields along the j and k molecular axes.[66] Although $\beta^{(2)}$ has 27 tensor elements, highly symmetric molecules usually have a limited number of non-zero tensor elements.

As mentioned, an Euler transformation is needed to correlate the molecular coordinate system (xyz) and the laboratory coordinate system (XYZ). Three Euler angles: the in-plane rotation angle ϕ, tilt angle θ and twist angle ψ, are defined as shown in Figure 1.7.[67] It has to be noted that, different definitions of these Euler angles will lead to a different Euler transformation matrix.[67-68] Using the definition in Figure 1.7, the Euler transformation matrix R correlating the molecular coordinate system (xyz) and the laboratory coordinate system (XYZ) can be written as the following:[67]

$$R = \begin{bmatrix} -\sin\psi\sin\phi + \cos\theta\cos\psi\cos\phi & -\cos\psi\sin\phi - \cos\theta\sin\psi\cos\phi & \sin\theta\cos\phi \\ \sin\psi\cos\phi + \cos\theta\cos\psi\sin\phi & \cos\psi\cos\phi - \cos\theta\sin\psi\sin\phi & \sin\theta\sin\phi \\ -\sin\theta\cos\psi & \sin\theta\sin\psi & \cos\theta \end{bmatrix} \quad (1.6)$$

as defined in:

$$\begin{bmatrix} X \\ Y \\ Z \end{bmatrix} = R \times \begin{bmatrix} x \\ y \\ z \end{bmatrix} = \begin{bmatrix} R_{Xx} & R_{Xy} & R_{Xz} \\ R_{Yx} & R_{Yy} & R_{Yz} \\ R_{Zx} & R_{Zy} & R_{Zz} \end{bmatrix} \times \begin{bmatrix} x \\ y \\ z \end{bmatrix} \quad (1.7)$$
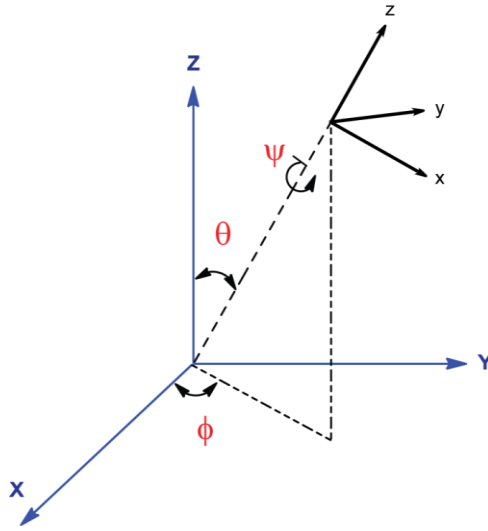
Figure 1.7 Three Euler angles (in-plane rotation angle ϕ, tilt angle θ and twist angle ψ) correlating the molecular coordinate system (xyz) and the laboratory coordinate system (XYZ).[67]

To describe the relationship between the second-order nonlinear susceptibility tensor $\chi_R^{(2)}$ and the molecular hyperpolarizability tensor $\beta^{(2)}$, equation 1.5 can be written in a further expression:[49, 54, 69-70]

$$\chi_{IJK}^{(2)} = N \sum_{ijk} \langle R_{Ii} R_{Jj} R_{Kk} \rangle \beta_{ijk}^{(2)} \quad (1.8)$$

where R_{Ii}, R_{Jj} and R_{Kk} are the corresponding elements of the Euler transformation matrix.

In a typical SHG study, orientation analysis of an interfacial molecule refers to the determination of ϕ, θ and ψ. In order to achieve this, polarization-dependent SHG measurements have to be done in which both the *p*-polarized and *s*-polarized SHG signal intensities are recorded as a function of polarization rotation angle of the incident fundamental light.
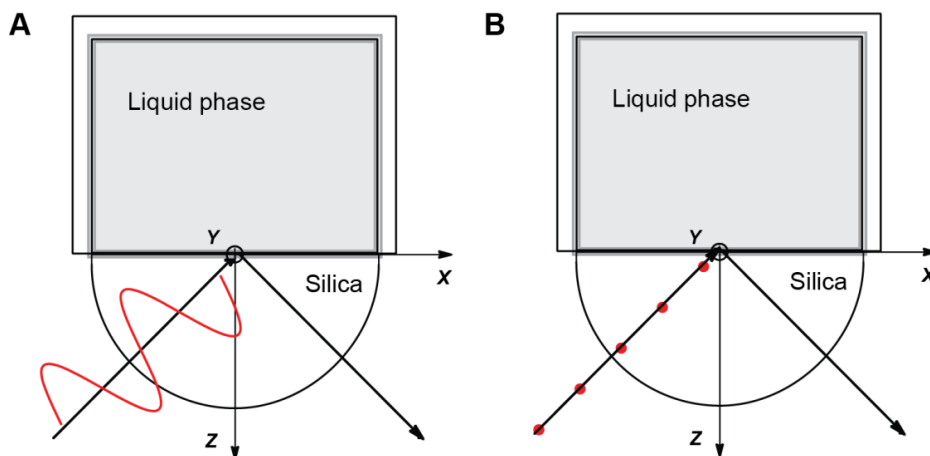
Figure 1.8 Definition of *p*-polarized light (A) and *s*-polarized light (B). The electric field is depicted in red and the propagation direction of the light reflected at the interface is shown in black. For p-polarized light, the oscillating direction of the electric field is parallel to the incidence plane *XZ*; for s-polarized light, the oscillating direction of the electric field is perpendicular to the incidence plane *XZ*.

The polarization of light is defined based on the relationship between the direction of the oscillating electric field of light and the incidence plane. As shown in Figure 1.8, the incidence plane (plane *XZ*) is formed by the surface normal and the light propagating direction. If the oscillating direction of the electric field is parallel to the *XZ* plane, the light is defined to be p-polarized with electric field components along both the *X* axis and *Z* axis (Figure 1.8A); if the oscillating direction of the electric field is perpendicular to the *XZ* plane, the light is defined to be s-polarized and has an electric field component only along the *Y* axis (Figure 1.8B).

The most common case of orientation analysis using resonant SHG involves a rotationally isotropic interfacial layer formed by the adsorption of self-assembly of a SHG-active molecule. For these systems, the following assumptions are made:[54, 71-72] (i) assume the generated SHG light is in resonance with an electronic transition within the interfacial molecule and the resonant transition dipole moment lies parallel to the long molecular axis z; (ii) assume the molecular hyperpolarizability tensor is dominated by a single component along the long molecular axis z (i.e. $\beta_{zzz}^{(2)}$ dominates $\beta^{(2)}$); (iii) assume the molecule exhibits a uniform random distribution in ϕ and ψ, so only one orientation parameter θ is left to be determined. With these assumptions, only three unique non-zero second-order nonlinear susceptibility tensor elements remain, and they are $\chi_{ZZZ}^{(2)}$, $\chi_{XXZ}^{(2)}\left(= \chi_{XZX}^{(2)}\right)$ and $\chi_{ZXX}^{(2)}$,[64, 69, 73] which can be written in the following simplified expressions:[50, 71, 74-75]

$$\chi_{ZZZ}^{(2)} = N\left\langle\cos^3\theta\right\rangle\beta_{zzz}^{(2)} \tag{1.9}$$

$$\chi_{XXZ}^{(2)} = \chi_{ZXX}^{(2)} = \frac{1}{2}N\left\langle\cos\theta\sin^2\theta\right\rangle\beta_{zzz}^{(2)} \tag{1.10}$$

The relative amplitude of $\chi_{ZZZ}^{(2)}$, $\chi_{XXZ}^{(2)}$ and $\chi_{ZXX}^{(2)}$ can be determined by fitting p-polarized and s-polarized SHG intensity as a function of rotation angle of the incident light using the following equations:[69, 71-73, 76]

$$I_s^{2\omega}(\gamma) = C\left|s_1\sin(2\gamma)\chi_{XXZ}^{(2)}\right|^2\left(I^\omega\right)^2 \tag{1.11}$$

$$I_p^{2\omega}(\gamma) = C\left|s_5\chi_{ZXX}^{(2)} + \cos^2\gamma\left(s_2\chi_{XXZ}^{(2)} + s_3\chi_{ZXX}^{(2)} + s_4\chi_{ZZZ}^{(2)} - s_5\chi_{ZXX}^{(2)}\right)\right|^2\left(I^\omega\right)^2 \tag{1.12}$$

19

where $I^{2\omega}$ is the intensity of the measured p-polarized or s-polarized SHG light, I^{ω} is the intensity of the incident fundamental light; s_{λ} (λ = 1, 2, 3, 4, 5) are constants related to the Fresnel coefficient (the expressions for Fresnel coefficient will be discussed later) and the incident angles of lights; γ is the polarization rotation angle of the incident light with $\gamma = 0°$ for p-polarized light and $\gamma = \pm 90°$ for s-polarized light.

After extracting the relative amplitude of the three unique non-zero second-order nonlinear susceptibility tensor elements, θ can be determined using equation 1.9 and 1.10. One point that needs to be highlighted here is equations 1.9 – 1.12 are not general, and are only qualified under the previously mentioned assumptions. Actually, the expressions for non-zero susceptibility tensor elements are very complicated.[67] One needs to make appropriate symmetry considerations and consider the angular average to obtain the expressions as the linear combination of non-zero molecular hyperpolarizability tensor elements. The values of non-zero molecular hyperpolarizability tensor elements are usually obtained by computational simulation[77-79] and other measurements.[80]

1.3 Sum Frequency Generation (SFG)

1.3.1 Theoretical Background for SFG

SFG is another type of nonlinear optical process. Similar to SHG, under the electric-dipole approximation, SFG is only allowed in non-centrosymmetric environments.[54, 62, 64] Figure 1.9A shows the geometry of SFG generated in the reflection beam at an interface. SFG is generated in both the reflection beam and refraction beam, and therefore SFG spectra can be collected in

either beam depending on the experimental set-up. Figure 1.9B illustrates the energy level diagram describing SFG. In the diagram, the solid line represents the ground state of the molecules at the interfaces and the dashed lines represent virtual states.
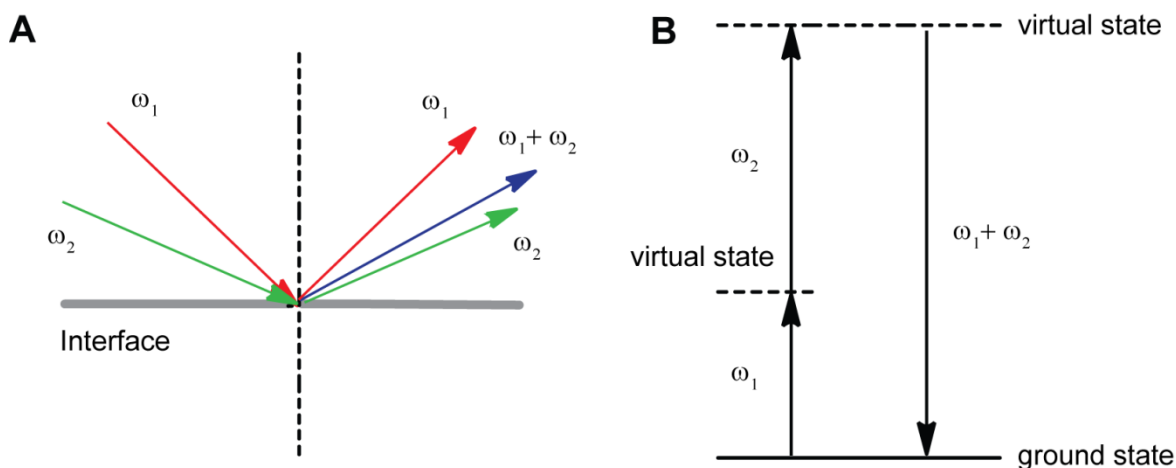
Figure 1.9 (A) Geometry of SFG generated in the reflection beam at an interface. SFG signal is generated in both the reflected beam and refracted beam. (B) Energy level diagram describing SFG. Solid line represents an atomic or molecular ground state, and dashed lines represent virtual states.

1.3.2 Resonant Vibrational SFG

SFG is typically used to probe vibrational signatures of molecules. In resonant SFG, one of the incident beams is usually set to have a fixed wavelength within the visible range (e.g. 800 nm), which is not in resonance with the interfacial molecule, and the other beam is set to have a frequency within the IR range, which is in resonance with certain vibrational modes within the interfacial molecule. As shown in Figure 1.10, in resonant vibrational SFG, one of the virtual levels becomes a real vibrational level. Scanning the IR frequency will achieve a SFG spectrum, and the SFG signal intensity is usually plotted versus IR frequency to highlight the position of the vibrational mode.
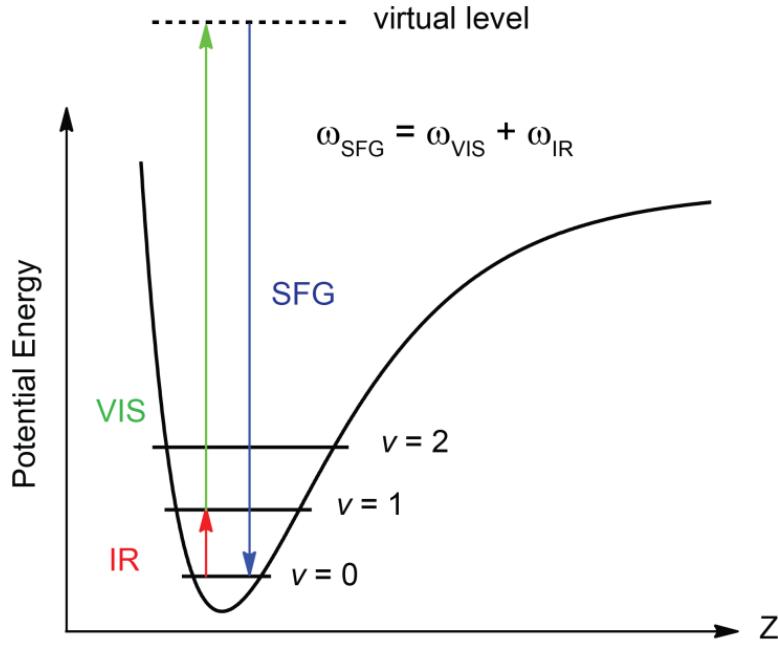
Figure 1.10 Resonant SFG probing vibrational signatures within interfacial molecule. In vibrational SFG, the visible wavelength/frequency is fixed, and the IR frequency can be scanned. When the IR frequency is close to one of the vibrational transitions within the interfacial molecule, there is an enhancement in SFG signal.

The intensity of the SF signal, I_{SFG}, is described in the following equation:

$$I_{SFG} \propto \left| \chi^{(2)} \right|^2 I_{vis} I_{IR} \tag{1.13}$$

where I_{vis} and I_{IR} are the intensities of the incident visible and IR beams, respectively. As in SHG, $\chi^{(2)}$ represents the second-order nonlinear susceptibility of the interface, which can be further expressed as:[81-84]

$$\chi^{(2)} = \chi^{(2)}_{NR} + \sum_v \chi^{(2)}_R = \chi^{(2)}_{NR} + \sum_v \frac{A_v}{\omega_{IR} - \omega_v + i\Gamma_v} \tag{1.14}$$

22

where $\chi_{NR}^{(2)}$ and $\chi_{R}^{(2)}$ are the non-resonant and resonant contributions to the second-order nonlinear susceptibility. $\chi_{R}^{(2)}$ can be expressed as a summation over all frequencies (v) with ω_{IR} as the frequency of the IR beam. A_v, ω_v and Γ_v are the amplitude, frequency, and damping coefficient of the vth surface vibrational mode, respectively. The sign of the amplitude A_v can be either positive or negative, depending on the direction of the transition dipole moment of the corresponding mode.[85]

The resonant second-order nonlinear susceptibility $\chi_{R}^{(2)}$ can be also related to the number density of interfacial molecule (N) and the orientationally averaged molecular hyperpolarizability ($\langle \beta^{(2)} \rangle$) through the following equation:[50, 54]

$$\chi_{R}^{(2)} = N \langle \beta^{(2)} \rangle \qquad (1.15)$$

Similar to SHG, for certain incident visible and IR lights and a well-defined interface, the intensity of generated SFG light is mainly determined by two factors: the number density and the net orientation of interfacial molecules. Additionally, if we assume the orientation of interfacial molecules do not change much throughout adsorption or other interfacial processes, when the IR frequency (ω_{IR}) is the same as the central frequency of a vibrational mode (ω_v), the ratio A_v / Γ_v (or the amplitude A_v itself, if the damping coefficient Γ_v does not change) is directly proportional to the number density of molecular oscillators that are ordered at the interface. Consequently, changes in the SFG intensity and in turn $\chi_{R}^{(2)}$ can be directly related to the disappearance or appearance of interfacial molecules.

1.3.3 Polarization-Resolved SFG

For a rotationally isotropic interface with the symmetry of C∞v, there are only seven non-zero second-order nonlinear susceptibility tensor elements. By taking polarization-resolved SFG spectra, the relative amplitude of these tensor elements can be obtained.

There are only four polarization combinations with notations of *ppp*, *ssp*, *sps* and *pss*, respectively, for which SFG is effectively generated.[86] In this type of polarization notation, the polarizations of SFG light, visible light and IR light are arranged by the order of decreasing energy. For example, *sps* polarization refers to *s*-polarized SFG, *p*-polarized visible light and *s*-polarized IR light.

Under a certain polarization combination, only some of the non-zero second-order nonlinear susceptibility elements are probed. For example, under polarization combination *sps*, based on the laboratory coordinate system defined in Figure 1.4, the electric field of the incident IR light is only polarized along the Y axis, the electric field of visible light has components polarized along both the X axis and Z axis, and the collected SFG light is only polarized along the Y axis. So only two susceptibility tensor elements, $\chi_{YXY}^{(2)}$ and $\chi_{YZY}^{(2)}$, are possible candidates to be probed; however, $\chi_{YXY}^{(2)}$ is zero for a rotationally isotropic interface with the symmetry of C∞v. Consequently, only one susceptibility tensor element $\chi_{YZY}^{(2)}$ is actually probed under the *sps* polarization combination.
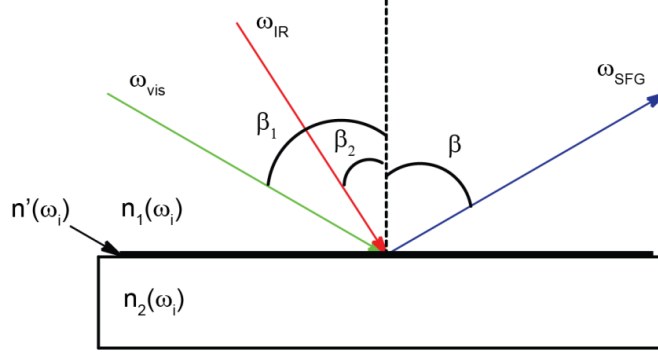
Figure 1.11 Schematic representation of SFG in reflection geometry from an isotropic achiral layer formed at the interface of medium 1 and medium 2. β, β_1 and β_2 are angles between the surface normal and the SFG beam, visible beam and IR beam, respectively. Frequency-dependent n_1, n_2 and n' are the refractive indices of the light in medium 1, medium 2 and the interfacial layer, respectively.

As shown in Figure 1.11, visible light (with incident angle of β_1) and IR light (with incident angle of β_2) are spatially and temporally overlapped on an interfacial layer, and the SFG light (with reflected angle of β) is generated in the reflection. The expressions for the effective second-order nonlinear susceptibility, $\chi_{eff}^{(2)}$, under different polarization combinations are readily derived and shown in the following equations:[49, 87]

$$\chi_{eff}^{(2),\ ssp} = L_{YY}(\omega_{SFG})L_{YY}(\omega_{vis})L_{ZZ}(\omega_{IR})\sin\beta_2\chi_{YYZ}^{(2)}$$

$$\chi_{eff}^{(2),\ sps} = L_{YY}(\omega_{SFG})L_{ZZ}(\omega_{vis})L_{YY}(\omega_{IR})\sin\beta_1\chi_{YZY}^{(2)}$$

$$\chi_{eff}^{(2),\ pss} = L_{ZZ}(\omega_{SFG})L_{YY}(\omega_{vis})L_{YY}(\omega_{IR})\sin\beta\chi_{ZYY}^{(2)}$$

$$\begin{aligned}\chi_{eff}^{(2),\ ppp} = &-L_{XX}(\omega_{SFG})L_{XX}(\omega_{vis})L_{ZZ}(\omega_{IR})\cos\beta\cos\beta_1\sin\beta_2\chi_{XXZ}^{(2)}\\ &-L_{XX}(\omega_{SFG})L_{ZZ}(\omega_{vis})L_{XX}(\omega_{IR})\cos\beta\sin\beta_1\cos\beta_2\chi_{XZX}^{(2)}\\ &+L_{ZZ}(\omega_{SFG})L_{XX}(\omega_{vis})L_{XX}(\omega_{IR})\sin\beta\cos\beta_1\cos\beta_2\chi_{ZXX}^{(2)}\\ &+L_{ZZ}(\omega_{SFG})L_{ZZ}(\omega_{vis})L_{ZZ}(\omega_{IR})\sin\beta\sin\beta_1\sin\beta_2\chi_{ZZZ}^{(2)}\end{aligned} \qquad (1.16)$$

where L_{II} ($I = X, Y, Z$) is the Fresnel coefficient determined from:[87]

$$L_{XX}(\omega_i) = \frac{2n_1(\omega_i)\cos\gamma_i}{n_1(\omega_i)\cos\gamma_i + n_2(\omega_i)\cos\beta_i}$$

$$L_{YY}(\omega_i) = \frac{2n_1(\omega_i)\cos\beta_i}{n_1(\omega_i)\cos\beta_i + n_2(\omega_i)\cos\gamma_i}$$ (1.17)

$$L_{ZZ}(\omega_i) = \frac{2n_2(\omega_i)\cos\beta_i}{n_1(\omega_i)\cos\gamma_i + n_2(\omega_i)\cos\beta_i}\left(\frac{n_1(\omega_i)}{n'(\omega_i)}\right)^2$$

Once again the frequency dependent n_1, n_2 and n' are refractive indices of the light in medium 1, medium 2 and the interfacial layer, respectively; γ_i (i = SFG, visible, IR) is the refractive angle of the ith laser beam, which is derived from $n_1(\omega_i)\sin\beta_i = n_2(\omega_i)\sin\gamma_i$. As SHG is a special case of SFG in which the two incidence beams are identical, equation 1.16 and 1.17 are also qualified for SHG.

As illustrated by equation 1.16, the relative amplitude of the non-zero susceptibility tensor elements can be obtained by taking polarization-resolved SFG measurements. Consequently, orientation analysis can be done to extract information about the interfacial molecular orientation.[88-91] Details about relating the determined $\chi_{IJK}^{(2)}$ to the orientation of the corresponding vibrational mode will be discussed in chapter 5.

1.3.4 Broadband SFG

There are two types of SFG experimental set-ups with respect to the bandwidth of IR light in the frequency domain: scanning SFG and broadband SFG.

In scanning SFG, both visible light and IR light have narrow bandwidths (< 10 cm^{-1}) in the frequency domain. The frequency of visible light is fixed, and in order to collect an SFG spectrum over a wide range of wavenumbers, the frequency of IR light is scanned point by point.

In broadband SFG, the frequency-fixed visible light is also narrow in the frequency domain; however, the IR light has a much broader bandwidth (> 120 cm^{-1}). By changing the central frequency of the IR light, SFG spectra can be collected shot by shot. The IR power usually has a broad Gaussian shape in the frequency domain, which can be determined by using a spectrometer or measuring the SFG spectra from a gold surface, which exhibits strong non-resonant SFG. Consequently, power normalization is necessary after acquiring spectra. Nevertheless, compared with scanning SFG, it is faster to collect a spectrum using broadband SFG.[92]

For all the experiments present in this thesis, SFG spectra were acquired using broadband SFG, in which the IR pulse had a bandwidth of at least 120 cm^{-1}. Generally, most of experiments can be done using no more than three broadband IR pulses centered at different frequencies. Details about the experimental set-up are described in each chapter.

1.4 Applications of SHG and SFG

SHG and SFG are well-suited to study the properties of interfacial molecules at various interfaces. As previously mentioned, resonant SHG is usually used to probe the electronic transition, while SFG is used to probe the vibrational transition. In this section, the application of SHG and SFG in some specific research areas will be briefly discussed.

Firstly, as surface-specific techniques, SHG and SFG signals are very sensitive to the orientation change of interfacial molecules. By using polarization-resolved resonant SHG and vibrational SFG, information about absolute orientation of interfacial molecules can be extracted, which is important in the description of many chemical, physical and biological interfacial processes. Much work has been done in determining how to relate SHG and SFG measurements

to the orientation of specific molecules at various interfaces. Rowlen and co-worker published the full description of orientation analysis using polarized resonant SHG.[74] Wang and co-workers quantitatively described how to do spectral and orientational analysis using polarized vibrational SFG, and developed a set of polarization selection rules for assignment of SFG spectra.[68] Phase-sensitive SFG is a new development of SFG that provides information about the absolute direction of the molecule on interest.[93-94] Different from conventional SFG, in which $\left|\chi^{(2)}\right|^2$ is measured, the imaginary part of the second-order nonlinear susceptibility is directly probed in phase-sensitive SFG by the use of a reference (local) oscillator, and therefore the complexity of $\chi_R^{(2)}$ can be determined. The most famous application of phase-sensitive SFG was the study related to the interfacial structure of water.[95-96] The flip-flop of interfacial water molecules (i.e. a change in orientation by ~180 degrees) was observed upon a change in solution pH or by inverting the charge of chemical species present at the interface (for example positive or negative surfactants).

Secondly, resonant SHG and vibrational SFG can be used to probe the kinetics of interfacial processes.[71-72] As resonant SHG or SFG signal is related to the number density of interfacial molecules, interfacial processes such as adsorption/desorption can be followed in real-time by monitoring the change in the signal intensity. In experiments, the resonant SHG or SFG signal is often recorded as a function of time, in which kinetic information of the interfacial process such as reaction order can be extracted; the signal is also recorded versus a controllable variable in the system of interest, such as concentration, temperature and pressure, in which thermodynamic information such as binding affinity and adsorption energy can be extracted.[17] For example, by using resonant SHG, Geiger and co-workers quantified the binding energy of the toxic metal pollutant chromate and uranyl at different solid/water interfaces.[97-99] In recent studies, Yan and

co-workers successfully probed the secondary structure of a protein and its folding kinetics at interfaces by monitoring chiral SFG as a function of time.[51, 100]

Thirdly, vibrational SFG can be used to follow chemical reactions at interfaces. Taking advantage of the sensitivity of vibrational SFG in probing the presence of new chemical species, information about reaction intermediates and the reaction mechanism can be extracted. Much work has been done to follow chemical reactions at solid/gas and solid/liquid interfaces. For example, Somorjai and co-workers studied oxidation, hydrogenation and dehydrogenation reactions on metal surfaces under reaction conditions from ultra-high vacuum to high pressure using vibrational SFG;[101-103] they also studied the oxidation of CO on platinum surfaces in aqueous solution[104] and acetonitrile/water solutions.[105] In another example, Wieckowski, Dlott and co-workers studied ethanol oxidation at the aqueous/platinum interface.[106] With respect to biological systems of interest, Ye and co-workers followed the enzyme-catalyzed hydrolysis reaction of a planar supported lipid bilayer at the silica/buffer interface.[107]

Fourthly, for non-resonant SHG, the $\chi^{(3)}$ technique proposed by Eisenthal[50, 55-56] has been well developed to study the acid-base properties of solid/aqueous interfaces. With respect to the silica/aqueous interface, the silica surface is not neutral but charged at solution pH values greater than pH 3. The surface charge induces an interfacial potential, which also interacts with interfacial water and contributes to the non-resonant SHG signal through a $\chi^{(3)}$ term. Any change in the protonation state of surface silanols will change the surface charge density and the interfacial potential, changing the SHG signal accordingly. The $\chi^{(3)}$ technique has wide applications, especially in the study of the adsorption of metal cations onto silica surface,[108-112] and the study of specific ion effects on the acid-base properties of the silica surface.[113-115]

In recent years, the application of the nonlinear optical techniques SHG and SFG has spread into many different research areas. In material science, SFG has been used to study the surface molecular structures of polymer materials,[49, 57] while SH and SF scattering have been used to study the properties of particles and droplets.[116-117] In environmental science, SHG has been used to study the abrasion and dissolution of mineral oxides in aqueous solution,[118] and the adsorption of toxic metal pollutants on solid surfaces.[97-99] In chemical biology, SFG has been employed to study the properties of various components of biological systems including lipids, peptides and proteins.[51, 100, 119-123] SHG and SFG are also employed in microscopy applications, which effectively probe microscopic interfacial phenomena while avoiding interference signal from bulk phases.[124]

1.5 Thesis Organization

Taking the widely used planar silica and functionalized silica as substrates, this thesis focuses mainly on characterizing the structure and order of molecules at these solid surfaces, and investigating the thermodynamics and kinetics of processes at both solid/liquid and solid/air interfaces using the nonlinear optical techniques vibrational SFG and SHG.

Chapter 2 describes a study on the performance of silica supported organocatalysts using nonlinear optical techniques. Specifically, the binding of a model reactant 4-nitroacetophenone with amino and ureido organocatalytic monolayers on silica has been investigated at the acetonitrile/solid interface using a combination of SHG and vibrational SFG. By changing the ketone concentration in the bulk solvent, binding isotherms at each interface were determined from SHG measurements. Langmuir fitting of these isotherms yielded binding energies consistent with hydrogen bond formation. Surprisingly, the ketone had a lower binding affinity

for ureido monolayers compared with its binding behavior at amino-modified surfaces despite the fact that urea can form two hydrogen bonds with carbonyl groups. This lower binding affinity was attributed to the presence of a hydrogen bond network within the ureido monolayer that must be disrupted to facilitate ketone binding. Vibrational SFG measurements of the urea groups in the N-H stretching region revealed two new peaks upon introduction of the ketone that were attributed to the ketone-bound urea.

Chapter 3 describes a study of the reaction mechanism at interface using SFG. The Cu(I)-catalyzed 1,3-dipolar azide-alkyne cycloaddition (CuAAC) has arisen as one of the most useful chemical transformations for introducing complexity onto surfaces and materials owing to its functional group tolerance and high yield. In this chapter, the reaction of a benzyl azide monolayer at the silica/methanol interface was monitored in real-time using broadband SFG. A strong peak at 2096 cm^{-1} assigned to the azides was observed for the first time by SFG. Using a cyano-substituted alkyne, the decrease of the azide peak and the increase of the cyano peak (2234 cm^{-1}) were probed simultaneously. From the kinetic analysis, the reaction order with respect to copper was determined to be 2.1, suggesting that CuAAC on the surface follows a similar mechanism as in solution.

Chapter 4 describes monitoring the thermal dissociation of immobilized DNA duplexes using vibrational SFG. By employing the CuAAC reaction, a thymidine 15-mer (T_{15}) monolayer was immobilized on silica, which is the most common substrate for DNA chips and microarrays in biodiagnostics. To determine the overall order and thermal sensitivity of DNA, the interactions of the silica supported T_{15} strands with complementary A_{15} strands in solution were studied using SFG. The methyl groups on the T_{15} single strand were found to be considerably ordered at both the silica/buffer and silica/air interfaces, which was surprising as single stranded

polythymidine does not exhibit self-stacking. The most temperature-sensitive mode was also attributed to the methyl groups, which should experience significant reorientation upon duplex dissociation. Fitting revealed a melting temperature that is ~ 12 °C lower than the solution-phase melting temperature. This value of ~ 12 °C agrees exactly with previous work utilizing SHG to monitor the thermal dissociation of a DNA 15mer at the silica/buffer interface, indicating that immobilization on silica is quite destabilizing leading to a low dissociation temperature.

Chapter 5 describes our study of the interfacial structure of acetonitrile at the silica surface with and without water present and as a function of pH. SFG spectra of acetonitrile in the C-H stretch region were collected from the silica/aqueous interface at various acetonitrile concentrations. A strong peak attributed to the methyl symmetric stretch within the acetonitrile molecule was observed in both the ppp and ssp spectra. Unlike previous studies, in which a double-Lorentzian model was used to fit the peak, a single-Lorentzian model was found to best fit our data. Orientation analysis suggested that the net orientation of interfacial acetonitrile molecules did not change significantly as the acetonitrile concentration decreased. At certain acetonitrile/water composition, increasing solution pH from a neutral value to a strongly basic value effectively decreased the number density of interfacial acetonitrile molecules, which correlated strongly with an increase in the amount of ordered interfacial water.

Chapter 6 describes the conclusion of this thesis and future work for related projects.

Chapter 2

Ketone Binding at Amino and Ureido Monolayer/Solvent Interfaces Studied by Nonlinear Optical Techniques

Portions of this chapter are reproduced with permission

from the American Chemical Society (ACS)

2.1 Introduction

Green chemistry represents a synthetic paradigm that embodies the balance between beneficial properties and hazardous side effects by emphasizing the design of low-impact, environmentally benign synthetic strategies.[125] One strategy for making catalytic reactions green involves taking a well established soluble catalyst and immobilizing it onto a solid support; ideally, this immobilized catalyst is stable throughout the catalytic process, can be separated from the reaction products easily, and reused in subsequent reactions with minimal preparation. A great deal of work has been done towards making these reusable immobilized catalysts.[7, 126-127] However, tethering catalysts to solid support can have deleterious effect on catalyst performance, and the unpredictable variation in the performance of the catalysts upon immobilization, such as activity, enantioselectivity and recyclability, still remains a major drawback in the field.[128] If we can correlate the performance of immobilized catalyst systems with the molecular environment around the immobilized catalyst, we should be able to address some of these shortcomings and ultimately predict and control the behavior of such immobilized catalysts.

At the solid/solvent interface, immobilized molecules often have different properties compared with solution bulk molecules.[16] For example, homogeneous Ti-salen catalyst complexes that are immobilized via axial coordination with surface silanol sites exhibit lower activity and enantioselectivity than the same catalyst in solution.[129] One class of techniques that can be used to study these interfacial molecules is second-order nonlinear optical spectroscopy, including second harmonic generation (SHG) and sum frequency generation (SFG).[54] As surface-specific techniques, they are well suited to follow processes that proceed at a variety of interfaces.[48-53] SHG can be used to monitor the electronic signatures of the interface, while vibrational SFG can be used to probe the presence and changes of vibrational signatures at the

interface. Combining these two techniques, multiple features of an immobilized catalyst system, such as molecular orientation and binding affinity, can be monitored in the presence of reactant and solvent.

Compared with metal-based catalysts, organocatalysts have many advantages such as less sensitivity to moisture and oxygen, amenability to mild reaction conditions, low cost, and low toxicity.[130] The growing interest in "greening" catalytic reactions has led to great progress in organocatalysis,[131-134] and much work has been done towards immobilizing organocatalysts covalently onto a wide range of solid supports, such as polymers, magnetic nanoparticles and silica.[8-9, 135-136] Among them, silica supported bases and acids are two promising types of supported organocatalysts. For example, silica supported primary and secondary amines, as Lewis or Brønsted bases, usually perform well in catalyzing reactions related to carbanion generation, such as the aldol and Michael reactions.[9] Regarding Lewis acidic organocatalysts, urea and thiourea have been demonstrated to catalyze a multitude of reactions by activating the carbonyl electrophile through the formation of hydrogen bonds.[137-138] Like other Lewis acid catalysts, urea and thiourea have also been developed into immobilized catalysts,[139] especially in some cooperative catalysis systems.[140]

Here we explore the interaction between a ketone model reactant and two kinds of silica supported monolayer organocatalysts: basic amines and acidic urea groups by using a combination of SHG and SFG. In this work, 3-aminopropyltrimethoxysilane (APS) and 3-aminophenyltrimethoxysilane (APhS) were employed to make two types of amine monolayers on silica (Figure 2.1A). For the preparation of a Lewis acidic monolayer, 3-ureidopropyltrimethoxysilane (UDPS) was used to functionalize silica. After surface modification, the binding of model ketone 4-nitroacetophenone at these modified silica/solvent

interfaces was monitored by resonantly enhanced SHG (Figure 2.1B). Practically this involves using an incident beam to illuminate the interface and generate SH light at twice the frequency of the incident beam, which was then detected in a reflection geometry. The model ketone was found to bind to both the basic and acidic surfaces, but the binding was stronger for the amines. The low binding affinity of ketone for the Lewis acidic urea surface was attributed to the competition between ketone binding and hydrogen bond formation between neighboring urea molecules, which was supported by vibrational SFG measurements in N-H stretch region.
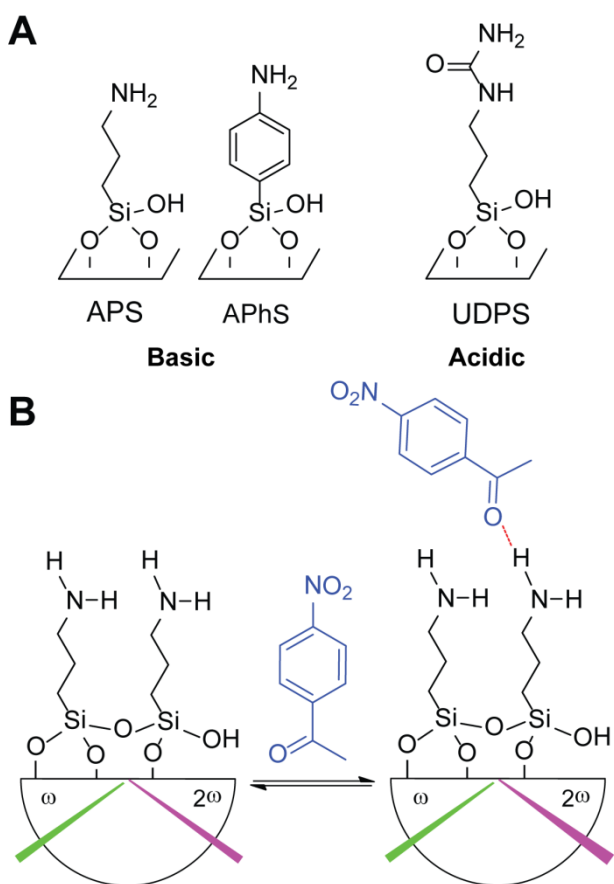
Figure 2.1 (A) The basic surfaces (APS-silica and APhS-silica) and acidic surface (UDPS-silica) under investigation. (B) The binding of model ketone 4-nitroacetophenone to the amino propyl (APS) modified silica/acetonitrile interface studied by SHG.

2.2 Experimental Section

2.2.1 Materials

All silanes were purchased from Aldrich while the remaining solvents and reagents were purchased from Aldrich, VWR, or Fisher and used without further purification. To 100 mL of toluene was added 100 μL of Millipore water, which was sonicated until it appeared clear (~30 minutes). The mixture was quickly separated into 20 mL aliquots that were capped in air-tight scintillation vials and used when needed. Silicon (100) wafers (prime grade, 0.5 mm thickness) were purchased from Fluoroware.

2.2.2 Self-Assembly of Monolayers

Monolayers were prepared on both silicon wafers containing a native oxide layer and silica hemispheres. Prior to silanization, substrates were cleaned with water and methanol, followed by drying in an oven for 10 min at 90 °C. The cleaned substrates were treated with fresh "piranha solution" (3:1 mixture of sulfuric acid and 30% hydrogen peroxide) for 1h. (*Caution: Piranha solution is a strong oxidizing agent and reacts explosively with organic compounds.*) They were then rinsed copiously with Millipore water, and methanol. Afterwards, the substrates were placed in an oven for 30 min at 90 °C, followed by cooling to room temperature and then plasma cleaning (plasma cleaner, PDC-32G, Harrick Plasma) in air for 2 min. The substrates were then immediately used in the silanization process.

Cleaned substrates were immersed in 3 mM APS, APhS or UDPS toluene solution (0.1 vol% water in dry toluene).[34, 141] The immersion time was 5 hours for APS and APhS, and 3 hours for UDPS. Then substrates were removed from the solution, rinsed rigorously with toluene, immersed in toluene for 30 min, sonicated for 5 min, and then rinsed with a 1:1 mixture of

toluene/methanol and methanol. Finally, the substrates were blown dry under nitrogen and used immediately in an experiment. For characterization, X-ray photoelectron spectroscopy (XPS) and atomic force microscope (AFM) measurements were performed on silicon wafers, while SHG and SFG studies were performed on silica hemispheres.

2.2.3 XPS Analysis
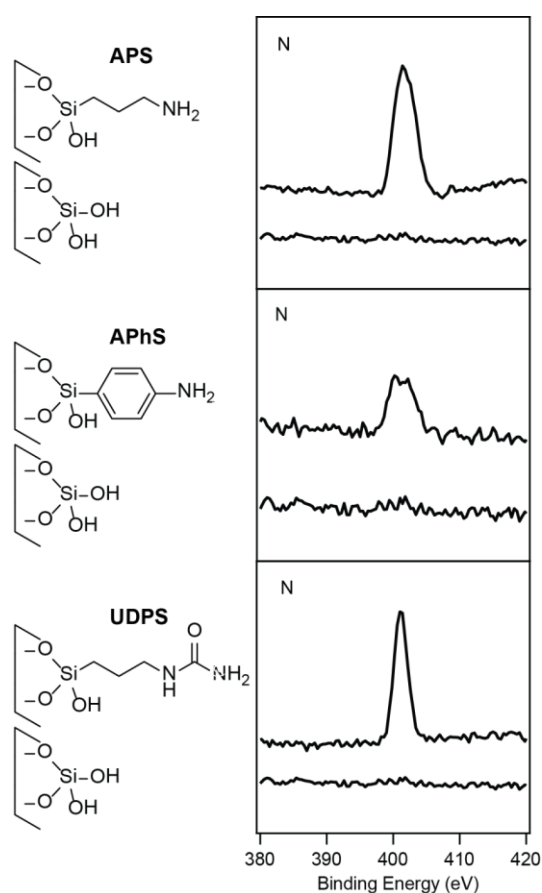
Figure 2.2 XPS analysis of the self-assembled monolayers formed on a silicon wafer.

XPS measurements were performed on samples prepared within 2 days using an AXIS ULTRA spectrometer (Kratos Analytical) with chamber pressure lower than 3×10^{-8} Pa. X-ray

was generated by a 210 W monochromatic Al K$_\alpha$ source (hν = 1486.7 eV). The incident angle was 35.3° from the plane of the sample surface and the photoelectron exit angle was 90°. XPS spectra were collected for binding energies from 1100 to 0 eV at a step of 0.4 eV. The analyzer pass energy was 160 eV.

XPS spectra are shown in Figure 2.2. After silanization, the presence of the APS, APhS and UDPS monolayers was confirmed by the N1s peak in the XPS wide scan spectrum compared with that of the bare wafer. The N1s peaks for all three surfaces appeared at around 401 eV in the spectrum.

2.2.4 AFM Analysis

AFM measurements were performed on freshly prepared samples using a MFP-3D AFM (Asylum). The AFM was operated in tapping mode with silicon cantilevers (Olympus, 300 kHz frequency).

AFM imagings are shown in Figure 2.3. The root-mean-square (RMS) roughness values for APS, APhS and UDPS modified silicon wafers were 0.31, 0.13, and 0.42 nm, respectively, indicating that monolayers were achieved.
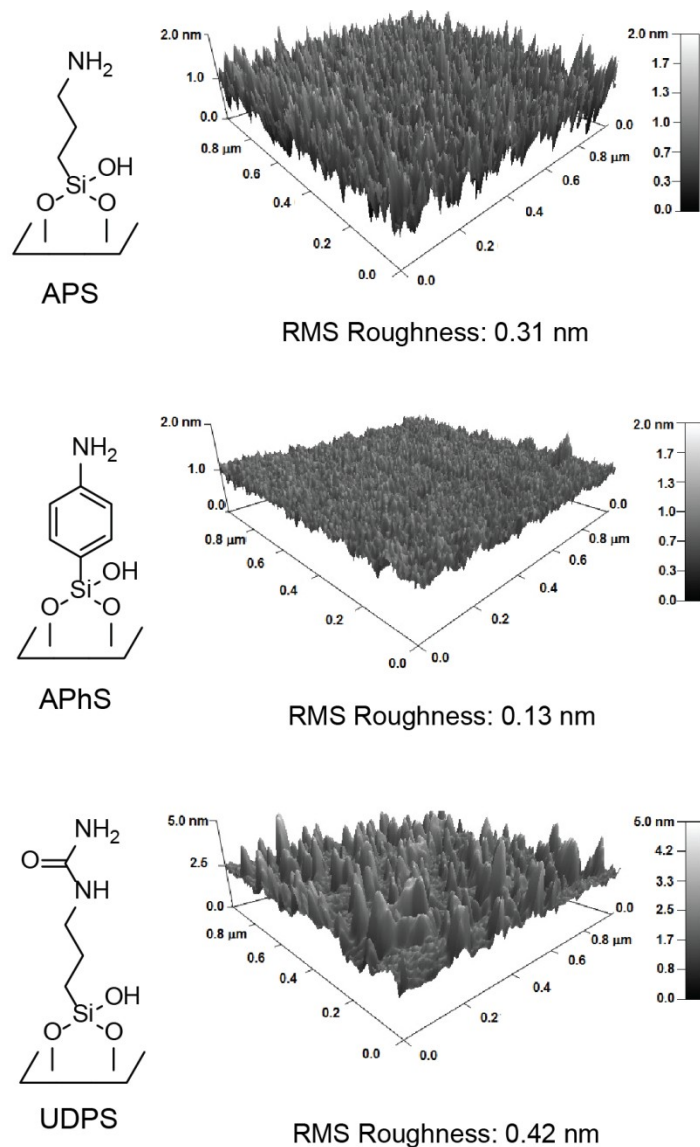
Figure 2.3 AFM analysis of the self-assembled monolayers formed on a silicon wafer.

2.2.5 Laser System and SHG Experimental Setup

The experimental setup for SHG measurements is shown in Figure 2.4. Our laser system consists of a Ti-sapphire oscillator (Spectra Physics, Maitai, 80 MHz), a Nd:YLF laser (Spectra Physics, Empower) and a regeneratively amplified laser (Spectra Physics, Spitfire Pro, 1kHz, 100 fs, 3.3 W). The Maitai and the Empower were used to seed and pump the Spitfire to generate an 800 nm beam. One-third of the Spitfire output (800 nm, 1.1 W) was used to pump an optical

parametric amplifier (Spectra Physics, OPA-800CF) to generate a tunable visible light in the wavelength range between 548 nm and 600 nm. The power of the visible beam was then decreased to ~0.3 μJ by a neutral-density filter (New Focus, cat. # 5215). After passing through a half-wave plate and a polarizer, the polarized visible beam was focused onto the modified-silica/acetonitrile interface at an angle of 62° from surface normal. The reflection beam from the interface was passed through a short pass filter (Thorlabs) and then directed into a monochromator (Optometrics Corporation, Mini-Chrom, MC1-02), which was tuned to the corresponding SH wavelength. SHG signal was detected by a photomultiplier tube (PMT, Hamamatsu Photonics), and the amplified electric response was counted with a gated photon counter (Stanford Research Systems). For orientation analysis, a polarizer was placed before the PMT to select the p-polarized or s-polarized SH response.

The modified silica hemisphere (ISP optics, 1 inch diameter, QU-HS-25, UV-grade SiO_2) was mounted on a custom-built Teflon cell. The flat side of the hemisphere was perpendicular to the laser table and in contact with the liquid phase in the sample cell. The top of the cell was exposed so solutions with different concentrations could be introduced. Prior to each experiment, the quadratic power dependence and appropriate bandwidth of the SHG were verified to ensure no sample damage was occurring at the interface. In the presence of monolayers or ketone at the acetonitrile/silica interface, we observed that prolonged measurement led to a significant increase in signal, which we attributed to damage of organic molecules at the interface. Thus we were careful to defocus our incident beam and measured SH for small time intervals (~50 seconds). These intervals were repeated every few minutes to ensure that the system had reached equilibrium.
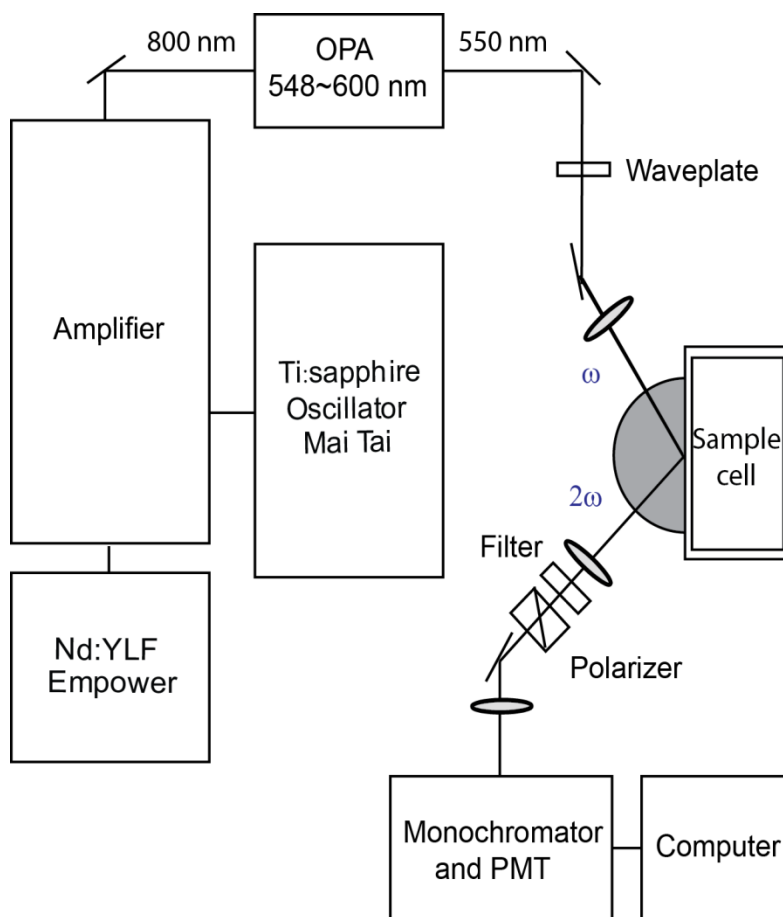
Figure 2.4 Schematic diagram of the experimental setup for SHG experiments.

2.2.6 Broadband SFG Experimental Setup

The experimental setup for SFG measurements is shown in Figure 2.5. Two-thirds of the Spitfire output (800 nm, 2.2 W) was used to pump a TOPAS-C/NDFG optical parametric amplifier (Light Conversion). The generated broadband infrared light (FWHM $\sim$ 120 cm^{-1}) was tunable between 3100 and 3600 cm^{-1}. The femtosecond visible light from the Spitfire (800 nm) was temporally broadened to picosecond (FWHM $\sim$10 cm^{-1}) using a Fabry-Perot etalon. The femtosecond IR beam ($\sim$10−12 μJ/pulse) and the picosecond visible beam ($\sim$10 μJ/pulse) were overlapped spatially and temporally onto the modified-silica/deuterated acetonitrile interface at angles of 66° and 64° from surface normal. The reflection beam was filtered with a bandpass

filter (Chroma, HQ 617/70 M) to remove residual visible light and then passed through a polarizer to select polarization. The polarized SF beam was focused onto a spectrograph (Acton SP-2556 imaging spectrograph, grating: 1800 grooves/mm with 500 nm blaze wavelength), which was connected to a camera (Acton PIXIS 100B CCD digital camera system, 1340×100 pixels, 20 μm $\times$ 20 μm pixel size, Princeton Instruments).
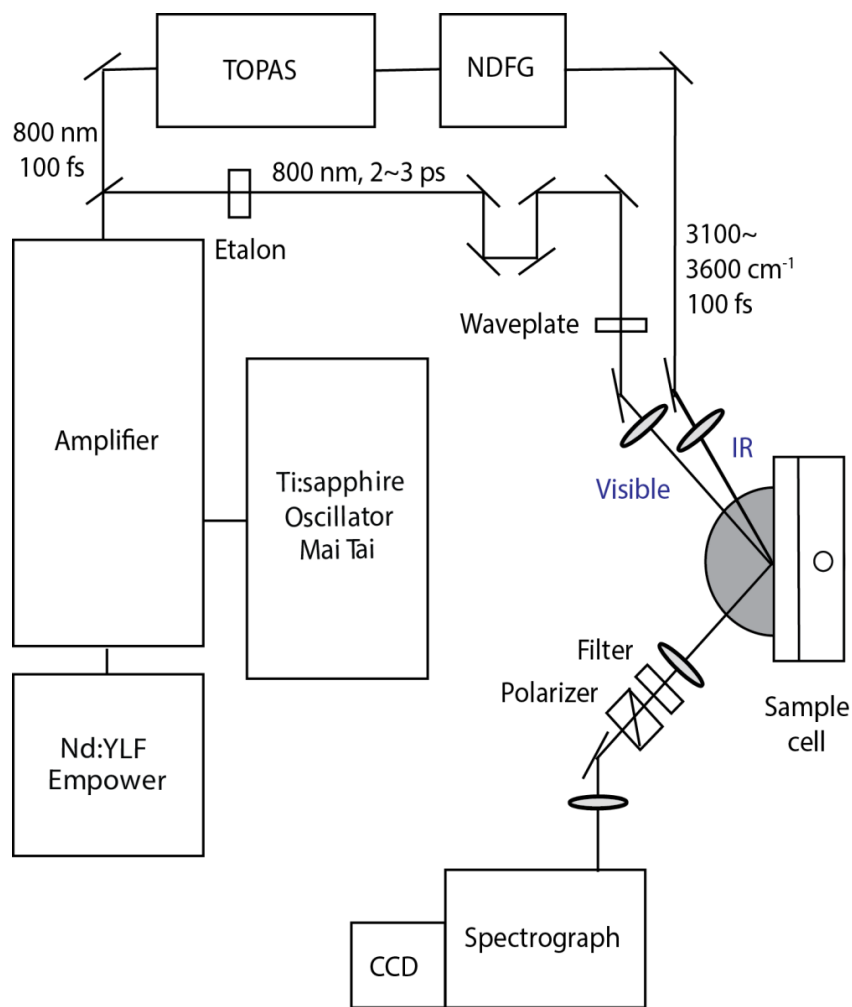
Figure 2.5 Schematic diagram of the experimental setup for broadband SFG experiments.

The SFG spectra were collected using the ssp polarization combination of input and output laser beams (s-polarized SFG output, s-polarized visible input, and p-polarized IR input). Four

IR beams centered at 3160, 3330, 3410 and 3520 cm^{-1} individually were employed to cover the N-H stretch region. Reference SFG spectra from a gold-coated silica hemisphere were collected both before and after each experiment. Spectra were then measured for the modified-silica/deuterated acetonitrile interface using the same configuration, and normalized by summing the spectra and dividing this summed spectrum by the sum of the gold spectra.[142]

2.2.7 Procedure of SFG Spectra Fitting

The fitting of SFG spectra was accomplished using Igor Pro software: based on the number of vibrational modes and the corresponding peaks expected in the spectrum, a fitting function with the desired number of resonant $\chi_R^{(2)}$ terms and a non-resonant term $\chi_{NR}^{(2)}$ was chosen. For each fit initial A_v, ω_v, Γ_v and $\chi_{NR}^{(2)}$ were estimated and then the software was allowed to optimize all of these fit parameters; the returned values from the previous run were used as initial values for a second run. The fitting stopped when the returned values were the same as the previous input values. The reported amplitudes ± the standard deviations were returned from the fit.

2.3 Results and Discussion

2.3.1 Monitoring Ketone Binding with SHG Spectroscopy

Under the electric-dipole approximation, SHG is forbidden in centrosymmetric bulk materials and consequently is sensitive to processes at the interface, where centrosymmetry is broken.[62] When the molecule adsorbed at the interface has an electronic transition that is in resonance with the incident frequency or SH frequency, the second harmonic response will be

significantly enhanced. Thus, we use resonantly enhanced SHG to monitor the binding of 4-nitroacetophenone at these modified silica/acetonitrile interfaces.

As shown in equation 2.1, the intensity of SHG at an interface, I_{SHG}, is related to the second order nonlinear susceptibility of the interface, $\chi^{(2)}$. When the incident light or SH is in resonance with a transition within an interfacial species, $\chi^{(2)}$ can be expressed as the sum of its nonresonant and resonant contributions, $\chi_{NR}^{(2)}$ and $\chi_{R}^{(2)}$.

$$I_{SHG} = \left|\chi^{(2)}\right|^2 = \left|\chi_{NR}^{(2)} + \chi_{R}^{(2)}e^{i\Delta\phi}\right|^2 \tag{2.1}$$

where $\Delta\phi$ is the phase difference between the nonresonant and resonant terms. For resonant SHG at the silica/solvent interface, this phase difference is assumed to be 90°, which allows the relative $\chi_{R}^{(2)}$ to be determined from the normalized signal intensity.[143] The resonant second-order susceptibility can be modeled as the product of the number density of the resonant surface species, N, and the orientationally averaged molecular hyperpolarizability, $\left\langle\beta^{(2)}\right\rangle$.

$$\chi_{R}^{(2)} = N\left\langle\beta^{(2)}\right\rangle \tag{2.2}$$

Assuming $\left\langle\beta^{(2)}\right\rangle$ remains constant during the adsorption process, then the resonant susceptibility $\chi_{R}^{(2)}$ is directly proportional to the number density of molecules absorbed at the interface. This linear relationship makes it very straightforward to relate the change in intensity with the change in surface coverage of adsorbing species.

As stated earlier, many reactions utilizing amine or urea organocatalysts involve carbonyl containing electrophiles like ketones and aldehydes. Therefore, we sought an SHG-active ketone that we could monitor using resonantly-enhanced second harmonic generation. 4-

Nitroacetophenone absorbs strongly at 264 nm in acetonitrile (Figure 2.6A), which is an ideal λ_{max} value for our SHG experiments based on our laser assembly.
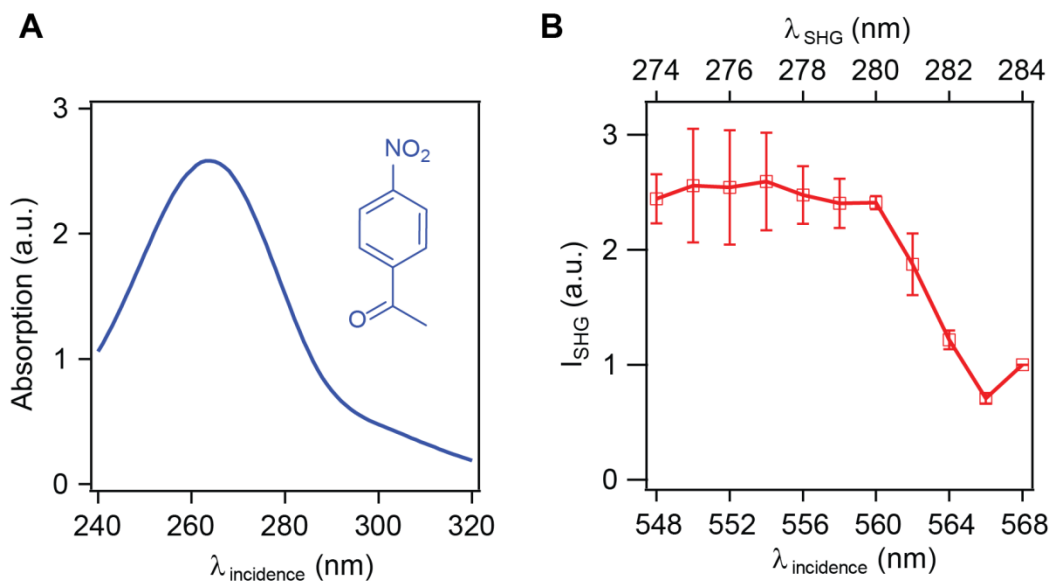
Figure 2.6 (A) The UV-vis absorption spectrum of 4-nitroacetophenone in acetonitrile. (B) The average SHG spectrum of 4-nitroacetophenone absorbed at the UDPS-silica/acetonitrile interface. The spectra were collected using a 15-mM ketone solution.

To verify that the ketone exhibited resonantly enhanced SHG upon binding to the surface, we measured the SHG from the UDPS(urea)-silica/acetonitrile interface in the presence of a 15 mM solution of 4-nitroacetophenone by monitoring the SHG intensity as a function of the incident wavelength. Figure 2.6B reveals that the SHG intensity displayed resonant enhancement when the incident beam had a wavelength between 548 nm and 560 nm, consistent with the UV-visible spectrum of 4-nitroacetophenone in acetonitrile. Based on the SHG spectrum, an incident beam of 550 ± 2 nm was chosen for our 4-nitroacetophenone adsorption studies, which corresponded to an SHG wavelength of 275 nm.

2.3.2 Ketone Adsorption/Desorption Traces
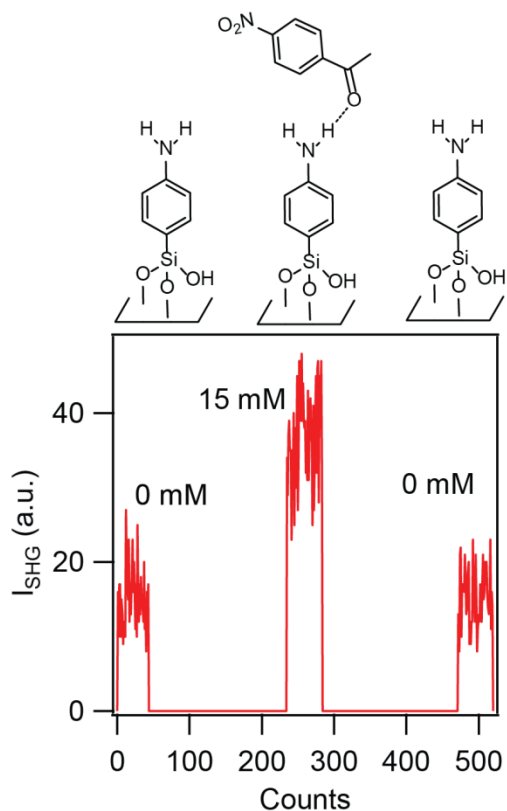
Figure 2.7 Adsorption/desorption trace for 4-nitroacetophenone absorbed at the APhS-silica/acetonitrile interface. One count corresponds to approximately one second.

To assess the reversibility of ketone binding to the basic and acidic surfaces of interest, adsorption/desorption studies were performed. First, the background signal was collected from the functionalized silica/acetonitrile interface; then the acetonitrile in the sample cell was replaced by a 15-mM ketone solution. As expected, the SHG signal increased substantially upon introducing the 4-nitroacetophenone due to resonant enhancement. Next the ketone solution was removed and the sample surface was washed repeatedly with solvent, at which point the SHG intensity went back to the original level. This indicated that the interaction was fully reversible. Figure 2.7 illustrates the adsorption/desorption trace for 4-nitroacetophenone absorbed at the

47

APhS-silica/acetonitrile interface. The same method was used to assess the reversibility of ketone binding to APS-silica/acetonitrile and UDPS-silica/acetonitrile interfaces, and similar reversible interactions were observed.

2.3.3 Ketone Adsorption Isotherms

Owing to the reversibility of ketone binding with the interface, the Langmuir model of surface adsorption can be used to describe the dependence of SHG signal on the bulk ketone concentration. In the Langmuir model, the surface can be treated as a series of non-interacting empty sites, and the adsorption process can be described as the binding of a ketone molecule (M) with an empty surface site (ES) to form a filled site (FS).[144]

$$M + ES \underset{k_{-1}}{\overset{k_1}{\rightleftharpoons}} FS \tag{2.3}$$

The kinetic form of this equilibrium is:

$$\frac{dN}{dt} = k_1 \frac{C(N_{max} - N)}{19.15} - k_{-1} N \tag{2.4}$$

where N is the number of absorbed ketones, N_{max} is the maximum number of accessible surface sites, C is the bulk concentration of ketone, 19.15 is the molarity of the solvent acetonitrile, and k_1 and k_{-1} are the rate constants for adsorption and desorption, respectively.[144]

When the system reaches equilibrium, the rate of adsorption equals the rate of desorption, and $\frac{dN}{dt} = 0$. If we define the equilibrium constant K as the ratio of the rate constants (k_1/k_{-1}), then the relative surface coverage $\frac{N}{N_{max}}$ can be expressed as a function of bulk ketone concentration C with equilibrium constant K.[144]

$$\frac{N}{N_{max}} = \frac{1}{1 + \dfrac{19.15}{KC}} \tag{2.5}$$

If we assume that the net orientation of the ketone does not change as a function of surface coverage, then from equation 2.1, 2.2 and 2.5, the relationship between resonant SHG intensity and the ketone concentration can be obtained:

$$I_{SHG} - I_0 \propto \left|\chi_R^{(2)}\right|^2 = \left|\frac{N_{max}\left\langle\beta^{(2)}\right\rangle}{1 + \dfrac{19.15}{KC}}\right|^2 = \frac{A}{\left(1 + \dfrac{19.15}{KC}\right)^2} \tag{2.6}$$

where I_0 is the nonresonant SHG intensity collected when there is no ketone present in the solution, and A is a constant that depends on the absolute number density and intrinsic activity of the ketone as well as the incident electric field. The adsorption isotherms of 4-nitroacetophenone at the APS-silica, APhS-silica and UDPS-silica/acetonitrile interfaces are shown in figure 2.8.
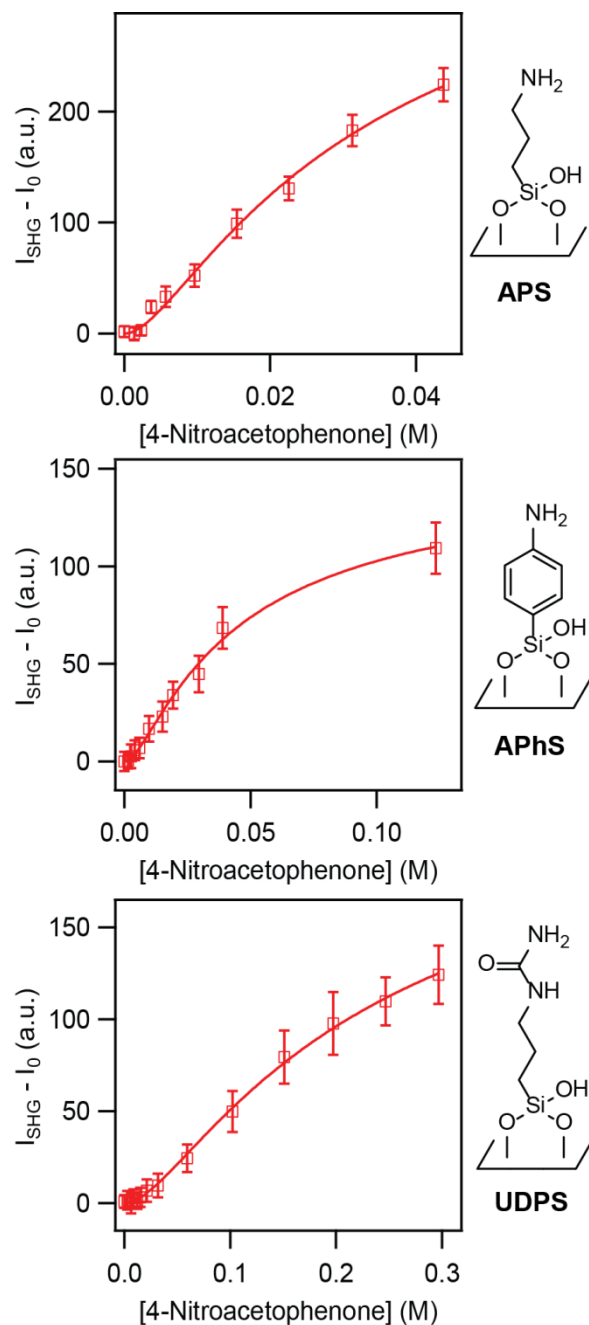
Figure 2.8 Adsorption isotherms of 4-nitroacetophenone at the APS-silica, APhS-silica and UDPS-silica/acetonitrile interfaces. Solid lines are fits with the Langmuir model (equation 2.6).

To determine the equilibrium constant, the isotherm data were fit with equation 2.6. From these values the adsorption free energy ΔG_{ads} was also easily obtained from:

$$\Delta G_{ads} = -RT \ln K \qquad\qquad (2.7)$$

The equilibrium constants K and adsorption free energies ΔG_{ads} for 4-nitroacetophenone adsorption at the APS-silica, APhS-silica and UDPS-silica/acetonitrile interfaces are summarized in table 2.1. The equilibrium constants for the basic APS-silica and APhS-silica/acetonitrile interfaces were $8(4) \times 10^2$ and $7(2) \times 10^2$, respectively; the adsorption free energies were also quite similar ($\sim$ -24 kJ/mol) at 298 K.

Table 2.1 Equilibrium Constants K and Adsorption Free Energies ΔG_{ads} for 4-Nitroacetophenone Absorbed at Functionalized-Silica/Acetonitrile Interfaces.

Interface	K	ΔG_{ads} / kJ·mol^{-1}
APS-silica/ACN	$8(4) \times 10^2$	-24(1)
APhS-silica/ACN	$7(2) \times 10^2$	-23.7(7)
UDPS-silica/ACN	$1.6(5) \times 10^2$	-19.8(8)

The interaction of the amines with the electrophilic carbon atoms of ketone could result in the condensation of the two, resulting in imine formation.[145] However, the rapid increase in SHG signal upon adding the ketone and the reversibility of this complex indicated that imine formation was unlikely. Instead, the calculated adsorption free energies were consistent with hydrogen-bond formation between the amino monolayers and the ketone. This lack of condensation is not surprising as the condensation is often promoted with the use of a small amount of catalytic acid, which is absent in our system.[146] Additionally, amines are often employed to activate the nucleophile rather than the electrophilic carbonyl in reactions using

amino monolayers and have been found to not undergo condensation in the absence of acid.[147-148] Yet, as both the amine and carbonyl compound are present in the reaction mixture it is still important to identify any interactions of the ketone with these monolayers for a complete understanding of these systems.

Regarding the specificity of the hydrogen bonding interaction with the 4-nitrophenyl substituted ketone and the amino monolayers, previous studies indicated that the oxygen atoms in aromatic nitro groups, which are very weakly basic, are not good hydrogen bond acceptors.[149-151] Rather the oxygen atoms on the carbonyl are far better hydrogen bond acceptors[150] and therefore are expected to accept the amino hydrogen (N-H) from APS and APhS to form a hydrogen bond. The determined adsorption free energies of the ketone absorbed at APS-silica and APhS-silica/acetonitrile are on the order of one or two such bonds as a single hydrogen bond formed by an amine donor and a carbonyl acceptor has a binding energy in the range of 11 to 17 kJ/mol.[150] Although the amino groups in APS and APhS have different substituents that result in different Brønsted acidities (for alkyl amines, pK_a = 38~40; for phenyl amines, pK_a = 25~31),[150] the formed hydrogen bonds have similar bond energies.

Compared with the APS and APhS modified silica surfaces, 4-nitroacetophenone adsorption at the Lewis acidic UDPS-silica/acetonitrile interface had a lower binding constant ($1.6(5) \times 10^2$) and adsorption free energy magnitude (~-20 kJ/mol). This lower affinity for the urea, which is known to form two hydrogen bonds with carbonyl groups,[137-138, 140] was surprising. To understand the lower affinity of the ketone for the ureido surface, we consider the hydrogen bonded environment of the monolayer. Specifically, the ureido groups possess both C=O and N-H moieties, which are good hydrogen bond donor and acceptor components. Therefore we propose that the UDPS monolayer on silica formed a network through hydrogen bonding of

neighboring molecules, which is consistent with observations of urea derivatives in crystals[152-153] and in organic solvents.[154] Upon introducing the ketone to the UDPS monolayer, the ketone had to break this hydrogen bond network to form new hydrogen bonds with the ureido groups, hence lowering the magnitude of the resulting adsorption free energy.

2.3.4 Polarization Dependence of SHG Response and Average Molecular Orientation

Resonant enhanced SHG can also be used to probe the ketone orientation at these different interfaces. For a rotationally isotropic surface, there are only three independent nonzero surface second-order susceptibility tensor elements, $\chi_{ZZZ}^{(2)}$, $\chi_{XXZ}^{(2)}$ and $\chi_{ZXX}^{(2)}$.[64, 69, 73] For SHG fields polarized parallel to the plane of incidence ($I_p^{2\omega}$) and perpendicular to the incidence plane ($I_s^{2\omega}$), the SHG signal can be expressed as follows:[69, 71, 73-74]

$$I_s^{2\omega}(\gamma) = C \left| s_1 \sin(2\gamma) \chi_{XXZ}^{(2)} \right|^2 \left(I^\omega \right)^2 \tag{2.8}$$

$$I_p^{2\omega}(\gamma) = C \left| s_5 \chi_{ZXX}^{(2)} + \cos^2 \gamma \left(s_2 \chi_{XXZ}^{(2)} + s_3 \chi_{ZXX}^{(2)} + s_4 \chi_{ZZZ}^{(2)} - s_5 \chi_{ZXX}^{(2)} \right) \right|^2 \left(I^\omega \right)^2 \tag{2.9}$$

where $I^{2\omega}$ is the SHG intensity, I^ω is the incident beam intensity, γ is the polarization rotation angle of the incident beam ($\gamma = 0°$ corresponds to p-polarization and $\gamma = 90°$ corresponds to s-polarization). The s_i terms are constants that depend on the experimental geometry. The axis labels X, Y and Z are of the interface coordinate system in the laboratory frame, and Z is the surface normal. The relative amplitudes of the three nonzero tensor elements can be determined by fitting the SHG data collected at two different polarizations as a function of incident polarization using equation 2.8 and 2.9.
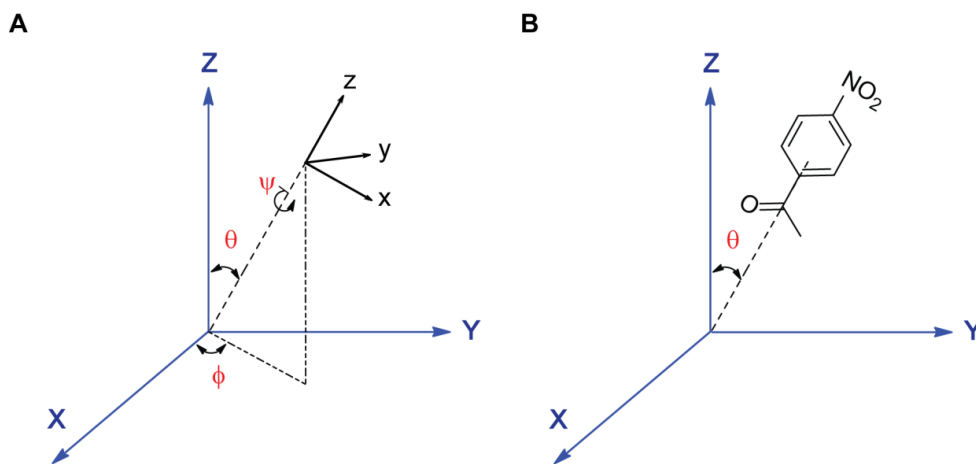
Figure 2.9 (A) Three Euler angles (azimuthal angle ϕ, tilt angle Θ and twist angle ψ) correlating molecular coordinate system (xyz) and laboratory coordinate system (XYZ). (B) Only tilt angle Θ is left to be determined under the assumption that a single molecular hyperpolarizability element $\beta_{zzz}^{(2)}$ dominates the second harmonic signal and the molecule exhibits uniform random distribution in ϕ and ψ.

The surface second order susceptibility tensor elements $\chi^{(2)}$ can be related to the molecular second order susceptibility tensor elements $\beta^{(2)}$ through Euler transformation. Three Euler angles, in-plane rotation angle ϕ, tilt angle Θ and twist angle ψ as shown in Figure 2.9A, are needed to correlate molecular coordinate system (xyz) and laboratory coordinate system (XYZ). For a rod-like molecule, it is common to assume that a single molecular hyperpolarizability element $\beta_{zzz}^{(2)}$ dominates the second harmonic signal, where z is the molecular axis, and assume that the molecule exhibits uniform random distribution in ϕ and ψ, so only one orientation parameter Θ is left to be determined. (Figure 2.9B) In this case, the nonzero surface second order susceptibility tensor elements have the following representations:[71, 74-75]

$$\chi_{ZZZ}^{(2)} = N\langle\cos^3\theta\rangle\beta_{zzz}^{(2)} \tag{2.10}$$

$$\chi_{XXZ}^{(2)} = \chi_{ZXX}^{(2)} = \frac{1}{2}N\langle\cos\theta\sin^2\theta\rangle\beta_{zzz}^{(2)} \tag{2.11}$$

where N is the surface number density of the absorbed molecule, θ is the angle between the molecular axis z and the interface normal axis Z, and the brackets denote the orientational average.

Figure 2.10 shows the polarization dependence of the SH response from 4-nitroacetophenone absorbed at the APS, APhS and UDPS-silica/acetonitrile interface. The experiments were done using a 15-mM ketone solution. By fitting the SHG data collected at different polarizations (p-polarized and s-polarized) as a function of incident polarization using equation 2.8 and 2.9, the relative amplitudes of the three nonzero tensor elements, $\chi_{ZZZ}^{(2)}$, $\chi_{XXZ}^{(2)}$ and $\chi_{ZXX}^{(2)}$, can be determined. In the analysis process, the amplitude of $\chi_{XXZ}^{(2)}$ was assumed to be 1, and the results are shown in table 2.2. There are two different sets of nonzero tensor elements, and they differ in the sign of $\chi_{ZXX}^{(2)}$ relative to the sign of $\chi_{XXZ}^{(2)}$. From the fits, the ratio of $\chi_{ZXX}^{(2)}$ to $\chi_{XXZ}^{(2)}$ is close to 1, suggesting the assumption that element $\beta_{zzz}^{(2)}$ dominates the second harmonic signal is reasonable.[72] For each interface, the orientation analysis experiment was done twice. Two tilt angles were determined for each run due to the sign difference between $\chi_{ZXX}^{(2)}$ and $\chi_{XXZ}^{(2)}$. The reported tilt angle in table 2.2 was the average of the two values determined from fitting the polarization-dependent data.
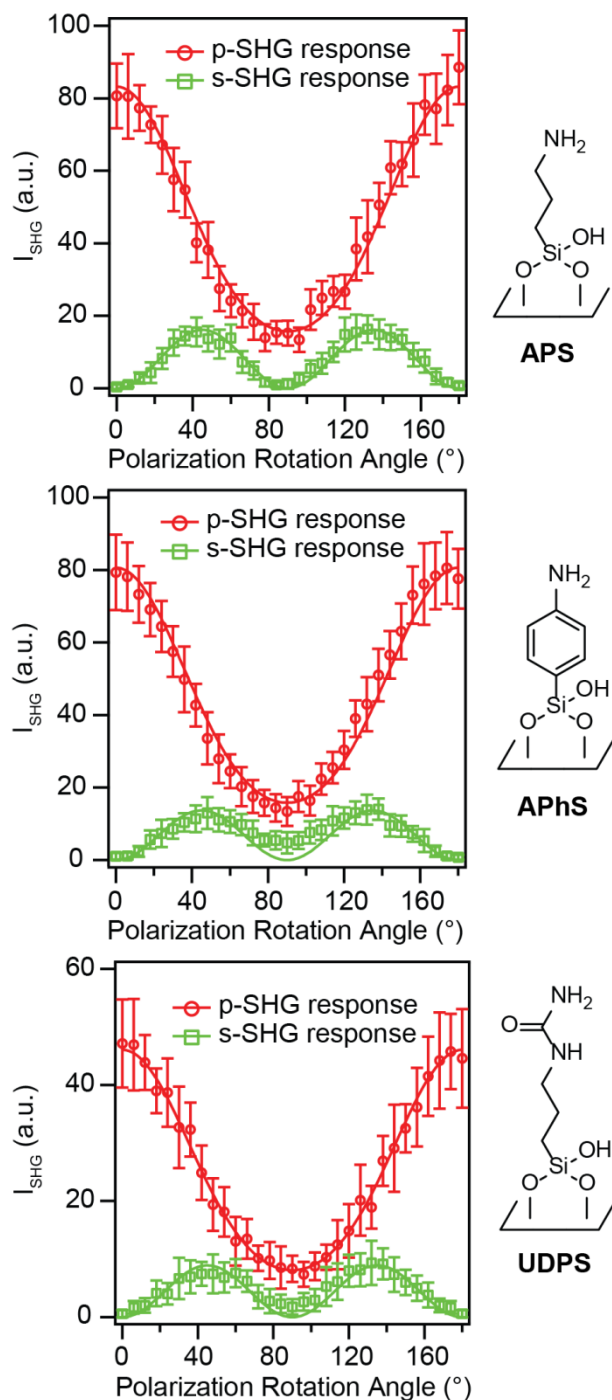
Figure 2.10 The polarization dependence of the p-polarized SHG (red) and s-polarized SHG (green) from 4-nitroacetophenone absorbed at the UDPS-silica/acetonitrile interface. The orientation analysis was done using a 15-mM ketone solution. The solid lines are fits with equation 2.8 and 2.9.

The mean tilt angle of 4-nitroacetophenone absorbed at APS-silica/acetonitrile, APhS-silica/acetonitrile and UDPS-silica/acetonitrile interfaces are determined to be $41 \pm 2°$, $40 \pm 2°$ and $39 \pm 2°$, respectively. These angles are close to the magic angle of 39°, which is the measured value that all molecules converge to as the distribution of orientations becomes more and more broad.[155] This indicates there are two possibilities for the orientation of the absorbed ketone molecule: one possibility is the ketones absorbed at all three interfaces are highly orientated with a similar tilt angle of ~39°. The more likely possibility, however, is the ketone orients randomly at these interfaces, resulting in a broad distribution of θ. The lack of unique binding orientation is not completely surprising given the ability of the ketone to form one or two hydrogen bonds with the interface.

Table 2.2 Nonzero $\chi^{(2)}$ Elements and Tilt Angles θ of 4-Nitroacetophenone Adsorbed at the Modified Silica/Acetonitrile Interfaces.

	APS (15 mM)		APhS (15 mM)		UDPS (15 mM)		UDPS (700 mM)	
χ_{xxz}	1	-1	1	-1	1	-1	1	-1
χ_{zxx}	0.98±0.01	0.98±0.01	0.96±0.15	0.96±0.15	0.88±0.11	0.88±0.11	0.88	0.88
χ_{zzz}	2.42±0.08	2.82±0.08	2.44±0.31	2.85±0.31	2.50±0.03	2.91±0.03	1.86	2.27
θ	42.0±0.4	39.8±0.3	41.6±0.4	39.4±0.6	40±2	38±2	44	41

The orientation analysis in Figure 2.10 was done using a 15-mM ketone solution, for UDPS-silica/acetonitrile interface, which corresponds to ~11% coverage for the UDPS monolayer. Another orientation analysis was done using a 700-mM ketone solution at the UDPS-silica/acetonitrile interface, which corresponds to 85% monolayer coverage. The mean tilt angle

was determined to be 44° or 41°, which is within error for the angle determined using the 15 mM solution (40° or 38°). This value is still very close to the magic angle of 39°, which indicates that there is likely a broad distribution of the ketone also at high interface coverage. The agreement between these two measurements indicates that changes in the ketone coverage rather than changes in orientation contribute mostly to the signal change.

2.3.5 SFG Spectra in N-H Stretch Region

As previously mentioned, utilizing urea and thiourea functional groups to activate carbonyl electrophiles is the basis of many organocatalytic systems,[137-138, 140] which made the low affinity of the ketone with the urea monolayer surprising. We attributed the relatively weak interactions with our SHG-active ketone and the urea-modified monolayer (UDPS) to the presence of a hydrogen-bonded network of the neighboring urea groups, which must break to accommodate ketone binding. To determine whether evidence of this network could be observed experimentally, a related vibrational nonlinear optical method, broadband SFG, was employed to study the N-H. (Figure 2.11A) Similar to resonantly enhanced SHG, when the IR frequency is in resonance with the N-H stretch modes at the interface, the second-order susceptibility $\chi^{(2)}$ becomes large, leading to an enhancement in the SFG electric field.

As this is also a second-order process, the intensity of SFG is related to the surface second order susceptibility $\chi^{(2)}$, and the electric fields of the IR and visible beams. This $\chi^{(2)}$ is further broken down into a non-resonant term $\chi_{NR}^{(2)}$, and vibrational resonant term $\chi_R^{(2)}$ summed over all possible frequencies, which is considered to possess a Lorentzian lineshape as shown below:[81-82, 84]

$$I_{SFG} \propto \left| \chi^{(2)} \right|^2 = \left| \chi_{NR}^{(2)} + \sum_v \chi_R^{(2)} \right|^2 = \left| \chi_{NR}^{(2)} + \sum_v \frac{A_v}{\omega_{IR} - \omega_v + i\Gamma_v} \right|^2 \qquad (2.12)$$

Here ω_{IR} is the frequency of the incident IR field, and A_v, ω_v and Γ_v are the amplitude, frequency, and damping coefficient of the vth surface vibrational mode, respectively. The value of A_v may carry either a positive or a negative sign, indicating the direction of the transition dipole moment of the corresponding mode.[85]

The acquisition of SFG spectra in the N-H stretch region is usually not easy because of the disturbance of water, whose SFG spectra has two broad peaks at around 3200 cm^{-1} and 3450 cm^{-1}.[156-157] Consequently, in these experiments freshly opened deuterated acetonitrile (d$_3$-ACN) was used to avoid the disturbance of water.
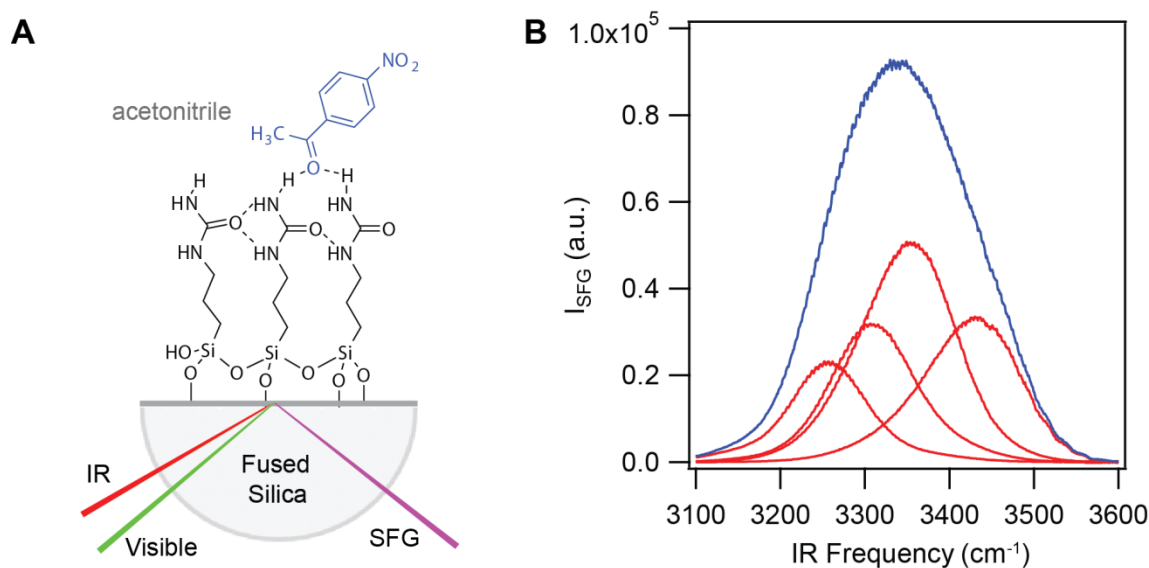
Figure 2.11 (A) The binding of model ketone 4-nitroacetophenone to the ureido propyl (UDPS) modified silica/acetonitrile interface studied by SFG. (B) Gold reference spectra for the SFG analysis. The red traces are the spectra collected at four different IR central wavenumbers and the blue trace is the sum of these red traces.

At the beginning of each experiment, reference SFG spectra were first collected using the same configuration from the gold/air interface using the same type of silica hemisphere coated with 200 nm of gold placed in the sample cell without using any solvent. As shown in Figure 2.11B, in order to study the N-H stretch in the urea group, four IR pulses were used to cover the region from 3200 cm^{-1} to 3500 cm^{-1}, then these spectrum were summed up to achieve a reference spectra. The spectra at the same IR central wavelengths were measured for the modified silica/d$_3$-ACN interfaces. After subtracting the background, these intensity spectra were summed up and divided by the gold reference spectra and then fit with equation 2.12.

Table 2.3 SFG Spectra Fitting Parameters in the N-H Stretch Region at the UDPS-silica/d$_3$-ACN Interface.

ω_v / cm^{-1}	0 mM [a]		40 mM [c]		200 mM [b]	
	A_v	Γ_v	A_v	Γ_v	A_v	Γ_v
3282	4(2)	67(15)	2.16(9)	67	0.60(9)	67
3344	3.8(3)	39(1)	2.78(3)	39	-	-
3373	-	-	-1.12(3)	33	-2.25(8)	33(1)
3429	-2.7(2)	43(2)	-2.26(4)	43	-	-
3471	-	-	1.36(6)	47	3.0(3)	47(3)
$\chi_{NR}^{(2)}$	0.148(7)		0.1455(6)		0.137(1)	

[a]The 0 mM spectrum was fit with three Lorentzian peaks allowing all ω_v, A_v, Γ_v and $\chi_{NR}^{(2)}$ values to vary. [b]The 200 mM spectrum was fit with three Lorentzian peaks with the ω_v and Γ_v values for the 3282 cm^{-1} peak held based on those found for the 0 mM spectrum. [c]The 40 mM spectrum was fit with five Lorentzian peaks with all ω_v and Γ_v values held based on those found for the 0 mM spectrum and the 200 mM spectrum. The notation 3.8(3) refers to 3.8 plus/minus 0.3, which is the average value plus/minus the standard deviation.

Normalized SFG spectra in the N-H stretching region at the UDPS-silica/d$_3$-ACN interface in the presence of different concentrations of ketone (0 mM, 40 mM and 200 mM) were shown in Figure 2.12B. The spectra were fitted with equation 2.12 and the fitting parameters are shown in table 2.3.
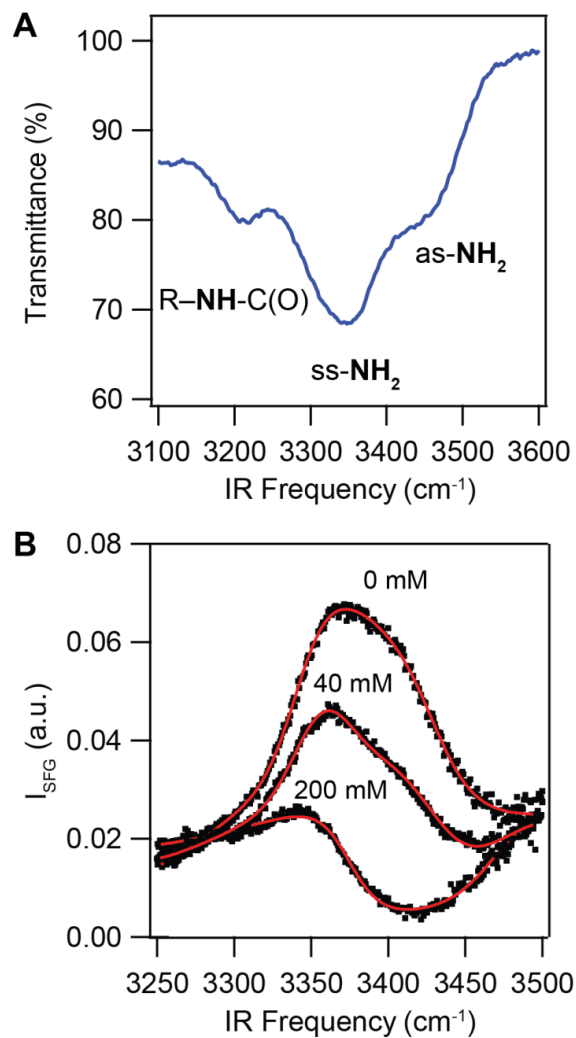
Figure 2.12 (A) IR spectra of UDPS in acetonitrile. (B) SFG spectra in the N-H stretching region at the UDPS-silica/d$_3$-ACN interface in the presence of 0 mM, 40 mM and 200 mM 4-nitroacetophenone. The solid lines are fits with equation 2.12. All SFG spectra were collected with the ssp polarization combination.

Figure 2.12A illustrates the IR absorbance spectrum of 3-ureidopropyltrimethoxysilane in acetonitrile; there are three N-H stretch modes present. The peaks at ~3350 cm^{-1} and ~3450 cm^{-1} have been assigned to the symmetric stretch mode (ss-NH$_2$) and the asymmetric stretch mode (as-NH$_2$) of the –NH$_2$ group on the urea based on IR assignments in the literature for unsubstituted urea.[158] We tentatively assign the third peak at ~3220 cm^{-1} to the N-H stretch of the R–NH-C(O) portion of urea bound directly to the surface. Figure 2.12B illustrates the SFG spectra at the UDPS-silica/d$_3$-ACN interface in the presence of different concentrations of ketone. When there was no ketone in the solution (0 mM), the spectral fit identified three peaks with frequencies of 3282, 3344, and 3429 cm^{-1}, consistent with the IR spectrum, which were consequently assigned to the N-H stretch for the disubstituted nitrogen in the urea and the symmetric (ss-NH$_2$) and asymmetric (as-NH$_2$) stretch of the terminal NH$_2$ group, respectively. The peak amplitudes for the symmetric and asymmetric stretch of the terminal NH$_2$ groups have opposite sign, indicating these two modes are out of phase.[159]

Upon adding ketone, however, the amplitudes of the peaks and the overall shape of the spectrum changed significantly. From the fit, two new peaks became apparent: one at 3373 cm^{-1}, the other at 3472 cm^{-1}, which were assigned to the symmetric and the asymmetric stretch of the NH$_2$ bound to the ketone, respectively. The presence of new peaks attributed to the ketone-bound urea supports that binding significantly changed the local environment of the urea. Moreover, the shift to higher wavenumbers indicated that weaker hydrogen bonds formed with the ketone than with neighboring urea sites, as increased hydrogen-bonding corresponds to lower vibrational wavenumbers.[157] This shift supports our hypothesis that the urea groups form a stable hydrogen-bonded network that the ketone disrupts upon binding (Figure 2.13). We also observed that the peak amplitude changed sign for the bound versus unbound NH$_2$ groups, resulting in

deconstructive interference in the spectra, which supports that binding to the ketone led to significant reorientation of the urea's terminal NH_2 group. Finally, we note that our assignment of symmetric and antisymmetric modes for the hydrogen-bonded urea presupposes that the hydrogen-bonding preserves C_{2v} symmetry. In contrast, a previous SFG investigation of urea at the air/water interface observed only one mode rather than the two observed in the IR spectrum,[85] which may stem from the different orientation or hydrogen-bonding environment of the molecule at this interface.
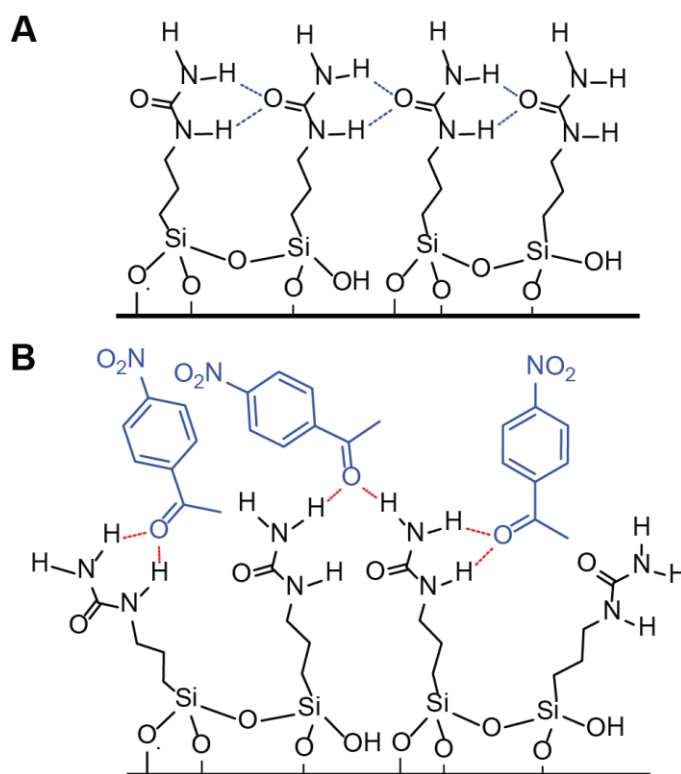
Figure 2.13 Schematic representation of surface urea orientation before (A) and after (B) ketone binding.

2.4 Conclusion

In this project, we investigated the binding behavior of a model ketone at silica supported basic and Lewis acidic monolayer surfaces using SHG and SFG. The binding at both types of monolayers was consistent with hydrogen bond formation between the donor group on the monolayer surface and the acceptor ketone molecule. Compared with its behavior on silica supported amino monolayers, the model ketone has a lower binding affinity at the silica supported urea monolayer despite the widespread use of urea organocatalysis in catalytic activation of carbonyl compounds. The lower binding affinity was attributed to the formation of a hydrogen bond network within the urea monolayer that must be disrupted to facilitate ketone binding. SFG data in the N-H stretch region indicated that ketone binding led to weaker hydrogen-bonds than those formed in the network and that binding led to an orientation change of the urea molecules. Overall, the SFG results shed light on the lower binding affinity observed by SHG. Finally, this investigation highlights how the combination of SFG and SHG is useful for studying the interactions of well-defined immobilized catalysts to better understand how the intrinsic affinity of the immobilized catalysts for the reactants influences the overall activity.

Chapter 3

Following the Azide-Alkyne Cycloaddition at the

Silica/Solvent Interface with Sum Frequency Generation

Portions of this chapter are reproduced with permission

from Wiley-VCH

3.1 Introduction

Silica is one of the most commonly used substrates for materials applications owing to its transparency to visible light, cost effectiveness, and stability to water and organic solvents. The surface modification of silica is also straightforward resulting in covalently attached molecules with a variety of functions stemming from immobilized homogeneous catalysts[7, 21, 128] to capture biomolecules.[160-161] Consequently much work has been focused on making diagnostic devices and catalytic materials on silica using glass slides or silica particles or gels. One challenge in optimizing these materials, however, is the difficulty in monitoring the functionalization process using real-time methods. As silica is an insulator, it is not amenable to the most common real-time methods like electrochemistry and surface plasmon resonance.[162] As a result, little is known about the dynamics of covalent reactions at the silica/liquid interface despite their significance.

One class of techniques that is uniquely well suited to monitor processes at such buried interfaces is second-order nonlinear optical spectroscopy,[48, 50, 54, 163] because of its intrinsic surface selectivity and accessibility to a variety of different solids, from polymers[49] and metals[101] to silica and other mineral oxides.[157] Vibrational sum frequency generation (SFG) is one such second-order process that has been widely utilized to follow covalent reactions at the silica/gas interface[164] and at catalytic metal surfaces under reaction conditions from vacuum to high pressure.[102] The buried metal/liquid interface has also been explored albeit less frequently using this technique. For example, Somorjai and co-workers monitored the oxidation of CO on platinum surfaces in aqueous solution[104] and acetonitrile/water solutions[105] by SFG in combination with cyclic voltammetry. Similarly, Wieckowski, Dlott and co-workers used broadband SFG to study ethanol oxidation[106] at the aqueous/Pt interface. With regard to oxide

66

interfaces like silica, Ye and co-workers recently used SFG to study the dynamics of an enzyme catalyzed hydrolysis reaction of a phospholipid bilayer supported on planar silica.[107] However, covalent reactions of monolayers at the silica/solvent interface have not been explored using this technique despite its suitability.

One of the most tremendously widespread chemical transformations in materials chemistry is the Cu(I)-catalyzed Huisgen 1,3-dipolar azide-alkyne cycloaddition (CuAAC) developed by Fokin and Sharpless[165] and Meldal.[166] Due to its high yield, functional group tolerance, reasonable reaction rate, and lack of by-products, this reaction has been employed to functionalize many materials including polymers,[167] biomacromolecules,[168-169] nanoparticles[170-171] and mesoporous supports.[172] It also has been utilized to introduce different functional groups into monolayers on silica[162, 173-174] and other planar surfaces.[175-176] In addition to the staggering number of examples of utilizing CuAAC to introduce function into materials, the mechanism of the reaction has also been of research interest. Beginning with the original study of CuAAC by Sharpless and co-workers,[165] much work has been devoted to determining the mechanism of CuAAC in solution.[177-183] Multiple kinetic studies now support that the reaction is second-order in copper when performed at submillimolar copper concentrations.[181-182, 184] Additionally, a recent isotope labelling study indicates that the rate determining step involves a binuclear copper complex containing one copper-acetylide and another copper coordinated to both the azide and the acetylide species.[183] However, the mechanism of surface CuAAC, particularly on silica surfaces, is less well understood given the challenges in monitoring insulator interfaces. For semi-conductor and metallic substrates, the reaction appears to be first-order in azide for azide monolayers prepared on germanium[185] and gold.[186] Yet, the order of reaction with respect to copper has not been determined for any example of surface CuAAC.
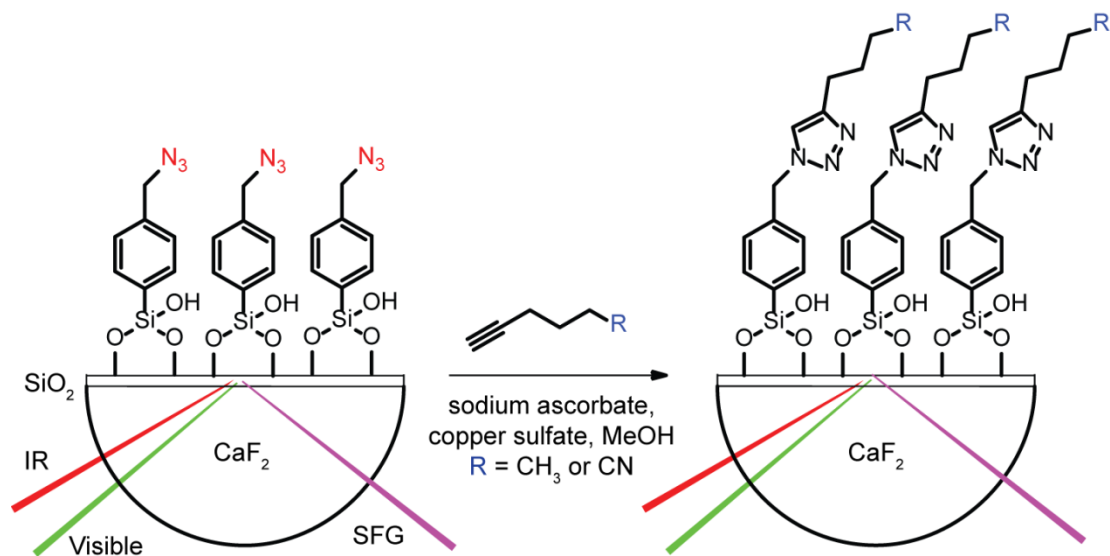
Figure 3.1 Monitoring CuAAC at the solid/liquid interface using broadband sum frequency generation.

In this project, the Cu(I)-catalyzed 1,3-dipolar azide-alkyne cycloaddition of an azide monolayer immobilized at the silica/methanol interface was directly monitored using sum frequency generation spectroscopy (Figure 3.1). The azide vibrational mode, never before observed by SFG, provides very strong signal indicating that it is an exceptional molecular handle for monitoring interfacial species by this technique. Finally, the dependence of the reaction profile on the catalyst concentration in solution has been evaluated, which indicates that the reaction on silica is second-order in copper.

3.2 Experimental Section

3.2.1 Materials

1-Hexyne, 5-hexynenitrile, copper(II) sulfate pentahydrate, and (+)-sodium L-ascorbate were purchased from Sigma-Aldrich; *p*-azidomethylphenyltrimethoxysilane (>90%) was

purchased from Gelest. These chemicals were used without further purification. HPLC grade methanol was purchased from Fisher Chemical and ultrapure deionized (18.2 MΩ•cm) water was used shortly after deionization by a Milli-Q-Plus ultrapure water purification system (Millipore).

3.2.2 Preparation of SiO$_2$ Thin Films on a CaF$_2$ Hemisphere

As shown in Figure 3.2, the IR spectrum of *p*-azidomethylphenyltrimethoxysilane exhibits a strong absorption at ~ 2100 cm^{-1}, which was assigned to the azide asymmetric stretch mode.[174, 187] This mode has been also observed in the Raman spectrum.[187-188] Although the azide asymmetric stretch mode is both IR and Raman active, it has never been directly observed by SFG.
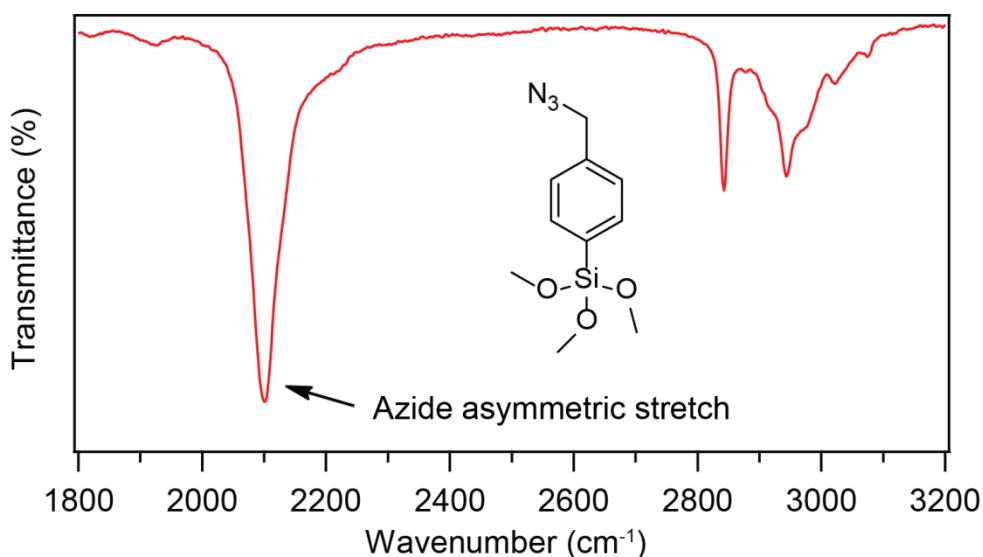
Figure 3.2 IR spectrum of *p*-azidomethylphenyltrimethoxysilane. The strong absorption at around 2100 cm^{-1} was assigned to the azide asymmetric stretch according to the literature.[174, 187-188]

In order to probe the azide asymmetric stretch mode using SFG spectroscopy, the broadband IR pulse should be centered around 2100 cm^{-1}. In SFG experiments, the most

commonly used solid substrate is IR grade SiO_2; however, it has a transmission range of 0.18-3.5 microns, or 2857-55556 cm^{-1}, which does not cover the region around 2100 cm^{-1}. To solve this problem, a CaF_2 hemisphere, which has a transmission range of 0.15-9.0 microns, or 1111-66667 cm^{-1}, was used as solid support. As surface silanol groups are required for the silanization of *p*-azidomethylphenyltrimethoxysilane, a SiO_2 thin film was deposited on top of the flat side of the CaF_2 hemisphere.

The formation of the SiO_2 film was achieved by electron beam vapor deposition using the method published by Ishibashi and co-workers.[189] A schematic graph of the modified CaF_2 hemisphere is shown in Figure 3.3. In order to increase the strength of the deposited SiO_2, a 3-nm Si layer was introduced between CaF_2 and SiO_2.[189] The thickness of the SiO_2 film was 125 nm.
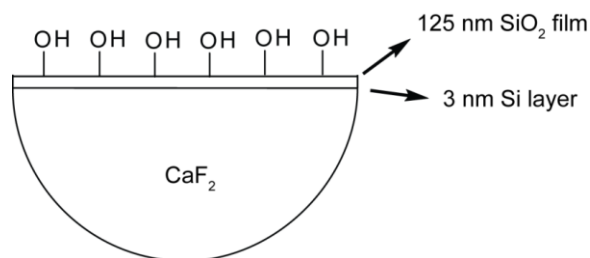
Figure 3.3 Schematic figure of the SiO_2 deposited CaF_2 hemisphere. A 3-nm Si layer was introduced between CaF_2 and SiO_2.[189] The thickness of the SiO_2 film was 125 nm.

The effectiveness of the generation of the SiO_2 film was verified by immersing the flat surface of the hemisphere with octadecyltrichlorosilane (ODS) toluene solution and then acquiring SFG spectra in the C-H stretching region. Practically, the flat surface of the hemisphere was immersed in an ODS/anhydrous toluene solution (1% v/v) at room temperature

for 10 min, then rinsed with toluene several times. Next, the hemisphere was air-dried and heated in an oven at 90 °C for 20 min.

SFG spectra from the air/ODS-SiO$_2$-CaF$_2$ interface are shown in Figure 3.4. Both ppp and ssp spectra exhibit strong signal intensity in the C-H stretching region, which mainly originates from the terminal methyl groups in the ODS layer formed on the surface.[190-191] The strong signal intensity indicated a SiO$_2$ film was effectively generated on top of the CaF$_2$ hemisphere.
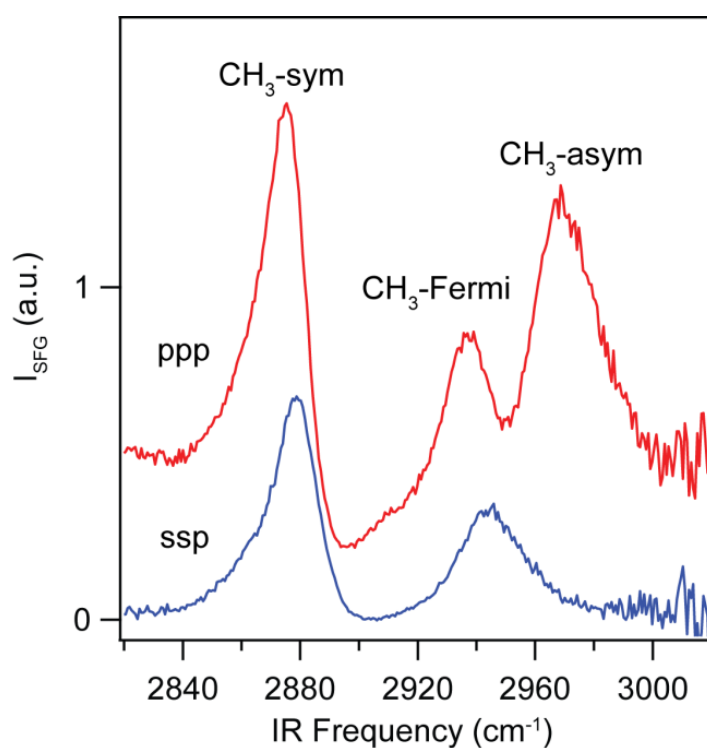
Figure 3.4 Normalized SFG spectra collected at the air/ODS-SiO$_2$-CaF$_2$ interface under both ppp and ssp polarization combinations. Three dominate peaks were observed, which originate from the terminal methyl groups in the surface ODS molecule. The peak at ~ 2880 cm^{-1} was assigned to methyl symmetric stretch (CH$_3$-sym), the peak at ~ 2940 cm^{-1} was assigned to Fermi resonance of methyl symmetric stretch (CH$_3$-Fermi), and the peak at ~ 2970 cm^{-1} was assigned to methyl asymmetric stretch (CH$_3$-asym).[190-191]

3.2.3 Preparation of Organic Azide Self-Assembled Monolayers

The azide monolayer was prepared according to our previously published method[141] using commercially available *p*-azidomethylphenyltrimethoxysilane. Briefly, the flat surface of the CaF_2 hemisphere was immersed in 3 mM *p*-azidomethylphenyltrimethoxysilane toluene solution (0.1 vol% water in dry toluene) for 4 hours. Then the silane solution was removed, and the hemisphere was rinsed rigorously with toluene, immersed in toluene for 30 min, sonicated for 5 min, and then rinsed with a 1:1 mixture of toluene/methanol and methanol. Finally, the hemisphere was blown dry under nitrogen and used immediately in an experiment.

3.2.4 Laser System and SFG Experimental Setup

Details about the SFG setup have been described in chapter 1. Briefly, as shown in Figure 3.5, our laser system consists of a femtosecond Ti:sapphire oscillator (Spectra-Physics, Mai Tai, 80 MHz), a Nd:YLF pump laser (Spectra-Physics, Empower) and a regeneratively amplified laser (Spitfire Pro, Spectra-Physics, 1 kHz, 100 fs, 3.3 W). Two-thirds of the output of the Spitfire (2.2 W) was used to pump a TOPAS-C/NDFG optical parametric amplifier (Spectra-Physics). The resulting broadband infrared light was tuned between ~2000 to 3000 cm^{-1} depending on the experiment. To generate visible light that was broadened to a picosecond pulse (FWHM ~10 cm^{-1}), we passed the Spitfire output through a Fabry-Perot etalon. The femtosecond IR light (~10-12 μJ/pulse) and the picosecond visible light (~10 μJ/pulse) were focused through a CaF_2 hemisphere (ISP optics, 1 inch diameter, CF-HS-25) at angles of 66° and 64°, respectively, from surface normal. The flat side of the CaF_2 hemisphere was coated with silica (125 nm) and then modified with a benzyl azide monolayer. This hemisphere was placed on a custom-built steel cell so that the flat surface of the hemisphere was perpendicular to the

laser table surface and in contact with methanol. Details about this sample cell have been described.[162] Reagent solutions were added via syringe, and the reaction mixture was mixed by drawing up and releasing the syringe several times. The SFG spectra at the functionalized silica/methanol interface corresponded to p-polarized SFG, p-polarized incident visible light and p-polarized incident IR light. Each spectrum was integrated for 1 minute and referenced to the spectrum collected from a CaF_2 sample containing a gold thin film in contact with air by dividing the spectrum from the azide monolayer by the gold spectrum.
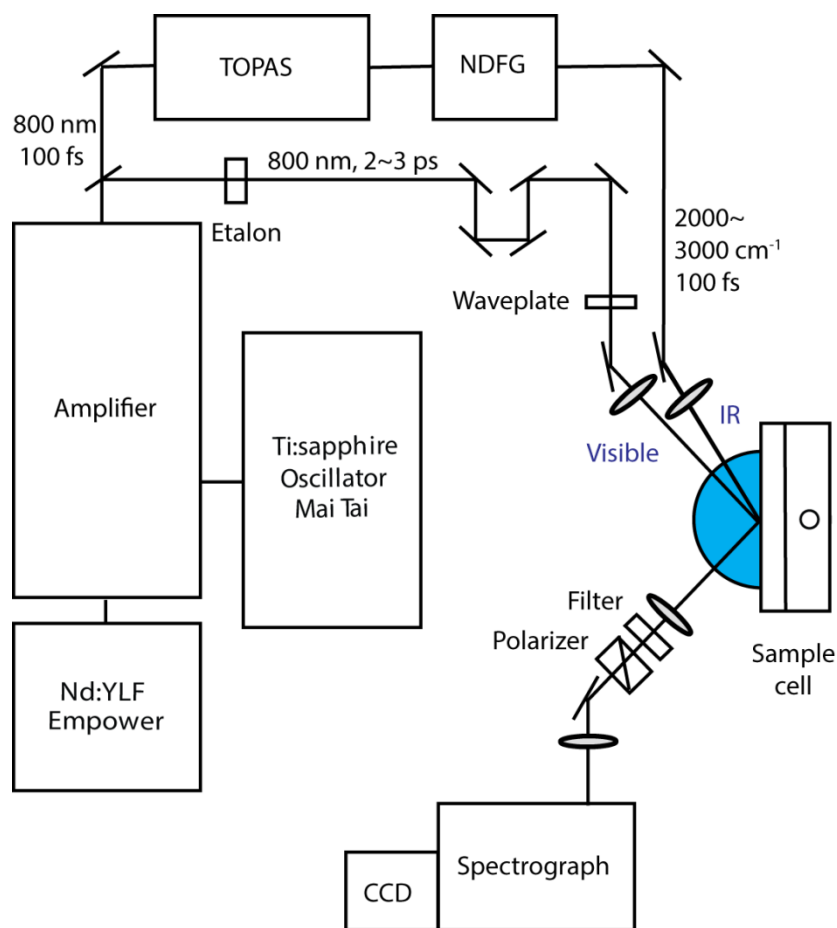
Figure 3.5 Schematic figure of the SFG experimental setup.

3.2.5 Monitoring CuAAC at the Interface with SFG

SFG was monitored at the air/gold/CaF$_2$ interface typically with an integration time of 20 seconds. The gold-coated hemisphere was then replaced with the azide-modified hemisphere, which was placed in contact with methanol in on our custom-built cell, and the SFG was monitored with the same incident IR and an integration time of 1 min. Next methanol was removed from the cell via syringe and the sample cell was filled with the alkyne methanol solution (1.2 mL) followed by certain amounts of the CuSO$_4$ in methanol and sodium ascorbate in water to reach the final desired concentrations of alkyne (1.50 mM) and CuSO$_4$ and sodium ascorbate. The solution was mixed by pulling and dispensing the reaction mixture into the syringe several times at which point the reaction time was started. The alkyne solution, the 5-mM CuSO$_4$ methanol solution and 10-mM sodium ascorbate aqueous solution were freshly prepared as stock solutions right before every experiment.

3.2.6 Procedure of SFG Spectra Fitting

The fitting of SFG spectra was accomplished using Igor Pro software: based on the number of vibrational modes and the corresponding peaks expected in the spectrum, a fitting function with the desired number of resonant $\chi_R^{(2)}$ terms and a non-resonant term $\chi_{NR}^{(2)}$ was chosen. For each fit initial A_v, ω_v, Γ_v and $\chi_{NR}^{(2)}$ were estimated and then the software was allowed to optimize all of these fit parameters; the returned values from the previous run were used as initial values for a second run. The fitting stopped when the returned values were the same as the previous input values. The reported amplitudes ± the standard deviations were returned from the fit.

3.3 Results and Discussion

3.3.1 SFG Spectra of Azide

The surface selectivity of sum frequency generation is intrinsic to the process as SFG is forbidden in centrosymmetric media but allowed in non-centrosymmetric media under the electric-dipole approximation.[62] For molecules oriented at an interface, centrosymmetry is broken. Consequently SFG can be used to study the kinetics of processes for these interfacial molecules, while effectively ignoring molecular species in the bulk phase not associated with the interface. For a molecule to be SFG active it must possess a vibrational mode that is both Raman and IR active.[57] The azide stretch meets this criteria,[174, 192] so we hypothesized that it would be observable by SFG.

A benzyl azide monolayer was prepared on silica according to our previously published method.[141] As fused silica is opaque in the region where the azide stretch is located ($\sim$2100 cm^{-1}), we prepared a SiO_2 thin film on a CaF_2 hemisphere using the method of Ishibashi and co-workers.[189] The functionalized SiO_2/CaF_2 hemisphere was then placed in contact with methanol in our custom-built cell and the broadband SFG was measured. We were pleased to observe a very strong transition at 2096 cm^{-1} that we assigned to the azide stretch. Moreover, the range of azide excitation was completely captured by the width of the IR pulse (FWHM $\sim$ 120 cm^{-1}). This allowed us to monitor the azide stretch in real time without varying the incident IR frequency.

Before performing an experiment, reference SFG spectra were first collected from the gold/air interface (Figure 3.6A) using the same type of CaF_2 hemisphere coated with 200 nm of gold placed in the sample cell without methanol. Then the spectrum at the same IR central wavelength was measured for the azide modified hemisphere/methanol interface (Figure 3.6A).

After subtracting the background, the intensity spectra were divided by the gold reference spectra and then fit with:[81, 193]

$$I_{SFG} \propto \left| \chi^{(2)} \right|^2 = \left| \chi_{NR}^{(2)} + \sum_v \chi_R^{(2)} \right|^2 = \left| \chi_{NR}^{(2)} + \sum_v \frac{A_v}{\omega_{IR} - \omega_v + i\Gamma_v} \right|^2 \tag{3.1}$$

where $\chi_{NR}^{(2)}$ and $\chi_R^{(2)}$ are the non-resonant and resonant contributions to the second-order susceptibility, and $\chi_R^{(2)}$ can be expressed as a summation over all frequencies (v) with ω_{IR} as the frequency of the incident IR field, A_v, ω_v and Γ_v as the amplitude, frequency, and damping coefficient of the vth surface vibrational mode, respectively. The normalized SFG spectrum of azide was shown in Figure 3.6B.
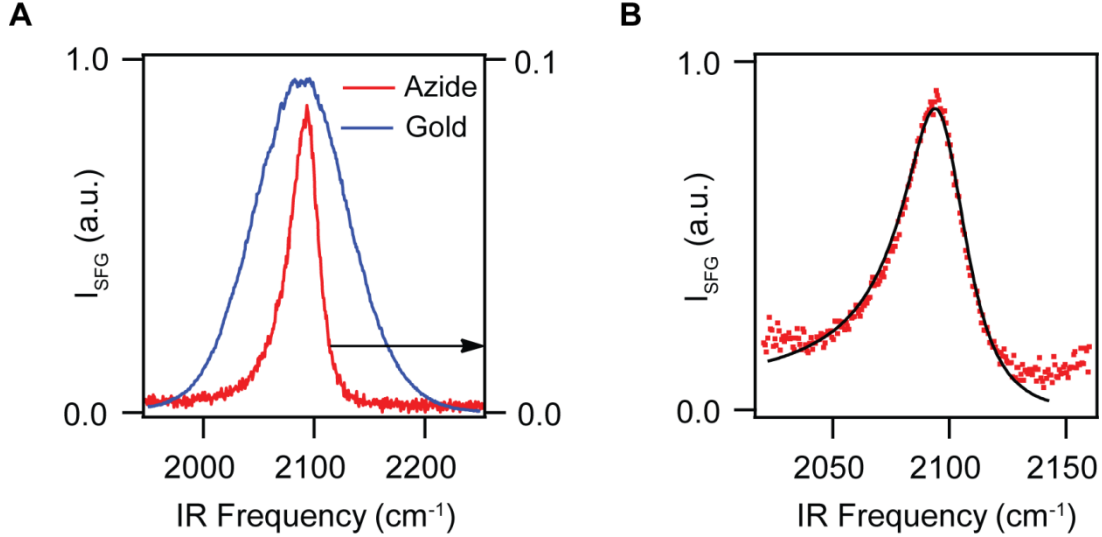
Figure 3.6 Normalization of azide SFG spectra. (A) The SFG spectrum collected at the CaF_2-gold/air interface and the SFG spectrum collected at the CaF_2-SiO_2-azide/methanol interface using the same IR pulse. (B) Normalized azide SFG spectrum and theoretical fit with equation 3.1.

When the IR frequency matches the center frequency of a vibrational mode, the peak amplitude, A_v, can be related to the number density of the corresponding oscillators N_s according to:

$$A_v \propto N_s \langle \beta^{(2)} \rangle \tag{3.2}$$

where $\langle \beta^{(2)} \rangle$ is the hyperpolarizability averaged over all molecular orientations. Assuming $\langle \beta^{(2)} \rangle$ remains constant with coverage, then the amplitude A_v is directly proportional to the number density of molecular oscillators that are ordered at the interface. Consequently, changes in the SFG intensity and in turn $\chi^{(2)}$ can be directly related to the disappearance or appearance of interfacial reactants.
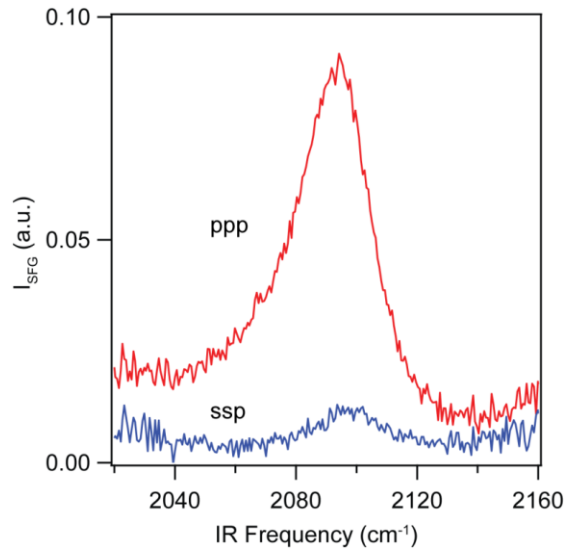
Figure 3.7 Normalized SFG spectra collected at the CaF_2-SiO_2-azide/methanol interface under ppp and ssp polarization combinations.

Figure 3.7 shows the normalized SFG spectra measured for the azide modified hemisphere/methanol interface under ppp and ssp polarization combinations. The azide modified

SiO$_2$-CaF$_2$ hemisphere possesses symmetry of $C_{\infty v}$, and there are only three unique non-zero second-order nonlinear susceptibility tensor elements, which are $\chi^{(2)}_{ZZZ}$, $\chi^{(2)}_{XXZ}\left(=\chi^{(2)}_{XZX}\right)$ and $\chi^{(2)}_{ZXX}$,[64, 69, 73] Under ppp polarization combination, all three elements are probed, while under the ssp polarization combination, only $\chi^{(2)}_{XXZ}$ is probed. As shown in the figure, under the ppp polarization combination, the azide asymmetric stretch peak has much stronger SFG intensity. For kinetic analysis, SFG spectra under the ppp polarization combination were collected due to the relatively high intensity.

3.3.2 CuAAC between Azide Monolayer and 1-Hexyne

As shown in Figure 3.8, the first CuAAC we studied was the reaction between the azide monolayer and 1-hexyne, in which copper sulfate, and the reducing agent sodium ascorbate were used to generate the Cu(I) catalyst. In the presence of 1-hexyne, copper sulfate, and sodium ascorbate, the azide peak completely disappeared after five hours (Figure 3.8). After fitting, the normalized peak amplitude, which is proportional to the number density of the surface azide molecule, was plotted versus time revealing a sharp decrease during the course of the reaction (Figure 3.9). In contrast, the azide peak amplitude remained prominent after being exposed to only 1-hexyne and copper sulfate for five hours in the absence of sodium ascorbate, which indicated that the disappearance of the azide was due specifically to the copper-catalyzed cycloaddition at the interface.
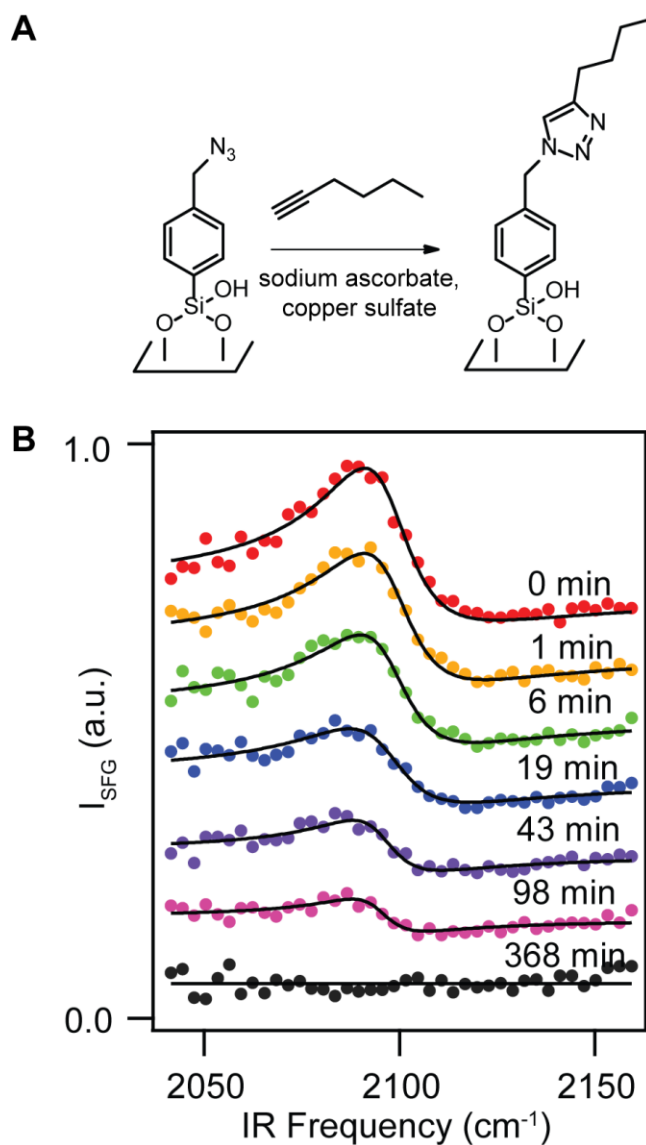
Figure 3.8 (A) The CuAAC of 1-hexyne with the azide-modified monolayer. (B) Normalized SFG spectra as a function of time revealing the azide stretch (2096 cm^{-1}). The lines are the fit of equation 3.1 to the data. *Reaction Conditions*: [1-hexyne] = 1.50 mM; [CuSO$_4$] = 0.021 mM, [sodium ascorbate] = 0.042 mM.
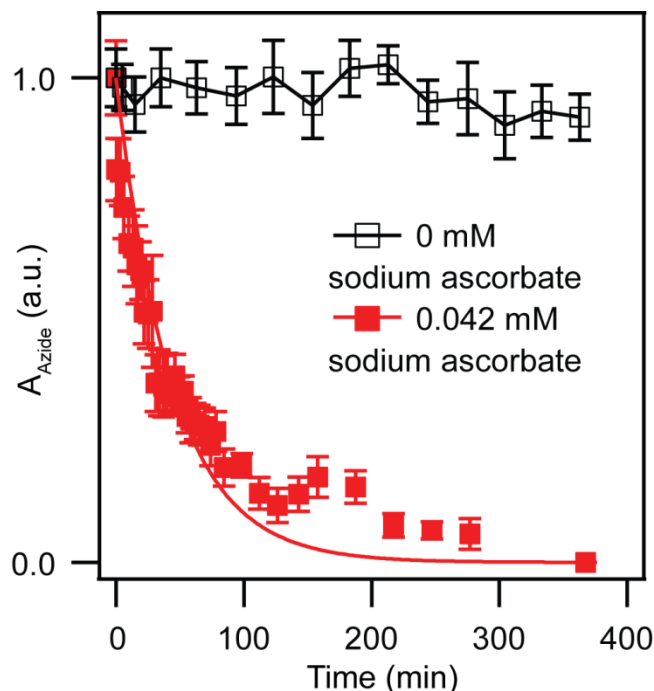
Figure 3.9 Normalized azide peak amplitude as a function of time during the reaction of the azide monolayer with 1-hexyne. The line represents the fit using equation 3.1. *Reaction Conditions*: [1-hexyne] = 1.50 mM; [CuSO$_4$] = 0.021 mM, [sodium ascorbate] = 0.042 mM. Under this condition, the apparent rate constant was determined to be 0.0229 ± 0.0001 min^{-1}.

To quantify the rate of this reaction and gain information about the order of the reaction in azide, the normalized azide peak amplitude versus time was fit with a pseudo-first-order rate law (Figure 3.9), which has an expression as follows:

$$A(t) = e^{-k't} \tag{3.3}$$

where k' is the apparent rate constant. The pseudo-first-order rate law fit the kinetic data well, indicating that under the given reaction conditions, the CuAAC is first order in the surface azide. As the alkyne was in large excess relative to the azide, the reaction rate only changed throughout the reaction as azide was consumed consistent with pseudo-first order conditions.

SFG spectra in the C-H stretching region for the benzyl azide monolayer before and after reaction with 1-hexyne were also collected. Before the reaction the most prominent peak was

present at ~ 2840 cm^{-1}, attributed to the methylene symmetric stretch of the benzyl group (Figure 3.10A). After CuAAC, a new peak at 2870 cm^{-1} appeared associated with the methyl group symmetric stretch (Figure 3.10B). The broad peak between 2910 cm^{-1} and 2950 cm^{-1} also changed in intensity owing to contributions from the Fermi resonance of the methyl stretch and the asymmetric stretch of the additional methylene groups present in the butyl substitution on the triazole.
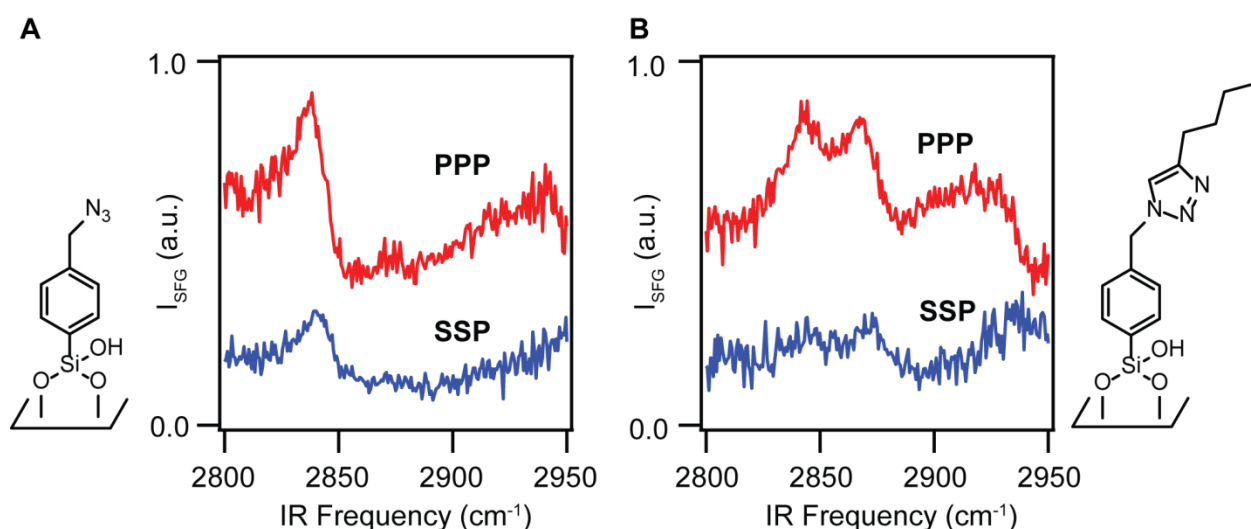
Figure 3.10 SFG spectra in the C-H stretch region. (A) Normalized SFG spectra for the benzyl azide monolayer at the solid/air interface under ppp and ssp polarization combinations. (B) Normalized SFG spectra of the same monolayer after reaction with 1-hexyne for ~ 5 hours under ppp and ssp polarization combinations. After reaction, the sample surface was rinsed with methanol several times and then dried under N$_2$. Each spectrum in A and B had an integration time of 5 min. *Reaction Conditions*: [1-hexyne] = 1.50 mM, [CuSO$_4$] = 0.021 mM, [Na ascorbate] = 0.042 mM.

3.3.3 CuAAC between Azide Monolayer and 5-Hexynenitrile

As shown in Figure 3.11, the second CuAAC we studied was the reaction between the azide monolayer and 5-hexynenitrile, where once again copper sulfate, and the reducing agent sodium ascorbate were used to generate the Cu(I) catalyst.
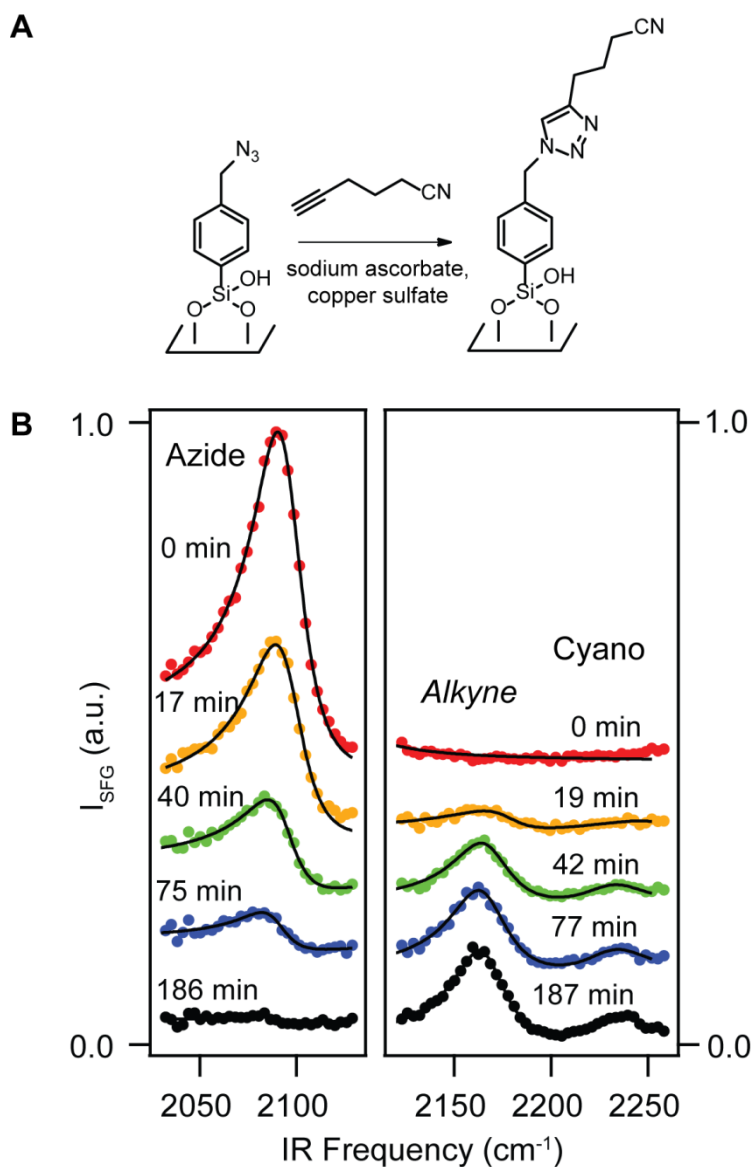
Figure 3.11 (A) CuAAC of 5-hexynenitrile with the azide-modified monolayer. (B) Normalized SFG spectra as a function of time in the azide (left) and the cyanide (right) stretch region. The lines are the fit of equation 3.1 to the data. The peak at 2166 cm^{-1} is tentatively assigned to the unreacted alkyne functional group. *Reaction Conditions*: [5-hexynenitrile] = 1.50 mM; [CuSO4] = 0.06 mM, [sodium ascorbate] = 0.12 mM.

5-Hexynenitrile possessed a cyano group with a vibrational mode close to that of the azide (CN: ~ 2230 cm^{-1}). Therefore, IR pulses centered at two different frequencies covering the range

between 2000 cm^{-1} and 2300 cm^{-1} were alternated every minute using our computer-controlled OPA (TOPAS), which allowed us to probe the azide peak and cyano peak nearly simultaneously (Figure 3.11). The cyano peak was observed to have a central frequency of 2234 cm^{-1} similar to reported values from other SFG studies of CN groups at interfaces.[194-195] As expected, no contribution from the cyano peak was observed in the absence of catalyst despite its presence in the solvent phase, which supports that the cyano groups only became oriented upon reacting with the surface monolayer.

3.3.4 Identification of the Peak at 2166 cm^{-1}

Between the azide peak and the cyano peak, a new peak was also observed at 2166 cm^{-1} (Figure 3.11 and 3.12A), and its intensity increased as the reaction proceeded. We found that washing the surface with methanol several times significantly reduced the intensity (Figure 3.12B). In order to determine its origin, control experiments were done. The completely reacted surface was treated with 5-hexynenitrile methanol solution for 20 min, and then SFG spectra were then collected from the solid/liquid interface (Figure 3.12C), which did not lead to the reappearance of the peak at 2166 cm^{-1}. However, upon introducing copper sulfate and sodium ascorbate with 5-hexynenitrile the peak reappeared (Figure 3.12D).
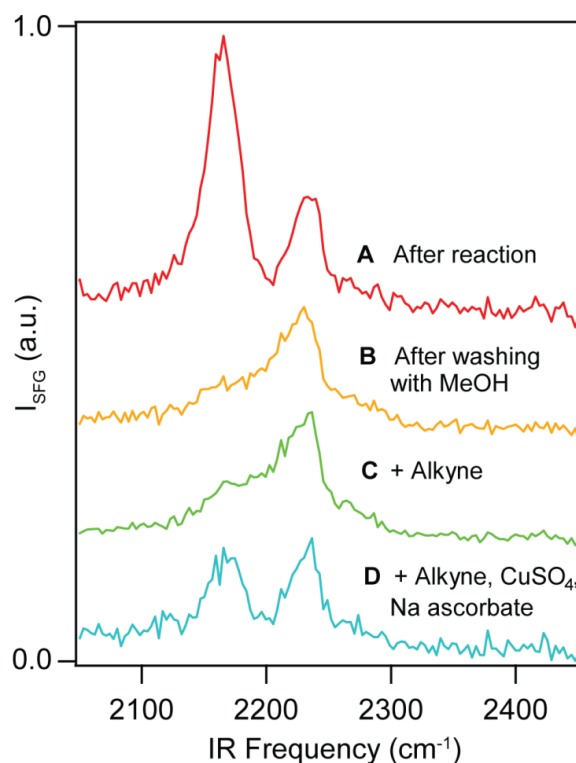
Figure 3.12 Un-normalized SFG spectra from: (A) a completely reacted benzyl azido monolayer with 5-hexynenitrile; (B) after washing the same surface several times with methanol; (C) after introducing 1.50 mM 5-hexynenitrile; (D) after introducing 1.50 mM 5-hexynenitrile, 0.06 mM copper sulfate and 0.12 mM sodium ascorbate. The same sample was used in A-D and was washed several times with methanol between the spectra collected in part C and D. Each spectrum had an integration time of 1 min.

Based on these observations, we attributed this peak to an alkyne present at the interface, although it appeared ~30 cm^{-1} higher than what has been previously observed for propiolic acid by SFG.[196] This peak, however, was not observed in the SFG spectra after reaction with 1-hexyne. We reason that it was only observed for the reaction with 5-hexynenitrile owing to the cyanide group and its ability to form a coordination complex with metal ions at the interface.[197-203] If this complex contains the cyanide on the surface and a copper ion coordinated to another unbound 5-hexynenitrile through the CN group, it results in an unreacted alkyne at the interface

(Figure 3.13). This metal-ligand complex would be weakly associated, so the unreacted alkyne would be rinsed away with methanol washes.
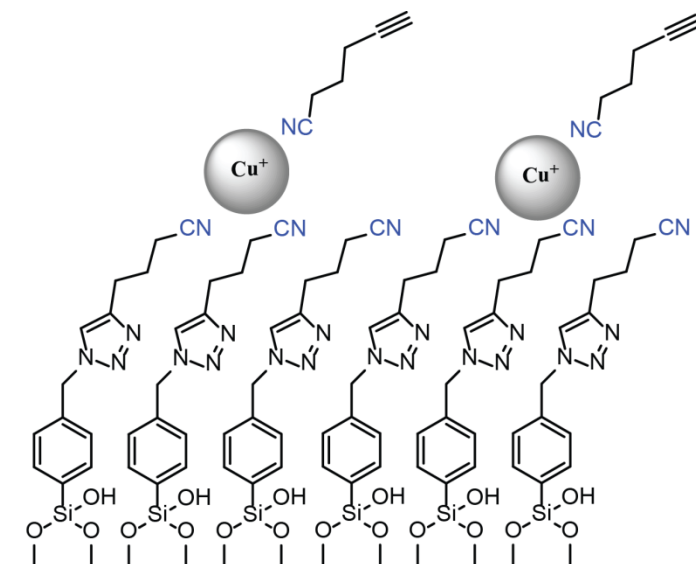
Figure 3.13 Schematic figure describing the origination of the peak at 2166 cm^{-1}. The cyanide on the surface coordinates with a copper ion, which coordinates to another unbound 5-hexynenitrile through the cyanide group, resulting in an unreacted alkyne at the interface.

3.3.5 Reaction Order with Respect to Copper Catalyst

For the reaction between azide monolayer and 5-hexynenitrile at the interface, to determine the reaction order with respect to the copper catalyst, the copper concentration was varied. A similar approach for assessing the order of reaction for one of the solution-phase components was reported for the Diels-Alder reaction on gold.[204] As expected the decay of the azide peak occurred more quickly upon increasing the copper sulfate and sodium ascorbate concentration.

As previously discussed, the mechanism of this click reaction has been widely studied in solution and has been found to be first order in azide and second order in copper.[181] To assess the reaction order at the interface, the amplitude of the azide and cyano peaks were determined from

separately fitting the SFG spectra corresponding to the two incident IR frequencies. The normalized peak amplitudes were plotted versus time, which revealed that the cyano peak increased while the azide peak decreased during the course of the reaction (Figure 3.14). The disappearance of the azide peak and the appearance of the cyano peak fit well to a first order rate law (Figure 3.14), indicating that the catalyst and the alkyne in solution were in great excess compared with the azide on the surface resulting in pseudo-first-order kinetics.[171, 185-186]
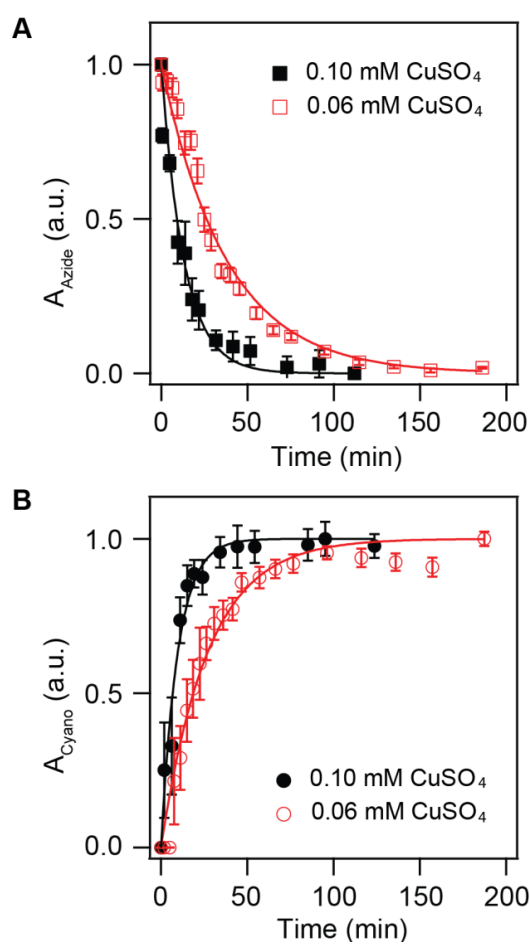
Figure 3.14 The normalized (A) azide and (B) cyano peak amplitudes versus reaction time, and the corresponding fits with a pseudo-first order rate equation at high (filled) and low (hollow) catalyst concentrations. *Reaction Conditions*: [5-hexynenitrile] = 1.50 mM; [CuSO$_4$] = 0.06 mM, [sodium ascorbate] = 0.12 mM (lower concentration); [CuSO$_4$] = 0.10 mM, [sodium ascorbate] = 0.20 mM (higher concentration).

In Figure 3.14, the normalized azide peak amplitude versus time was fit with equation 3.3; similarly, the normalized cyano peak amplitude versus time was fit with a pseudo-first-order rate law with the expression as follows:

$$A(t) = 1 - e^{-k't} \qquad (3.4)$$

where k' is the apparent rate constant. This form of the integrated rate law is suitable for interpreting the formation of the product rather than the exponential decay of the reactant.

Table 3.1 Apparent Rate Constants k' Determined from the Fitting of the Normalized Azide Peak Amplitude versus Time under Different Copper Concentrations. (Corresponding fittings are shown in Figure 3.14A.)

Copper concentration / mM	k' / min^{-1}
0.06	0.026 ± 0.001
0.10	0.076 ± 0.006

The general rate law for CuAAC can be expressed as follows:

$$r = k[Azide]^a[Alkyne]^b[Copper]^c \qquad (3.5)$$

where k is the rate constant, and a, b and c are the reaction orders with respect to reactant azide, alkyne and catalyst copper, respectively. When the surface azide is the limiting reagent, equation 3.5 can be modified as follows:

$$r = k'[Azide]^a \qquad (3.6)$$

where k' is the apparent rate constant, which has an expression of $k' = k[Alkyne]^b[Copper]^c$ and is the same as the apparent rate constant determined from fitting.

The apparent rate constants determined from fitting in Figure 3.14A are shown in table 3.1. Specifically, when the concentration of the copper ion was increased by a factor of 1.7 (from 0.06 mM to 0.10 mM), the pseudo-first-order rate constant was found to increase from 0.026 ± 0.001 to 0.076 ± 0.006 min^{-1}. This factor of 2.9 indicated that the reaction order for copper ion was 2.1, which is consistent with the value of two found for the reaction in solution.[181] A similar value was determined from the cyano peak amplitude data (Figure 3.14B). The fact that the surface reaction is also second order in copper, as observed in solution, suggests that two copper ions are present in the rate-determining step on the surface despite the more crowded environment.

3.4 Conclusion

In conclusion, we have found that the azide group and its reactivity can be followed in real time using vibrational SFG. By tuning the catalyst concentration, the time required to completely react the azide monolayer can be reduced to one hour. Additionally, kinetic analysis reveals that the surface reaction is second order in copper and first order in azide similar to the reaction in solution. This study lays the groundwork for further investigations of the mechanism of the interfacial click reaction and how parameters such as monolayer orientation influence the surface reactivity. Moreover, it establishes that SFG spectroscopy is well suited to follow the dynamics of monolayer reactions at buried oxide/liquid interfaces.

Finally, we note that the azide group resulted in much stronger SFG intensity than the cyano group. The unique vibrational signature of cyano groups and their SFG activity have made this group useful in monitoring the position and orientation of specific molecules at the interface.[194-195, 205-206] As the azide is bio-orthogonal (i.e. unreactive with functional groups that occur in

biological systems), and possesses a vibrational stretch with $C_{\infty v}$ symmetry in an uncongested region of the IR spectrum like CN, it is also a suitable candidate for such labeling experiments. Moreover, its strong SFG activity indicates that it is an even better label than cyanide.

Chapter 4

The Thermal Reorganization of DNA Immobilized at the Silica/Buffer Interface: A Vibrational Sum Frequency Generation Investigation

Portions of this chapter are reproduced with permission

from the Royal Society of Chemistry (RSC)

4.1 Introduction

Many biodiagnostic platforms involve the molecular recognition between an immobilized DNA sequence and a complementary oligonucleotide in solution.[207-209] Despite the widespread application of such DNA chips, studies aimed at understanding the structure and hybridization behavior of immobilized DNA, particularly on silica, have lagged behind the corresponding solution-phase measurements owing to the inherent difficulty in monitoring processes at the solid/liquid interface.[210-213] Indeed, little is known about how the structure of DNA varies with temperature although thermal stringency washes are typically employed in assays utilizing immobilized DNA chips.[214] Consequently, most of these assays follow steps based on empirical evidence that correlate the temperature, hybridization time and other experimental conditions with the most selective detection.

Over the past few decades, several vibrational spectroscopic techniques have evolved as powerful tools to probe unlabelled DNA at surfaces and interfaces.[42, 44, 215-217] For example, surface selective IR absorbance spectroscopy has been used to gain structural information about immobilized, unlabeled DNA complexes, which led to the identification of particular vibrational modes that corresponded to the surface-bound and hybridized strand.[37-41] However, examples of real-time hybridization measurements of DNA immobilized on substrates, particularly silica, remain scarce owing to the difficulty in distinguishing the hybridizing strand from non-interacting strands within the volume probed by the evanescent field.

To distinguish between those strands hybridized at the interfaces versus those present in the probe volume, nonlinear optical methods have a great advantage as only molecules with net orientation lead to observable generation of second-order processes. As a result of this intrinsic surface sensitivity and amenability to insulator substrates like silica, the nonlinear optical

methods sum frequency generation (SFG) and second harmonic generation (SHG) have been widely used to probe DNA at the air/liquid, solid/air, and solid/liquid interface.[217] Regarding the former, Bonn and co-workers have explored the structure of water around DNA interacting with lipid monolayers present at the air/aqueous interface using sum frequency generation.[218-219] At the silica/liquid interface, most relevant to DNA chips used in biodiagnostics, Geiger and co-workers have led the way in utilizing SHG to understand the behavior of DNA.[217, 220-226] Specifically, the strand density and ion affinity of single-stranded DNA immobilized at the interface has been explored with the $\chi^{(3)}$ technique of Eisenthal[50] based on changes in the non-resonant SHG signal with electrolyte composition and concentration.[221, 223-226] In complementary studies using resonantly enhanced SHG, the linear dichroic ratio was also found to be sensitive to the extent of hybridization of the surface immobilized strand.[220] Consequently, hybridization could be observed in real time utilizing this spectral handle. Resonantly enhanced SHG has also proven useful to detect the interactions of drug molecules with immobilized duplex DNA.[227] Additionally, we recently employed resonantly enhanced SHG to monitor hybridization at DNA-functionalized silica using a solution-phase strand modified with an SHG-active label distinct from the spectroscopic signature of DNA.[162] With this system, the temperature-dependent stability of the duplex was assessed as well as the reversibility of binding during salt stringency washes.

Vibrational SFG has also been utilized to monitor DNA at the solid interface albeit not at the silica/aqueous interface despite its widespread importance.[228] For example, DNA at the silica/air interface was monitored by SFG by Geiger and co-workers.[173, 229] Similar to their SHG work, they found that the chiral SFG response was particularly sensitive to the structure of the DNA duplex and could distinguish between the direction of polyadenosine:polythymidine

duplexes (which sequence was attached to the surface) owing to the resulting difference in the chiral arrangement of the methyl groups.[229] Koelsch and Zharnikov have explored the SFG of DNA immobilized on gold surfaces.[230-231] Interestingly, none of these studies took advantage of the real-time potential of SFG to monitor the rate of hybridization or changes in the structure as experimental parameters like temperature were varied.

Here we report monitoring immobilized oligonucleotides at the silica/buffer interface in real time as a function of temperature and aqueous composition using vibrational sum frequency generation in the C-H stretching region (2850-3000 cm^{-1}). We find that the nucleobases exhibit net order even prior to hybridization for immobilized single strands. Moreover, varying the temperature of the hybridized samples leads to spectral changes from the thymine nucleobases that were consistent with duplex dissociation.

4.2 Experimental Section

4.2.1 Laser System and Experimental Setup

A detailed description of our SFG setup has been described in Chapter 2 and 3, and the design of the temperature-variable solid/liquid sample cell has been described in a previously published paper.[162] Generally, the amplified 798-nm light pulses from the Spitfire were passed through a 30/70 beam splitter, and 2.3 W was used to pump a non-collinear optical parametric amplifier (TOPAS-C and NDFG, Light Conversion) to generate light in the IR region, while some of the remaining 798-nm light passed through a Fabry-Perot etalon (TecOptics) to generate picosecond pulses (full width half maximum of 10 cm^{-1}). Each beam was focused at the sample using a CaF_2 (focal length = 500 mm, Thorlab) or BK7 (focal length = 400 mm, Thorlab) focusing lens, respectively. The IR polarization was horizontal to the table therefore

perpendicular to the sample plane from the TOPAS NDFG (*p*-polarized), and the visible polarization was set to *p* or *s* using a half-wave plate (Thorlabs). Pulse energies of 10-20 µJ/pulse of visible and ~10-20 µJ/pulse of IR were used, and the beams were slightly defocused to minimize sample damage. The infrared (fs) and visible (ps) pulses were directed through the IR grade silica hemisphere at incident angles of 66° and 64° with respect to surface normal. The sample cell was designed to place the flat surface of the hemisphere perpendicular to the laser table. This vertical arrangement allowed us to change the solvent at the interface without requiring a flow setup.

For all of the experiments, only one TOPAS-NDFG setting was used to collect the spectra centered near 2900 cm^{-1}. For data acquisition, 4W × 10H or 5W × 10H binning was used to reduce the noise and the data were acquired for 3-10 min per spectrum. The spectra shown in the figures are representative of at least two experiments.

4.2.2 Sample Preparation

All oligonucleotides were synthesized on a solid-phase synthesizer (ABI 390) using reagents from Glen Research. All of the strands used contained a 5'-alkyne modified thymidine (Glen Research, Catalog No:10-1540-95) followed by the T$_{15}$ or A$_{15}$ sequence. This modified thymidine lacked a methyl group owing to the placement of the alkyne substituent.

The benzyl azide monolayer for immobilizing the alkyne DNA was prepared following our previous publication with an increased reaction time between the *p*-azidomethylphenyltrimethoxysilane in toluene and the freshly cleaned silica surface to increase the monolayer density.[141] Additionally, for all experiments performed at the solid/air interface, we utilized commercially available *p*-azidomethylphenyltrimethoxysilane (Gelest) rather than

synthesize our own. Briefly, the flat surface of the freshly cleaned silica hemisphere was immersed in 3 mM *p*-azidomethylphenyltrimethoxysilane toluene solution (0.1 vol% water in dry toluene) for ~ 15 hours. Then the silane solution was removed, and the hemisphere was rinsed rigorously with toluene, immersed in toluene for 30 min, sonicated for 5 min, and then rinsed with a 1:1 mixture of toluene/methanol and methanol. Finally, the hemisphere was blown dry under nitrogen and used immediately in an experiment.

The oligonucleotides were immobilized on top of the benzyl azide modified silica hemisphere through copper(I) catalyzed azide-alkyne cycloaddition. A mixture of $CuSO_4$-TBTA-TCEP (1:1:1 mole ratio) was prepared as catalyst based on the method proposed by Sun and co-workers[232] with modification. First of all, 1.1 mg (2 µmol) of tris-(benzyltriazolylmethyl)amine (TBTA) was dissolved in the mixture of 137.5 µL DMSO and 12.5 µL t-BuOH, followed by the addition of 50 µL $CuSO_4$ stock solution (40 mM $CuSO_4$, 0.3 M NaCl). Then 0.6 mg (2 µmol) of tris(carboxyethyl)phosphine (TCEP) was dissolved in 100 µL 0.3 M NaCl solution and then mixed with the TBTA solution to yield a greenish yellow solution. 30 nmol of alkyne-terminated DNA was dissolved in the mixture of 100 µL PBS buffer (0.3 M NaCl, pH 7.0) and 100 µL DMSO in a 0.6-mL Eppendorf tube. The 300-µL catalyst mixture was then added into the Eppendorf tube containing the alkyne-DNA and the tube was vortexed to obtain a transparent solution. The total volume of the DNA/catalyst solution was 500 µL, and the concentration of the DNA was 60 µM.

The benzyl azide modified silica hemisphere was treated with the DNA/catalyst solution overnight, and then was rinsed with the following solvents in the order as written: water, water/ethanol, ethanol, ethanol/DMSO, DMSO, ethanol/DMSO, ethanol, water/ethanol and

water to completely remove any unreacted DNA. Finally, the samples were blown dry with a stream of nitrogen.

4.2.3 Spectral Normalization

The spectra shown in Figure 4.6, 4.8A, 4.11A, 4.12 and 4.13A were normalized as follows: After background subtraction, each spectrum from the DNA-silica/buffer aqueous salt interface was divided by the corresponding spectrum from the same sample at the pure water interface, as the signal was dominated by the water peak at low salt concentration. As shown in Figure 4.1, the spectrum of the DNA-modified silica/water interface has a similar Gaussian shape as that from the silica/gold interface, so we can use the DNA-modified surface/water interface to determine the shape of the IR pulse. This procedure has the advantage of not requiring sample replacement to collect the reference spectrum, which can introduce error due to imperfect realignment between the actual and reference samples.
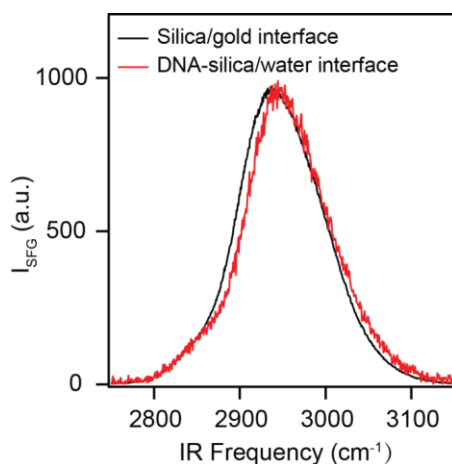
Figure 4.1 SFG spectrum from the DNA-silica/water interface compared with that from the silica/gold interface. The maximum intensities have been normalized to the same value as greater signal is always observed from the silica/gold interface owing to its greater second-order susceptibility compared with the silica/water interface.

The spectra shown in Figure 4.7 were normalized to the silica/gold interface, as gold exhibits strong non-resonant signal independent of IR wavelength. This referencing was achieved by dividing the spectra from DNA-functionalized sample with the spectrum measured immediately before from a gold-coated silica hemisphere at the same IR central wavelength (the same TOPAS-NDFG settings).

4.2.4 Spectral Fitting

The following equation was employed to fit the SFG spectra. The second order susceptibility $\chi^{(2)}$ is broken down into a non-resonant term $\chi_{NR}^{(2)}$, and vibrational resonant term $\chi_{R}^{(2)}$ summed over all possible wavenumbers. Each resonant mode is considered to possess a Lorentzian lineshape as shown below:

$$I_{SFG} \propto \left|\chi^{(2)}\right|^2 = \left|\chi_{NR}^{(2)} + \sum_v \chi_R^{(2)}\right|^2 = \left|\chi_{NR}^{(2)} + \sum_v \frac{A_v}{\omega_{IR} - \omega_v + i\Gamma_v}\right|^2 \tag{4.1}$$

Here ω_{IR} is the wavenumber of the incident IR beam, and A_v, ω_v, and Γ_v are the amplitude, frequency, and damping coefficient of the vth surface vibrational mode, respectively. The fitting was accomplished using Igor Pro: based on the number of vibrational modes expected in the region, a function with the desired number of resonant terms and a non-resonant term was chosen for fitting. For each fitting, initial A_v, ω_v, Γ_v and $\chi_{NR}^{(2)}$ values were estimated around the central wavenumbers noted in the manuscript and then the software was allowed to optimize all of them; the returned values from the previous run were used as initial values for a second run. The fitting stopped when the returned values were the same as the previous input values. Then for the last

run, all ω_v values were held as constants and the values of other parameters were obtained from fitting.

4.2.5 Melting of T$_{15}$:A$_{15}$ Duplex in Solution Phase Monitored Using UV-Vis Spectroscopy

For the DNA duplex melting experiment in solution, 0.61 nmol of each DNA sequence was mixed in 1.0 ml PBS buffer (0.5 M NaCl, 10 mM PBS, pH 7.0), and was allowed to equilibrate for 1 hour. The melting experiments were performed using an Agilent 8453 UV-Visible Spectroscopy System fit with a Peltier temperature controller. Absorbance readings were taken at 260 nm with 1 °C intervals from 20 to 70 °C. The hold time at each temperature was 1 min. The solution was stirred at 250 rpm during the temperature-variation experiment.

4.3 Results and Discussion

4.3.1 Experimental Design for Monitoring DNA Hybridization at the Silica Interface

Similar to the work of Geiger[229] and Koelsch and Zharnikov,[231] we utilized a polythymidine 15mer (T$_{15}$) and polydeoxyadenosine 15mer (A$_{15}$) as our complementary sequences to isolate CH$_3$ functional groups onto either the immobilized or solution-phase strand as methyl groups only appear on thymidine (T) of the four canonical deoxyribonucleotides. (Figure 4.2) Utilizing an attachment strategy developed in our group, we immobilized the DNA onto the silica surface using an alkyne-terminated thymidine, which could be reacted with a benzyl azido monolayer to generate the DNA-functionalized surface.[162] Unlike many other linker strategies, this attachment method only introduced one methylene group per reactive site on the silica from the benzylic position of the benzyl azide. Consequently, we were able to attribute most of the observed SFG

to the oligonucleotides and not the initial monolayer. As will be discussed, this is an advantage over other systems where the linker contributed significantly to the observed signal.[228-229]

Vibrational sum frequency generation occurs when two incident fields, one in the visible, the other in the infrared, are temporally and spatially overlapped in a noncentrosymmetric medium like an interface.[50, 54] New light is generated at a frequency that is the sum of the two incident frequencies. The intensity of this sum frequency signal (I_{SFG}) is proportional to the incident visible (I_{vis}) and IR (I_{IR}) intensities according to:

$$I_{SFG} \propto \left|\chi^{(2)}\right|^2 I_{vis}I_{IR} = \left|\chi_{NR}^{(2)} + \sum_v \chi_{R_v}^{(2)}\right|^2 I_{vis}I_{IR} \tag{4.2}$$

where $\chi^{(2)}$ is the second-order susceptibility of the system. Within the electric dipole approximation, $\chi^{(2)}$ requires a break in inversion symmetry to be non-zero. Thus, SF signal generated at the interface can be attributed to molecules with a net orientation. $\chi^{(2)}$ can be broken down into two components, one non-resonant ($\chi_{NR}^{(2)}$) and the other resonant ($\chi_R^{(2)}$).

As shown in equation 4.3 and 4.4, $\chi_R^{(2)}$ is proportional to the number density of molecular oscillators (N) and is resonantly enhanced when the IR frequency (ω_{IR}) approaches the frequency of a vibrational mode (ω_v) that is both IR and Raman active.[233]

$$\chi_{R_v}^{(2)} \propto N\left\langle\beta_v^{(2)}\right\rangle \tag{4.3}$$

$$\beta_v^{(2)} \propto \frac{\alpha_v\mu_v}{\omega_v - \omega_{IR} - i\Gamma_v} \tag{4.4}$$

Here, $\left\langle\beta_v^{(2)}\right\rangle$ is the orientationally averaged molecular hyperpolarizability, μ_v is the IR

transition dipole moment, α_v is the Raman polarizability tensor, and Γ_v is the natural line width of the transition. In our experimental set-up, we utilized a femtosecond IR pulse that is broad in the frequency domain and a picosecond visible pulse that is narrow in frequency. This configuration allows for broadband sum frequency generation, whereby multiple SF frequencies can be simultaneously generated and detected.[234-235]
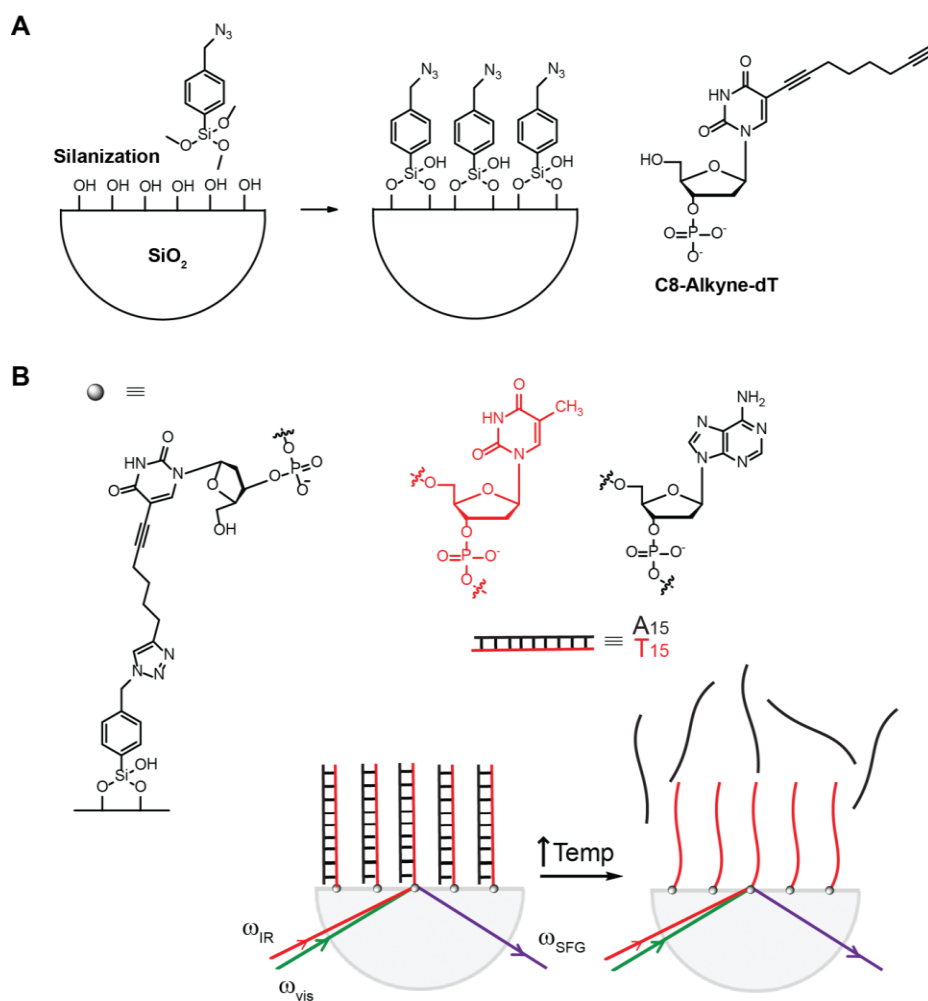
Figure 4.2 (A) The azide monolayer was prepared on silica hemisphere through silanization, and a DNA single strand 5'-dT-(T)$_{15}$-3' was synthesized, in which dT represents an alkyne modified thymidine. The DNA single strand was immobilized on the azide modified silica surface through copper(I) catalyzed azide-alkyne cycloaddition. (B) Schematic representation of monitoring the hybridization of immobilized DNA using vibrational sum frequency generation. The red line represents the T$_{15}$ single stand, and black line represents the complementary A$_{15}$ single strand.

As shown by the orientation dependence of $\chi_R^{(2)}$, one advantage of SFG is that it is very sensitive to the extent of ordering of the molecular oscillators in resonance with the incident IR, which in our experiments are the methylene and methine groups on the deoxyribose ring and the methyl groups on the thymine nucleobase.

4.3.2 Determination of the Surface Density of the Immobilized DNA Strand

The DNA surface was prepared using our previously published strategy[162] with a longer deposition time of *p*-azidomethylphenyltrimethoxysilane. X-ray photoelectron spectroscopy experiments indicated that the amount of surface nitrogen increased only slightly. Specifically, treating a Si wafer coated with a native oxide layer with the silane solution for 5 hours resulted in a N:O:Si ratio of 0.043:0.84:1. Increasing the reaction time for 15 hours resulted in a N:O:Si ratio of 0.052:0.81:1. The increase in the amount of nitrogen based on the increase in the N:Si or N:O ratio is indicative of a 20 or 25% increase, respectively, in azide compared with samples prepared in our previous publication.[162] For those samples a density of 6×10^{12} strand per cm^2 was estimated by assuming the silanol density was 3×10^{14} sites per cm^2 and that condensation with the *p*-azidomethylphenyltrimethoxysilane resulted in an azide density equal to 10% of the original silanol sites (this value represents an underestimation assuming far from complete condensation of all of the silanol sites). By using XPS, 15-30% of the azides were found to be converted to triazoles bearing DNA strands, which led to an approximate strand density of 6×10^{12} strands per cm^2. Although this density was calculated assuming the initial azide density, the resulting kinetic behavior was very consistent with a strand density of 10^{-7} mol per m^2 ($\sim 6 \times 10^{12}$ strand per cm^2) based on the kinetic model of heterogeneous hybridization put forth by Krull and co-workers.[236] Based on the slight increase in azide content under the coupling conditions for

101

this paper, a slightly higher strand density was expected, but according to the above model by Krull significant changes in the kinetic behavior are only expected when strand density varies by orders of magnitude.

4.3.3 SFG Spectra at the T$_{15}$-Functionalized Silica/Buffer Interface

We utilized the ssp polarization combination (s-SFG, s-vis and p-IR), commonly used to monitor the structure of DNA,[229-230] to probe these molecular resonances at the silica/buffer interface.

Unfortunately, utilizing D$_2$O to avoid spectral overlap between the O-H vibrational stretch of strongly hydrogen-bonded water (~3200 cm^{-1}) and that of the C-H groups in the DNA led to very poor spectra compared with that observed in water (Figure 4.3). When H$_2$O was used instead, much greater signal was observed, but the spectrum was broad indicative of resonant enhancement at all of the IR wavelengths present in the incident beam owing to the broad tail from the O-H vibrational stretch of water (Figure 4.4). However, upon adding NaCl, peaks emerged in the spectra that were clearly associated with the bound DNA. (Figure 4.4)

To understand the strong solvent dependence of the spectra, we reason that enhanced overlap between the O-H stretch of water and the C-H stretches actually improved the signal of the latter due to constructive interference that led to signal enhancement, which will be discussed later (Figure 4.5). We attribute the weaker SF signal in the D$_2$O spectra to two factors: first, the polarizability of OD is expected to be weaker than that of OH[237] and this polarizability contributes to the hyperpolarizability and thus SFG activity.[233] Second, the overlap is less between the C-H stretches and the weakly hydrogen-bonded O-D stretch (around 2510 cm^{-1})[238] compared with the overlap between the C-H stretches and the strongly hydrogen-bonded O-H

stretch (around 3200 cm^{-1}).[156] As the O-D peak is further from the C-H stretching region than the O-H peak, there is very weak resonance of D$_2$O in the C-H stretching region. As salt was added the amount of aligned D$_2$O diminished resulting in less resonant enhancement of the D$_2$O.
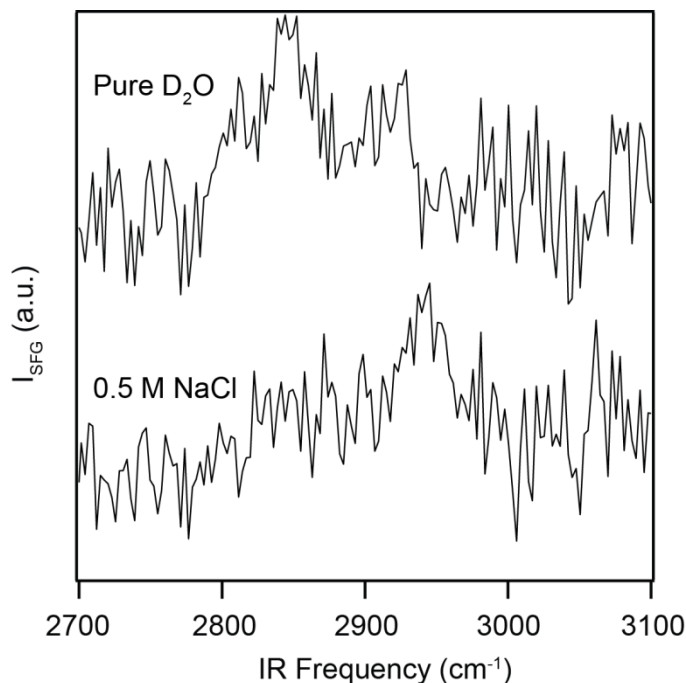
Figure 4.3 Raw (not normalized) SFG spectra at the T$_{15}$-functionalized silica/D$_2$O interface in pure D$_2$O and upon adding buffer (10 mM PBS, 0.5 M NaCl in D$_2$O, pH 7). The polarization combination was ssp.

As salt was added to the solution, the contribution to the $\chi_R^{(2)}$ from the H$_2$O decreased as the presence of NaCl is known to disrupt the structure of interfacial water.[239] The corresponding decrease in the amount of aligned water allowed us to discern the contribution to $\chi_R^{(2)}$ from the immobilized DNA (Figure 4.4). Consequently, we utilized buffered H$_2$O in these experiments and added 0.5 M NaCl to suppress the contribution of the water to the signal (the presence of salt is also necessary for duplex formation). In addition to decreasing the contribution from water,

with increasing salt concentration a decrease in the overall intensity of the C-H modes was consistently observed as shown in Figure 4.4. This decrease in C-H signal intensity indicated that increasing salt decreased the orientational average or reoriented the T_{15} strands resulting in lower SFG.
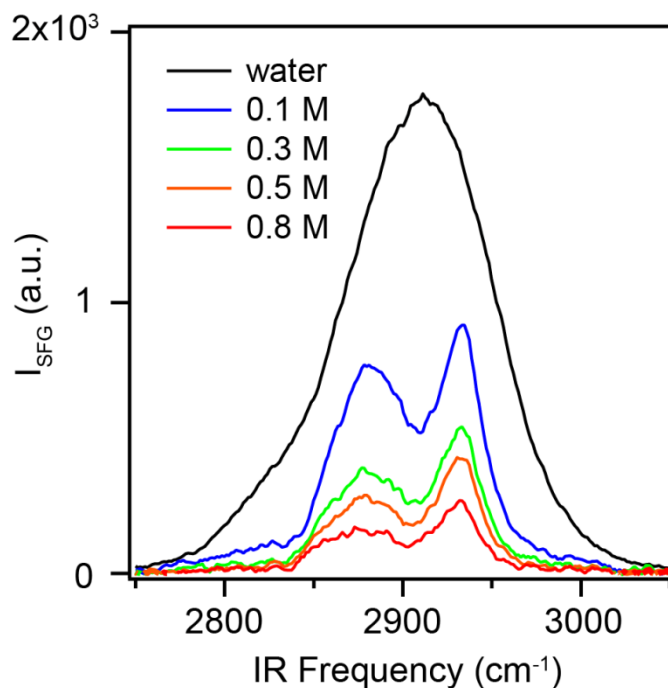
Figure 4.4 Raw (not referenced) SFG spectra from the T_{15}-functionalized silica/aqueous interface at varying NaCl concentrations. The Gaussian shape of the spectrum without salt is indicative of the incident femtosecond IR pulse that is broad in the frequency domain. The polarization combination was ssp.

Finally, as the spectrum in the absence of salt was featureless and representative of the broadband IR pulse, to account for the IR power profile we normalized our spectra by dividing each DNA/buffer spectrum by the spectrum measured at the pure water interface prior to the addition of NaCl containing buffer. After normalization, a higher baseline level was usually observed at high wavenumber (Figure 4.6), which we attribute to greater overlap with the O-H

resonance from water.

4.3.4 Interference between the C-H Stretch and O-H Stretch

In order to show how the interference between water's O-H stretch (3200 cm^{-1}, corresponding to strongly hydrogen bonded water) and the C-H stretches of DNA should affect the observed SFG spectra in the C-H stretch region, the following simple simulation was done. In this example, the amplitude of the CH$_3$ symmetric stretch peak at 2877 cm^{-1} was set as a constant while the amplitude of the O-H peak at 3200 cm^{-1} was varied. For simplicity the nonresonant second order susceptibility was set to zero. For the C-H and O-H resonances, the following peak properties were assumed: for the CH$_3$ symmetric stretch, $\omega = 2877$ cm^{-1}, $\Gamma = 16$ cm^{-1}, A = 1; for the OH stretch, $\omega = 3200$ cm^{-1}, $\Gamma = 150$ cm^{-1}.

$$
\begin{aligned}
\left|\chi^{(2)}\right|^2 &= \left|\chi^{(2)}_{CH} + \chi^{(2)}_{OH}\right|^2 = \left(\frac{1}{\omega - 2877 + 16i} + \frac{A}{\omega - 3200 + 150i}\right)\left(\frac{1}{\omega - 2877 - 16i} + \frac{A}{\omega - 3200 - 150i}\right) \\
&= \frac{1}{(\omega - 2877)^2 + 256} + \frac{A^2}{(\omega - 3200)^2 + 22500} + \frac{2A[\omega^2 - 6077\omega + 9208800]}{[(\omega - 2877)^2 + 256][(\omega - 3200)^2 + 22500]} \\
&= \text{term 1} + \text{term 2} + \text{term 3}
\end{aligned}
$$

(4.5)

In this equation, term 1 corresponds to the C-H stretching peak, term 2 corresponds to the O-H stretching peak, and term 3 is a cross term. Using a Gaussian expression for the IR intensity owing to the Gaussian shape of the IR pulse centered at 2900 cm^{-1} (bandwidth 120 cm^{-1}) and the three terms corresponding to $\left|\chi^{(2)}\right|^2$, SFG spectra were generated from:

$$
I_{SFG} \propto \left|\chi^{(2)}\right|^2 I_{vis} I_{IR} \propto \left|\chi^{(2)}\right|^2 I_{IR} = \left|\chi^{(2)}\right|^2 \exp\left[-\frac{(\omega - 2900)^2}{14400}\right]
$$

(4.6)
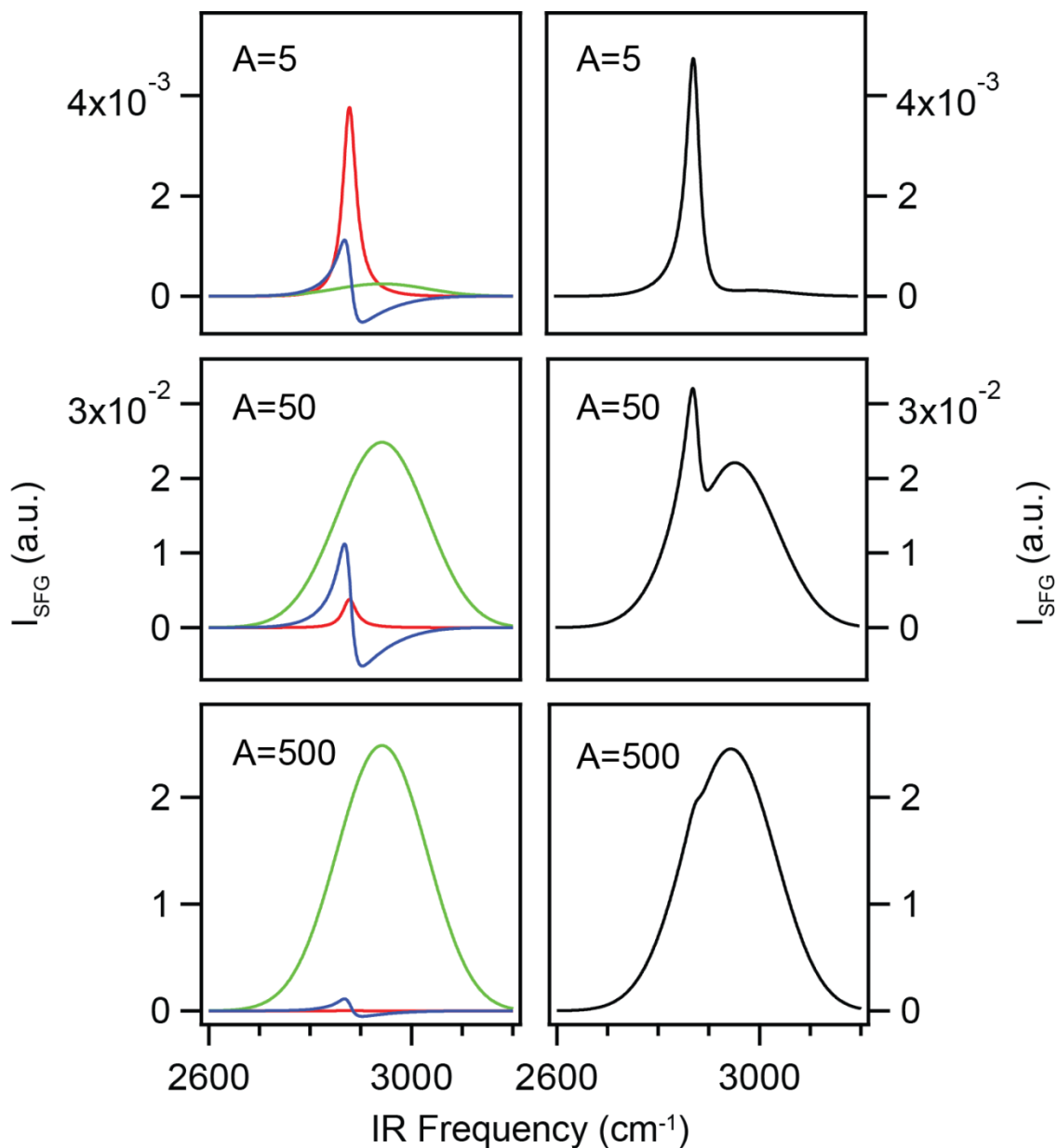
Figure 4.5 Simulated SFG spectra showing the interference between the water O-H stretch and a methyl C-H stretch. The spectra were modeled using equation 4.6. The amplitude of O-H peak (A) was varied and relative SFG intensities of the three terms were shown. The contribution to the signal of term 1 is shown in red, term 2 in green, and term 3 in blue. The overall observed spectra are in black on the right hand side.

Figure 4.5 shows the calculated relative intensities of the three terms and corresponding SFG spectra at different O-H peak amplitudes. When the amplitude of the O-H peak was much greater than that of the C-H stretch peak, the observed overall SFG spectra was dominated by the O-H peak and the C-H peaks were difficult to distinguish. As the amplitude of the O-H peak decreased, the C-H peaks became apparent. We propose these simulations explain the spectrum for the DNA-modified silica/pure water interface observed at very low salt concentration, which corresponds to a large amount of ordered water molecules owing to the presence of many negative charges at the interface. As salt was added, the interfacial static electric field arising from the negatively charged DNA and silica was screened resulting in less ordered water and a lower amplitude for the O-H peak (as the amplitude is proportional to the number density of aligned water).[239] In contrast, adding salt did not severely impact the amplitude of the C-H resonances as the number density of DNA remained constant. Consequently, the C-H resonances became apparent with increasing salt concentration.

4.3.5 Hybridization of the Immobilized T_{15} Strand with the Solution-Phase A_{15} Strand

Figure 4.6 illustrates the spectrum of the T_{15} immobilized at the silica/buffer interface in the presence of 0.5 M NaCl (10 mM phosphate buffer saline (PBS), pH 7) before and after hybridization with its complementary sequence. Using equations 4.1, we fit each spectrum to determine the peak amplitudes and central wavenumbers (table 4.1). Both before and after hybridization, the spectra exhibited five main transitions centered at 2856 cm^{-1}, 2878 cm^{-1}, 2895 cm^{-1}, 2924 cm^{-1} and 2936 cm^{-1}. We note that different samples led to different relative intensities of the five transitions, but the presence of all five transitions and the effect of hybridization and temperature on peak amplitude were consistent. We attribute this variability in relative amplitude

for different samples to variation in the average orientation of the immobilized DNA as the low strand density likely results in a variety of possible monolayer conformations unlike dense well-packed alkyl monolayers that yield highly reproducible structures and SFG spectra.
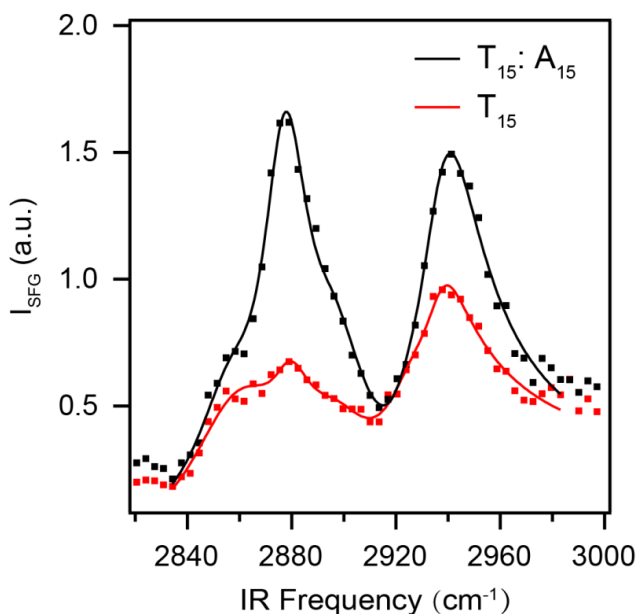
Figure 4.6 The SFG spectra collected at the T_{15}-functionalized silica/buffer interface before (T_{15}) and after ($T_{15}:A_{15}$) introduction of the complementary A_{15} strand. The spectra were normalized by the spectrum of the DNA-functionalized silica/water interface. The polarization combination was ssp.

Table 4.1 Spectral Fitting Parameters for Figure 4.6.

	ω	A^a	Γ	ω	A^a	Γ	ω	A^a	Γ	ω	A^a	Γ	ω	A^a	Γ
S^b	**2856**	17.1(1.9)	26.7	**2878**	1.5(1.1)	8.7	**2895**	1.7(1.6)	13.7	**2924**	6.2(2.6)	17.4	**2936**	1.9(0.7)	9.5
D^b	**2857**	7.8(2.8)	17.0	**2877**	9.9(1.2)	11.2	**2895**	5.8(2.8)	15.4	**2924**	2.3(2.3)	12.2	**2936**	9.7(2.1)	13.7

[a] The standard deviation of the amplitude returned from the fit is shown in parentheses.
[b] "S" represents single stand T_{15}, and "D" represents duplex $T_{15}:A_{15}$.

Regarding the peak assignments, we propose that these vibrational modes in the C-H stretching region originated primarily from the DNA as there were 15 methyl groups from the

nucleobases in addition to 32 methylene and 32 methine groups from the phosphate-sugar backbone for every four methylene groups from the alkyne linker (Figure 4.2). Moreover, we did not observe any appreciable signal for the benzyl azide monolayer in the presence of water (data not shown) and only very weak signal in the C-H region above 2850 cm^{-1} at the solid/air interface.[240]

4.3.6 SFG Spectra Peak Assignments

To aid in the assignment of the spectra, we reviewed the examples of IR absorbance and Raman spectroscopic measurements of the pure thymine nucleobase lacking the deoxyribose group in solution and the solid state.[241-245] Three to four peaks were generally observed between 2850 and 3000 cm^{-1} in both types of spectroscopy. The most consistently noted peak was a strong mode generally centered near 2940 cm^{-1} that we also observed, which has been attributed to the methyl symmetric stretch owing to its strong intensity in the Raman spectrum.[244-245] The presence of this mode at ~2940 cm^{-1} as well as lower wavenumber modes at 2908, 2880 and 2861 cm^{-1} was also observed in the SFG spectrum of pure thymine at the silica/air interface.[229] From these observations, we propose that the peak at 2936 cm^{-1} is primarily from the symmetric stretch of the methyl group on the thymine while the other three modes at ~2900, 2880 and 2860 cm^{-1} may stem from overtones associated with the thymine and possible contributions from C-H stretches of the sugar ring.[246] Additionally, the peak at 2924 cm^{-1} we attribute solely to methine or methylene stretches on the deoxyribose based on the SFG spectrum of thymidine at the silica/air interface,[229] as well as SFG measurements of A_{15} strands lacking methyl groups immobilized at the silica/air interface, which exhibited the strongest intensity at ~2924 cm^{-1} (Figure 4.7).
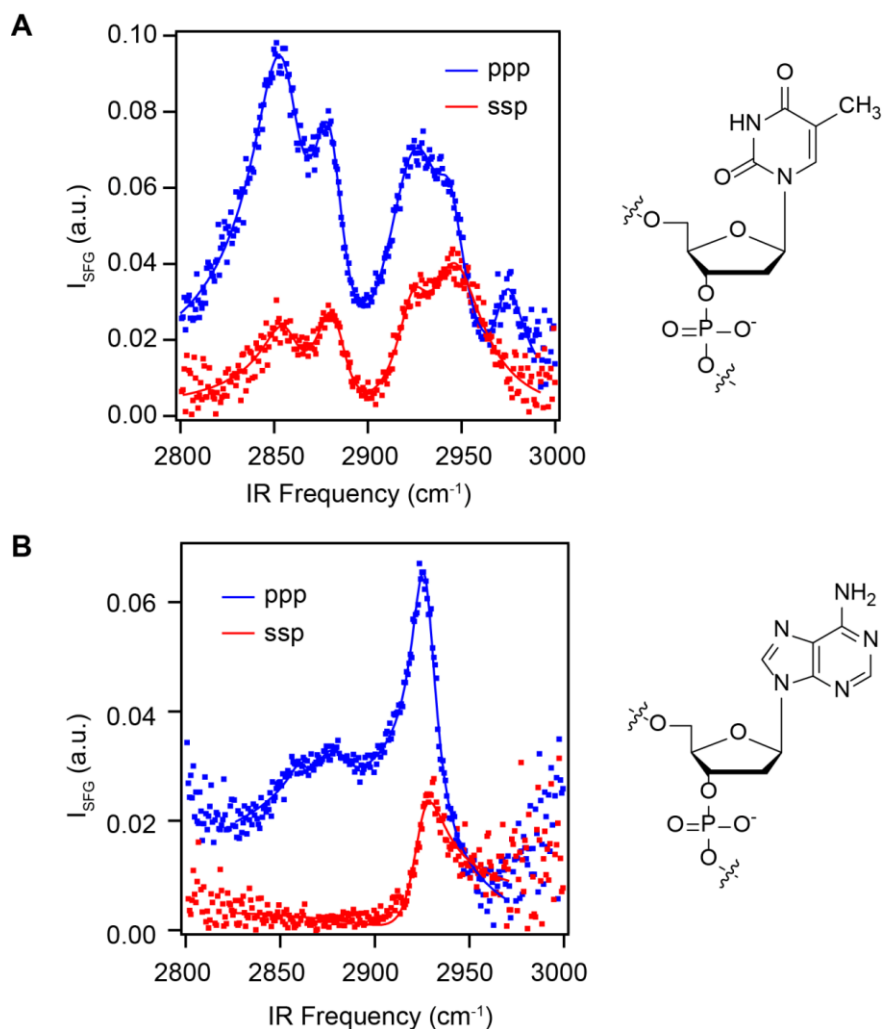
Figure 4.7 (A) The SFG spectra collected at the T_{15}-functionalized silica/air interface. The spectra were normalized by the spectrum from the silica/gold interface. (B) The SFG spectra collected at the A_{15}-functionalized silica/air interface. The spectra were normalized by the spectrum from the silica/gold interface. Both ppp (in blue) and ssp (in red) spectra were collected.

Table 4.2 Spectral Fitting Parameters for Figure 4.7A.

	ω	A^a	Γ	ω	A^a	Γ	ω	A^a	Γ	ω	A^a	Γ	ω	A^a	Γ
PPP	2857	2.8(0.2)	15.6	2881	1.9(0.1)	11.4	2926	4.9(0.4)	21.7	2943	0.6(0.2)	8.9	2973	0.9(0.1)	9.6
SSP	2857	1.1(0.2)	12.7	2882	1.3(0.1)	10.6	2924	1.2(0.4)	11.5	2944	2.6(0.5)	16.7	-	-	-

^{a} The standard deviation of the amplitude returned from the fit is shown in parentheses.

110

Table 4.3 Spectral Fitting Parameters for Figure 4.7B.

	ω	A^a	Γ	ω	A^a	Γ	ω	A^a	Γ	ω	A^a	Γ	ω	A^a	Γ
PPP	**2862**	0.10(0.06)	6.6	**2881**	0.5(0.2)	14.4	**2923**	5.4(0.7)	44.6	**2927**	1.0(0.1)	8.0	-	-	-
SSP	-	-	-	-	-	-	**2924**	1.24(0.05)	10.2	-	-	-	-	-	-

[a] The standard deviation of the amplitude returned from the fit is shown in parentheses.

From fitting, we found that the largest effect of hybridization of the T_{15}:A_{15} duplex on the spectra were increases in the intensity (manifested in the A/Γ ratio) for the modes at 2878 cm^{-1}, 2895 cm^{-1}, and 2936 cm^{-1} (Figure 4.6). We attributed the general increase in intensity of those modes particularly associated with the thymine base at 2878 cm^{-1}, 2895 cm^{-1} and 2936 cm^{-1} with an increase in orientational ordering of thymine after hybridization. This increase in intensity at ~2880 and 2940 cm^{-1} upon hybridizing polythymidine was also observed by the Geiger group for T_{15} strands immobilized at the silica/air interface.[173, 229] However, they did not observe any peak at ~2880 cm^{-1} prior to hybridization. The absence of this mode in the solid/air spectrum of Geiger could indicate that the single-strand was less ordered at the air interface compared with the buffer interface. However, their system used attachment chemistry that resulted in strong signals below 2900 cm^{-1} attributed in part to the structure of the underlying undecyl amide monolayer, which could have made detection of the peak at 2878 cm^{-1} difficult to discern for the more disordered single strand.[229]

To determine how our attachment chemistry influenced the spectrum of single-stranded DNA at the functionalized DNA-silica/air interface, we monitored SFG under two different polarization combinations (Figure 4.7). For these benzyl-triazole linked strands, the peaks at ~2880 cm^{-1} and ~2940 cm^{-1} were clear at the silica/air interface indicating that the single strand

was still relatively ordered in the absence of buffer. Moreover in the ppp spectrum more sensitive to asymmetric modes a peak at 2973 cm^{-1} was also observed for the immobilized T$_{15}$ at the solid/air (Figure 4.7A), which we attribute to the CH$_3$ asymmetric stretch. The presence of this mode also associated with the methyl group on the thymine nucleobase provides further support that the methyl groups exhibit net orientation even for single-stranded samples at the silica/air interface.

4.3.7 Melting of T$_{15}$:A$_{15}$ Duplex at the Solid/Buffer Interface Monitored Using SFG

Many applications using immobilized DNA strands utilize thermal stringency washes to liberate any weakly adsorbed DNA from the surface and allow only the perfectly complementary strands to remain.[214] Additionally, the thermal dissociation of oligonucleotide duplexes is often monitored in solution[247] and on surfaces[162, 248] to quantify the stability of a duplex and gain information about the thermodynamic parameters associated with hybridization. Little is known, however, about the structural changes of immobilized DNA as a function of temperature, particularly at the silica/buffer interface.

Consequently, we monitored SFG as the temperature increased from 20 to 60 °C (Figure 4.8A). We found, the SFG signal decreased with increasing temperature (Figure 4.8A). However, upon fitting the data it was revealed that the most sensitive peak to temperature was that at 2937 cm^{-1} for the duplex system. The amplitude-line width ratio (A/Γ) proportional to $\chi_R^{(2)}$[249] is shown for the peak at 2937 cm^{-1} as a function of temperature (Figure 4.8B). We attribute the decrease in intensity of the peak at 2937 cm^{-1} between 20 and 60 °C to dissociation of the duplex.
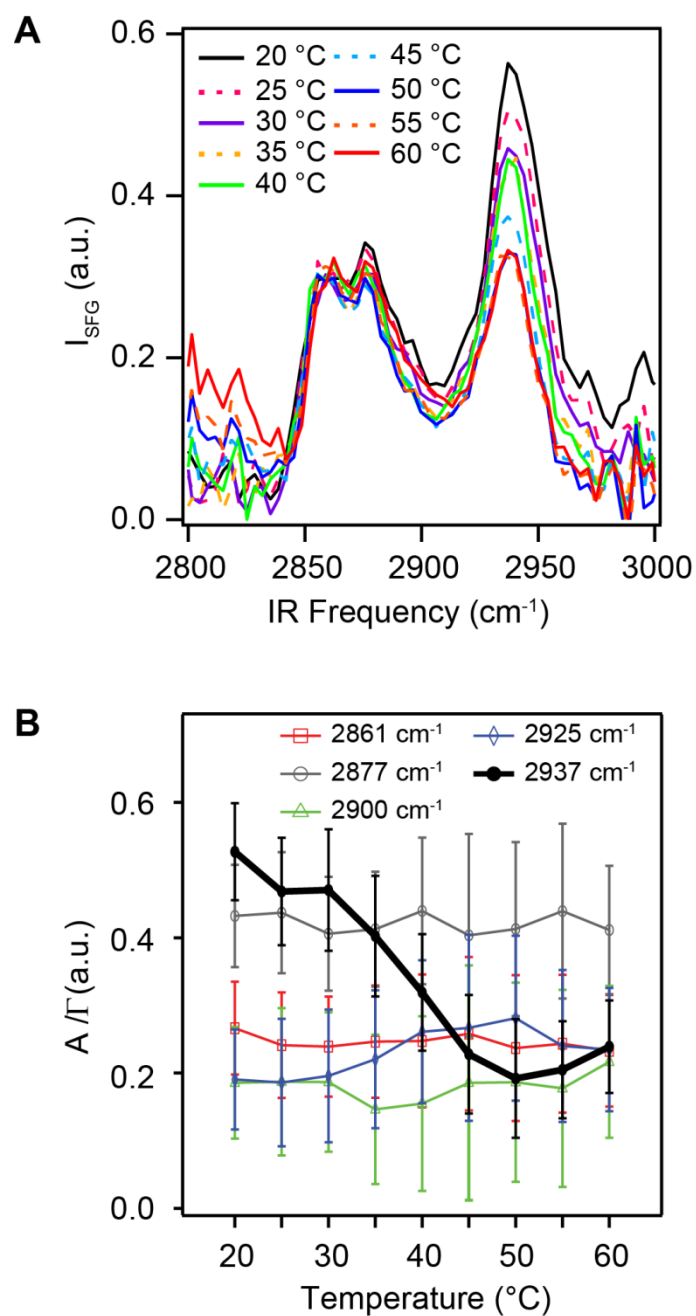
Figure 4.8 (A) Changes in SFG intensity of the $T_{15}:A_{15}$ modified surface as a function of temperature. The spectra collected at the DNA-functionalized silica/buffer interface were normalized by the spectrum from the same sample at the pure water interface. The polarization combination was ssp. (B) The amplitude and line-width ratio (A/Γ) corresponding to the five modes for the duplex system plotted versus temperature.

4.3.8 Melting of $T_{15}:A_{15}$ Duplex in Solution Phase Monitored Using UV-Vis Spectroscopy

The melting of the same DNA duplex in solution phase was monitored using UV-visible spectroscopy under the same reaction conditions. The temperature of the solution was increased from 20 to 70 °C, and the UV absorbance of the solution at 260 nm was recorded as a function of temperature. Because of the hyperchromic effect, DNA single strands absorb more light at 260 nm than DNA duplexes making absorbance measurements the standard method for monitoring DNA melting in solution.
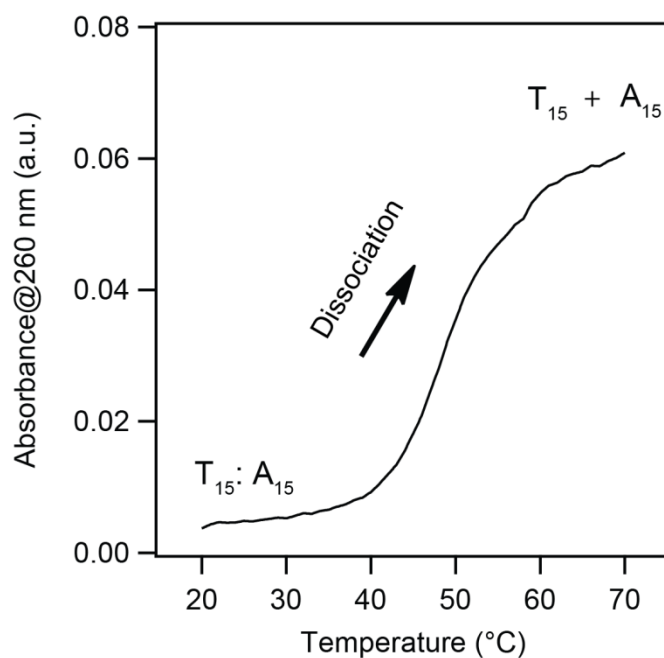
Figure 4.9 $T_{15}:A_{15}$ duplex melting monitored using UV-vis spectroscopy. *Reaction conditions:* 0.61 μM of each solution phase strand, 0.5 M NaCl, 10 mM PBS buffer, pH 7.0.

At room temperature, two complementary DNA single strands exist as duplex; as the temperature of the solution increases, the percentage of DNA duplex starts to decrease, and the UV absorption at 260 nm keeps increasing. The UV absorption reaches at maximum when the percentage of DNA single strand reaches at maximum (~ 100%) at high temperature. Figure 4.9

114

shows a typical melting profile of a DNA duplex in solution monitored using UV-visible spectroscopy, and the melting temperature of duplex (T_m) is defined as the temperature at which half of the DNA strands are in single strand state.

4.3.9 Comparison of Thermal Dissociation Profiles of the Immobilized and Solution-Phase T_{15}:A_{15} Duplex

Our previous study utilizing second harmonic generation spectroscopy and the same copper-catalyzed azide-alkyne cycloaddition attachment strategy found that immobilization of a 15-mer onto silica suppressed the thermal dissociation, or melting, temperature (T_m) by approximately 12 ± 2 °C in comparison with its solution-phase melting temperature (Figure 4.10A).[162] To verify that the change in A/Γ (2937 cm^{-1}) SFG ratio versus temperature for the duplex system stemmed from duplex dissociation, we compared it under the same conditions (0.61 μM primer, 0.5 M NaCl, 10 mM PBS buffer, pH 7.0) to the thermal dissociation of solution-phase DNA based on changes in UV absorbance at 260 nm (Figure 4.10B).

To determine the melting temperature from the SFG experiments, the A/Γ ratio at 2937 cm^{-1} (*Ratio*) versus temperature in Figure 4.10B was fit with the following equation:

$$\frac{Ratio_{\max} - Ratio}{Ratio_{\max} - Ratio_{\min}} = \text{Fraction Dissociated} = \frac{1}{1 + \exp\left(\dfrac{\Delta H}{R}\left(\dfrac{1}{T + 273.15} - \dfrac{1}{T_m + 273.15}\right)\right)}$$

(4.7)

where ΔH is the dissociation enthalpy, T is the temperature of the solution phase in Celsius, T_m is the melting temperature in Celsius, R is the ideal gas constant, $Ratio_{\max}$ and $Ratio_{\min}$ are fitting parameters.[162]
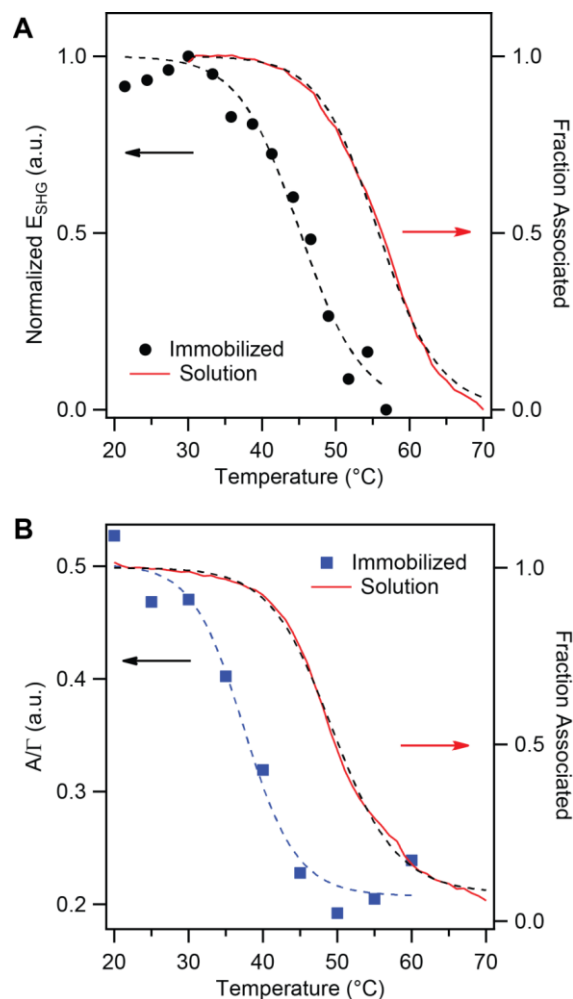
Figure 4.10 (A) Thermal dissociation of a 15 base pair DNA duplex at the silica/water interface monitored by resonant SHG and the comparison with the corresponding melting curve in solution phase using the same immobilization chemistry. The melting temperature difference was determined to be approximately 12 ± 2 °C. The figure is re-created from reference.[162] (B) Comparison of the melting curve of the immobilized $T_{15}:A_{15}$ duplex from the SFG A/Γ ratio (blue) and the free duplex in solution (red) based on absorbance measurements. *Reaction conditions:* 0.61 μM of each solution phase strand, 0.5 M NaCl, 10 mM PBS buffer, pH 7.0. The melting temperature difference was determined to be 11.9 °C very consistent with the results from the SHG study. The dashed lines are fits to the data with equation 4.7 and 4.8.

For the DNA duplex melting in the solution phase, the absorbance at 260 nm (Abs) was

converted to the fraction dissociated according to:

$$1 - \frac{Abs_{\max} - Abs}{Abs_{\max} - Abs_{\min}} = \text{Fraction Dissociated} = \frac{1}{1 + \exp\left(\dfrac{\varDelta H}{R} \left(\dfrac{1}{T + 273.15} - \dfrac{1}{T_m + 273.15} \right) \right)}$$

$$(4.8)$$

where $\varDelta H$ is the dissociation enthalpy, T is the temperature of the solution phase in Celsius, T_m is the melting temperature in Celsius, R is the ideal gas constant, $Abs_{\max}$ and $Abs_{\min}$ are fitting parameters.

From the fit to the SFG and absorbance data, the T_m was determined to be 37.5 °C for the former (the immobilized duplex) and 49.4 °C for the latter (the solution-phase duplex). The difference between the solution-phase melting temperature and the melting temperature for the immobilized DNA duplex was therefore 11.9 °C, which is consistent with our previous study (12 ± 2 °C). This difference in dissociation temperature between the solution-phase measurements and the SFG data was in excellent agreement with the suppression in T_m found in our SHG work (12 ± 2 °C) providing strong evidence that the major change in A/Γ ratio at 2937 cm^{-1} with temperature was due to duplex dissociation.

4.3.10 Thermal Evolution of Single-Stranded Immobilized DNA

Figure 4.11A shows the thermal evolution of the single-stranded oligonucleotide T_{15} immobilized at the silica/buffer interface. The thermal behavior of the immobilized single strand is not as predictable. Overall the SFG signal gradually decreased from 20 to 60 °C, indicating thermal energy induced randomization of the strand conformation owing to increased conformation entropy at higher temperatures.
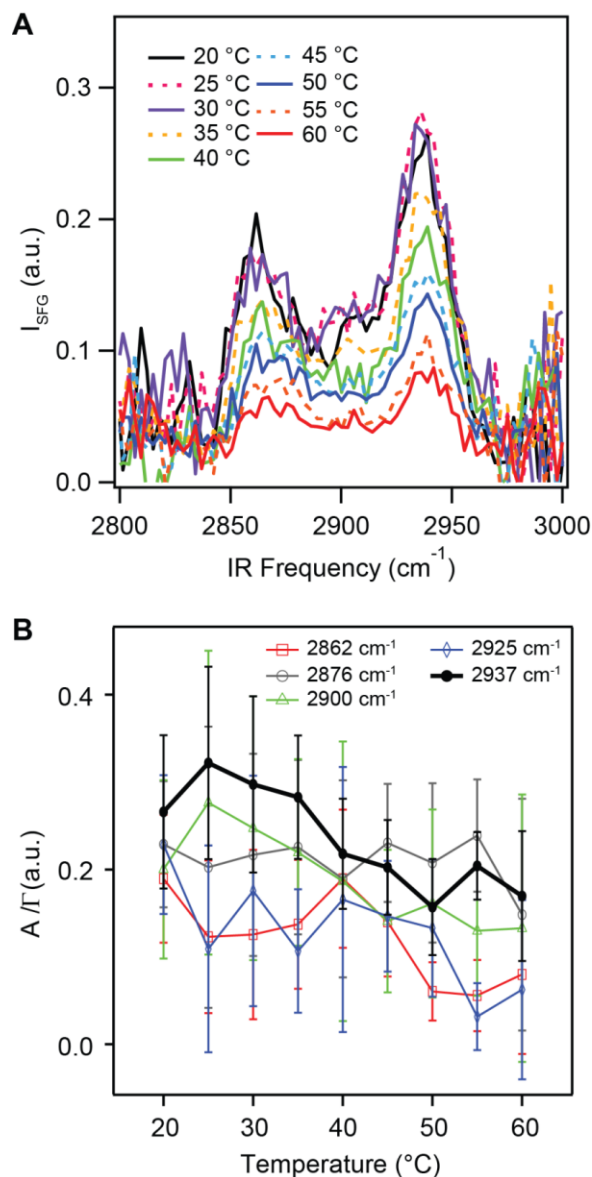
Figure 4.11 (A) Changes in SFG intensity of the T_{15}-modified silica/buffer interface normalized to that of water as a function of temperature. The spectra collected at the DNA-functionalized silica/buffer interface were normalized by the spectrum from the same sample at the pure water interface. The polarization combination was ssp. (B) The amplitude and line-width ratio (A/Γ) corresponding to the five modes for the single strand system plotted versus temperature.

After fitting, the A/Γ ratios for the five modes were plotted versus temperature (Figure 4.11B). We observed a small decrease in the A/Γ ratio at 2937 cm^{-1} between 35-45 °C, but this change was within uncertainty. We also note that the uncertainty in amplitude was larger for the

single-stranded sample than the duplex, which makes evaluating the temperature behavior of the latter more difficult.

4.3.11 Annealing of the T_{15} and T_{15}:A_{15} Functionalized Samples

To see whether the effect of temperature was reversible for both the single stranded and immobilized duplex samples the SFG spectra were measured for two samples before and after heating. In these experiments, the temperature of the samples was gradually increased to 60 °C followed by a gradual decrease to lab temperature (~21 °C). The T_{15}:A_{15} sample was then allowed to rehybridize for one hour.
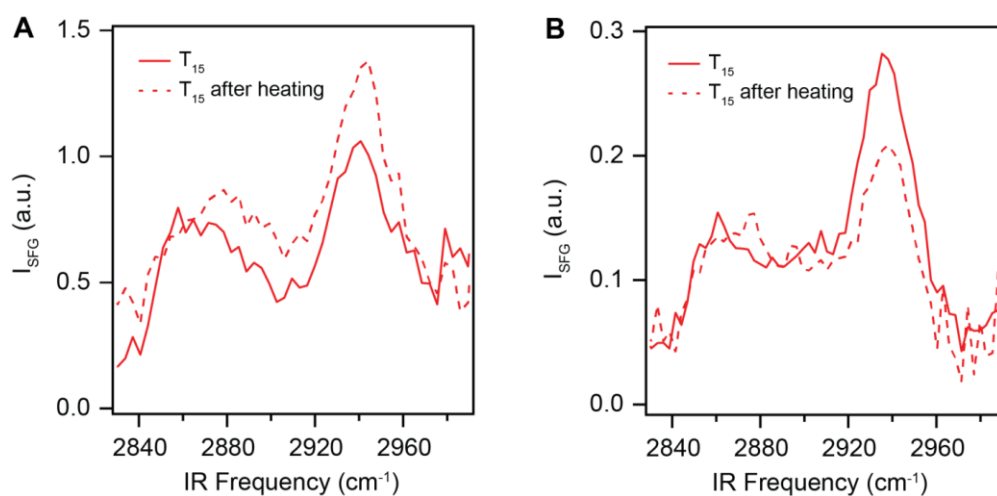
Figure 4.12 SFG spectra collected from the single-stranded T_{15}-functionalized silica/buffer interface before and after annealing the sample at 60 °C. The spectra were collected under the ssp polarization combination, and normalized to that from the DNA-functionalized silica/water interface. (A) and (B) represented spectra collected from two different samples under the same reaction conditions.
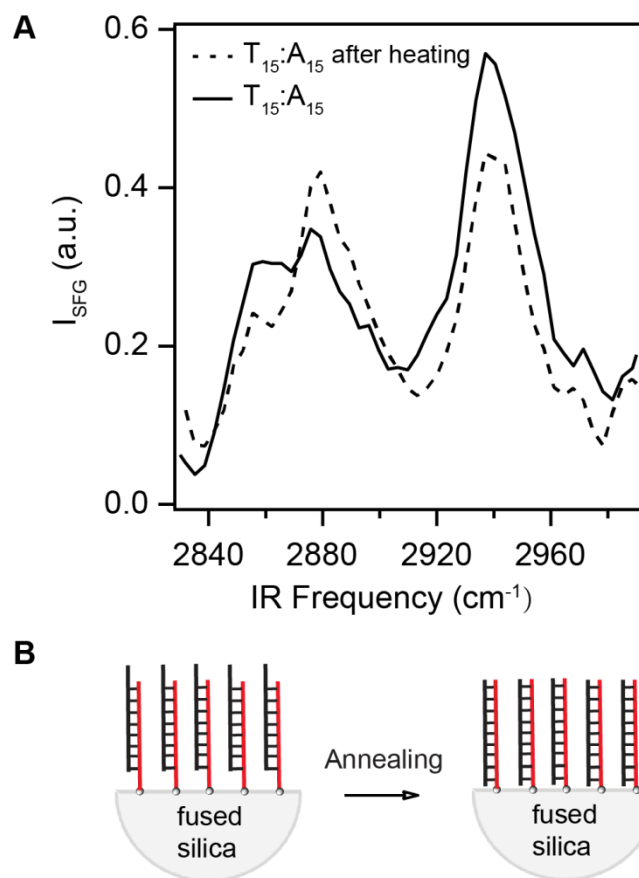
Figure 4.13 (A) SFG spectra before and after annealing the sample at 60 °C for the immobilized $T_{15}:A_{15}$ duplex. The spectra were collected at the DNA-functionalized silica/buffer interface and normalized by that from the DNA-functionalized silica/water interface. The polarization combination was ssp. (B) Schematic diagram explaining the spectral changes with annealing. Incomplete formation of the $T_{15}:A_{15}$ duplex was formed upon hybridizing the sample at the lab temperature, and this duplex was able to rearrange to the more stable duplex upon heating and cooling.

Table 4.4. Spectral Fitting Parameters for Figure 4.13A.

	ω	A^a	Γ	ω	A^a	Γ	ω	A^a	Γ	ω	A^a	Γ	ω	A^a	Γ
I^b	2860	2.2(0.6)	8.2	2877	5.9(1.0)	13.8	2895	2.3(1.0)	12.5	2917	2.6(1.0)	13.5	2935	6.2(0.8)	11.7
II^b	2859	1.1(0.3)	6.9	2879	4.3(0.6)	11.5	2894	6.1(1.6)	19.2	2928	2.9(1.3)	14.9	2938	3.9(0.6)	10.3

a The standard deviation of the amplitude returned from the fit is shown in parentheses.
b "I" represents "before annealing", and "II" represents "after annealing".

For both the duplex and single-strand functionalized samples, differences were observed before and after heating indicating that annealing played a major role in the structure of the immobilized strands. The changes in spectra for the single strand varied from sample to sample (Figure 4.12), whereas the spectral changes for the duplex were very consistent (Figure 4.13A). Specifically, spectra fitting revealed that annealing led to an increase in the mode at ~2895 cm^{-1}, which we associate with the thymine nucleobase as well as contributions from the deoxyribose ring.[246] In contrast, the modes at 2937 cm^{-1} and 2860 cm^{-1} also observed in the thymine spectra decreased. We attribute the spectral changes with annealing to the incomplete formation of the T_{15}:A_{15} duplex upon hybridizing the sample at the lab temperature. We propose that a shorter duplex formed more rapidly at the interface, and this duplex was only able to rearrange to the more stable duplex upon heating and cooling (Figure 4.13B). This led to different changes in peak intensity, likely due to a change in net orientation of the tethered duplex upon annealing. To avoid the formation of shorter duplexes future work will focus on non-repeating sequences that facilitate only one hybridization conformation.

4.4 Conclusion

In conclusion, we have demonstrated that the temperature sensitivity of immobilized DNA duplexes can be observed by SFG at the silica/buffer interface. Despite the expected disorder of the single unhybridized strand, all three major peaks that we attribute to the thymine nucleobase were present indicating that there was considerable net order of the single strands in the presence of buffer or air. We also observed that the temperature-sensitivity of the immobilized duplex was consistent with our previous work using labeled DNA that revealed that immobilization on silica was destabilizing leading to a lower dissociation temperature. The most temperature-sensitive

mode was attributed to the methyl groups on the polythymidine immobilized on silica, which should experience significant reorientation upon duplex dissociation. Annealing both the single strand and duplex immobilized samples led to changes in the SFG spectra, which may have ramifications for optimizing the hybridization efficiency and rate in DNA chip-based diagnostics. Future work will examine the influence of strand density and pH on strand orientation and temperature sensitivity.

Chapter 5

The Organization of Acetonitrile at the Fused Silica/Water

Interface Studied by Sum Frequency Generation

5.1 Introduction

At interfaces, liquid molecules usually exhibit properties that are different from their properties in bulk solution.[16] These properties have a significant impact on processes that occur at interfaces, such as heterogeneous catalysis, surface modification and fabrication, and absorption/desorption. Studying the properties of interfacial liquid molecules, and the interaction between liquid molecules and neighboring solid surface, will benefit the understanding of these interfacial processes.

Acetonitrile has a large dielectric constant, which is one of the most widely used solvents in chemistry. The acetonitrile molecule contains a hydrophobic methyl group and a highly polar cyanide group; this unique hydrophobic/polar combination makes acetonitrile have the capacity to dissolve a wide range of organic compounds.[142, 250] Acetonitrile is also miscible in water at any ratio, and consequently the acetonitrile/water mixture is a commonly used mobile phase in chromatography and is found to be effective in the separation of many chemical and biological species.[251-258]

Previous studies suggested that acetonitrile molecules form lipid-bilayer-like structures at the silica surface.[142, 250, 259-265] The formation of this bilayer structure is believed to be induced by hydrogen bond formation between the cyanide group and surface silanols. At the silica surface, the first sublayer has the most ordered structure, in which the cyanide groups point toward the silica surface due to the formation of these hydrogen bonds while the methyl groups point toward bulk solution; the second sublayer is less ordered than the first one, in which methyl groups interdigitate with methyl groups from the first sublayer and point towards the silica surface.[142] This bilayer pattern keeps repeating and becomes less and less ordered with distance.[142] A recent study suggested that the bilayer structure exists not only at the silica/acetonitrile interface, but

also at the silica/acetonitrile:water mixture interface, even at very low acetonitrile concentrations.[250] At both interfaces, two types of acetonitrile molecules are present within the bilayer pattern with different hydrogen-bonded states and chemical environments, based on their distinguishable resonances in the SFG spectra with central wavenumbers differing by as much as 10 cm^{-1}.[142, 250]
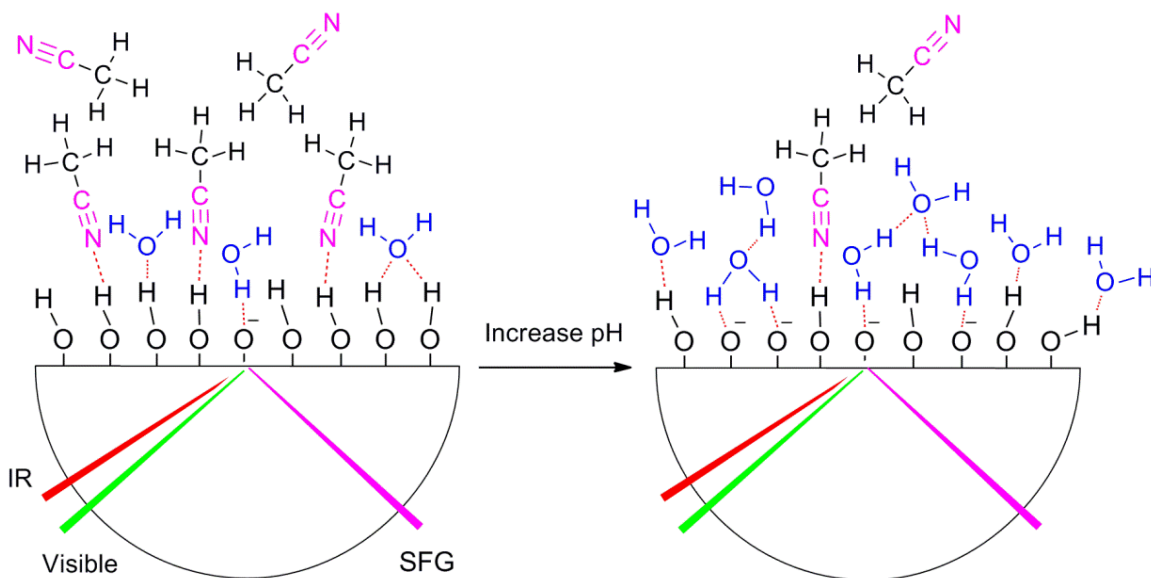
Figure 5.1 The organization of acetonitrile at the fused silica/water interface studied by vibrational sum frequency generation spectroscopy.

Knowing the importance of acetonitrile and the wide application of acetonitrile/water mixtures in heterogeneous catalysis and chromatography, it is worthwhile to study the properties of the acetonitrile molecule at the silica surface in the presence of water, especially at various solution pH values. In this chapter, vibrational sum frequency generation (SFG) spectroscopy was employed to study the interfacial structure and orientation of acetonitrile at the silica surface in the presence of water (Figure 5.1). The fitting of the methyl symmetric stretch mode using different models has been discussed, and as will be shown a single-Lorentzian model is found to

provide reasonable fit of the spectrum. Orientation analysis revealed that the net orientation of the acetonitrile molecule did not change significantly as the mole fraction of acetonitrile decreased from 100% to 4% in the acetonitrile/water mixture. At a certain acetonitrile/water composition, increasing the solution pH which deprotonated more surface silanol groups resulted in a decreased number of ordered interfacial acetonitrile molecules.

5.2 Experimental Section

5.2.1 Laser System and Experimental Setup

Our broadband SFG setup has been described in detail in Chapters 2 and 3. Generally, the amplified 798-nm light from the Spitfire was passed through a 30/70 beam splitter, and 2.3 W of the output was used to pump a non-collinear optical parametric amplifier (TOPAS-C and NDFG, Light Conversion) to generate IR light, while some of the remaining 798-nm light passed through a Fabry-Perot etalon (TecOptics) to generate picosecond pulses (full width half maximum of 10 cm^{-1}). Each beam was focused at the sample using a CaF$_2$ (focal length = 500 mm, Thorlab) or BK7 (focal length = 400 mm, Thorlab) focusing lens, respectively. Pulse energies of 10-20 μJ/pulse of visible and ~25 μJ/pulse of IR were used, and the beams were slightly defocused to minimize sample damage. The infrared and visible pulses were directed through the IR grade silica hemisphere at incident angles of 67° and 65° with respect to surface normal. The sample cell was designed to place the flat surface of the hemisphere perpendicular to the laser table.

For all of the experiments present in this chapter, only one TOPAS-NDFG setting was used to collect the spectra centered near 2950 cm^{-1}. The data were acquired for 1 min per spectrum.

The spectra shown in the figures are representative of at least two experiments. The error in A/Γ and ω_v represents the standard deviation from fit for a single set of spectra.

5.2.2 Materials and Sample Preparation

HPLC grade acetonitrile (> 99.9%) was purchased from Fisher Chemical and used without further purification. Ultrapure deionized (18.2 MΩ•cm) water was used shortly after deionization by a Milli-Q Plus ultrapure water purification system (Millipore).

Prior to each experiment, an IR grade silica hemisphere was cleaned with water and methanol, followed by drying in an oven for 10 min at 90 °C. The cleaned hemisphere was treated with fresh "piranha solution" (3:1 mixture of sulfuric acid and 30% hydrogen peroxide) for 1h. It was then rinsed copiously with Millipore water, and methanol. Afterwards, the hemisphere was placed in an oven for 30 min at 90 °C, followed by cooling to room temperature and then plasma cleaning (plasma cleaner, PDC-32G, Harrick Plasma) in air for 2 min. The cleaned hemisphere was used right after plasma cleaning.

5.2.3 Spectral Normalization and Fitting

The spectra shown in this chapter were normalized to the spectra from silica/gold interface, as gold exhibits strong non-resonant signal independent of IR wavelength. To achieve this, after background subtraction, the spectrum from the sample interface was divided with the spectrum measured immediately before from a gold-coated silica hemisphere at the same IR central wavelength (the same TOPAS-NDFG settings).

Equation 5.1 was employed to fit the normalized SFG spectra. In this equation, the second order susceptibility $\chi^{(2)}$ is broken down into two terms: a non-resonant term, $\chi^{(2)}_{NR}$, and

vibrational resonant term $\chi_R^{(2)}$ summed over all possible frequencies. Each resonant mode is considered to possess a Lorentzian lineshape.[81-82, 84]

$$I_{SFG} \propto \left|\chi^{(2)}\right|^2 = \left|\chi_{NR}^{(2)} + \sum_{v}\chi_R^{(2)}\right|^2 = \left|\chi_{NR}^{(2)} + \sum_{v}\frac{A_v}{\omega_{IR} - \omega_v + i\Gamma_v}\right|^2 \qquad (5.1)$$

Here ω_{IR} is the frequency of the incident IR beam, and A_v, ω_v, and Γ_v are the amplitude, central frequency, and damping coefficient of the vth surface vibrational mode, respectively.

The fitting was accomplished using Igor Pro: based on the number of vibrational modes expected in the region, a function with the desired number of resonant terms and a non-resonant term, which is a constant, was chosen for fitting. For each fitting, initial A_v, ω_v, Γ_v and $\chi_{NR}^{(2)}$ values were estimated and then the software was allowed to optimize all of them; the returned values from the previous run were used as initial values for a second run. The fitting stopped when the returned values were the same as the previous input values.

5.3 Results and Discussion

5.3.1 Theoretical Background of SFG

Sum frequency generation occurs when two incident fields are temporally and spatially overlapped in a noncentrosymmetric medium like an interface.[50, 54] New light is generated at a frequency that is the sum of the two incident frequencies. As shown in equation 5.2 and 5.3, the intensity of this sum frequency signal (I_{SFG}) is proportional to the incident visible (I_{vis}) and IR (I_{IR}) intensities and the second-order susceptibility ($\chi^{(2)}$), which is specific to each interface. The resonant part of the second-order susceptibility of the system, $\chi_R^{(2)}$, can be related to the

presence of ordering of specific molecules at the interface as $\chi_R^{(2)}$ is proportional to the product of the number density of molecular oscillators in resonance (N) and the orientationally averaged molecular hyperpolarizability ($\langle \beta_v^{(2)} \rangle$).[81, 233] Specifically, the SFG signal is resonantly enhanced when the IR frequency approaches the frequency of a surface vibrational mode that is both IR and Raman active.

$$I_{SFG} \propto \left| \chi^{(2)} \right|^2 I_{vis} I_{IR} = \left| \chi_{NR}^{(2)} + \sum_v \chi_{R_v}^{(2)} \right|^2 I_{vis} I_{IR} \tag{5.2}$$

$$\chi_{R_v}^{(2)} \propto N \langle \beta_v^{(2)} \rangle \tag{5.3}$$

5.3.2 SFG Spectra of Acetonitrile at the Silica/Acetonitrile Interface

SFG spectra of acetonitrile in the C-H stretch region were collected from the silica/pure acetonitrile interface under both ppp and ssp polarization combinations. As shown in Figure 5.2, the spectra exhibited a strong peak at $\sim$ 2943 cm^{-1} under ppp polarization and at $\sim$ 2944 cm^{-1} under ssp polarization. This mode was attributed to the symmetric stretch of the methyl group consistent with previous studies.[142] In the ppp spectrum, a broad peak between 3000 and 3200 cm^{-1} was also observed and attributed to the asymmetric stretch of the methyl group,[250] which had a much weaker peak intensity and was absent in ssp spectrum (Figure 5.2A). When the pure acetonitrile was replaced with an acetonitrile/water mixture (mole fraction of acetonitrile, n_{ACN} = 76%), the methyl symmetric stretch peak exhibited a weaker peak intensity, which mainly resulted from the decrease in the number density of acetonitrile molecules in the interface region; at the same time, the methyl asymmetric stretch peak was no longer observable (Figure 5.2B).
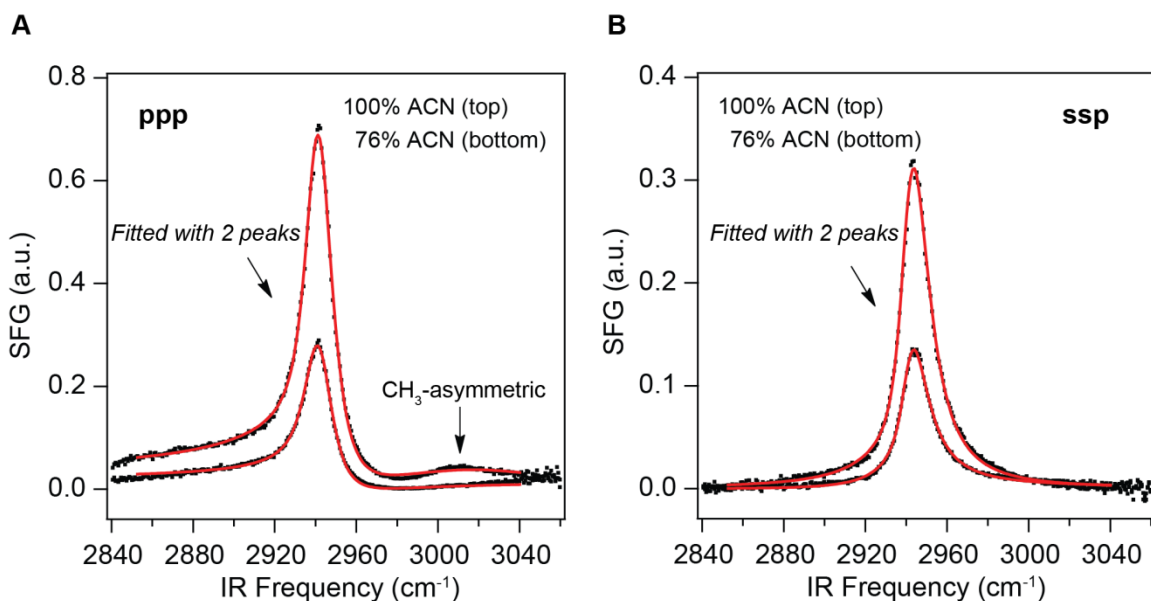
Figure 5.2 SFG spectra of acetonitrile in the C-H stretch region collected from silica/liquid interface under ppp (A) and ssp (B) polarization combinations. The mole fraction of acetonitrile was 100% and 76%, respectively. In the figure, the black dots are experimental data and the solid lines are theoretical fitting using equation 5.1. For all spectra, the methyl symmetric stretch peak was fit with a double-Lorentzian model, and the fitting parameters are reported in table 5.1.

Table 5.1 Fitting Parameters for Figure 5.2

	Peak 1			Peak 2		
	ω_v^{a}/cm^{-1}	A_v^{a}	Γ_v^{a}/cm^{-1}	ω_v^{a}/cm^{-1}	A_v^{a}	Γ_v^{a}/cm^{-1}
ppp -100% ACN	2940 ± 4	29 ± 136	11.6 ± 0.3	2941 ± 3	-34 ± 136	11.3 ± 0.9
ssp -100% ACN	2940 ± 4	31 ± 292	11 ± 1	2941 ± 4	-36 ± 292	11.1 ± 0.5
ppp - 76% ACN	2941 ± 6	31 ± 436	12 ± 3	2941 ± 5	-34 ± 436	11 ± 3
ssp - 76% ACN	2940 ± 2	30 ± 378	10 ± 1	2941 ± 2	-34 ± 378	9.8 ± 0.6

[a]In the notation 2940 ± 4, 2940 is the fitting parameter and 4 is the standard deviation from fitting.

Previous studies suggested that the acetonitrile molecule organizes into a lipid-bilayer-like structure at the silica/acetonitrile interface,[142, 250, 259-265] and this bilayer structure persists in the presence of water even at very low acetonitrile concentrations.[250] The investigation by Fourkas, Walker, Weeks and co-workers suggested that, for SFG spectra collected at the silica/acetonitrile

interface, fitting the peak corresponding to the methyl symmetric stretch revealed two types of methyl groups: one hydrogen bonded to surface silanol groups through the cyanide, and the other not. These modes were found to be distinguishable in the SFG spectra due to a 10 cm^{-1} difference in resonant wavenumber.[142]

As shown in Figure 5.2, in our first analysis we fit the methyl symmetric stretch mode with a double-Lorentzian model, and the fitting parameters are summarized in table 5.1. Unfortunately, the difference in the resonant wavenumber of the two peaks was found to be around 1 cm^{-1}, which lies within the resolution of SFG, and the peak amplitudes have huge uncertainties, indicating the double-Lorentzian model is not applicable here. Moreover, as will be shown a single-Lorentzian model provides a reasonable fit to our spectra. This difference in the fitting model is likely due to the different local chemical environments around interfacial acetonitrile molecules. Silica surface is highly sensitive to its chemical history,[266] so any difference in sample preparation stage (for example using different sample cleaning strategy), may make a difference in the final performance of silica surface. Although the bilayer structure of acetonitrile is still likely to exist, the methyl groups that are oriented in opposite direction have similar hydrogen-bonded environments, and consequently have a similar vibrational frequency in SFG spectra. Consequently, the SFG spectrum represents the net contribution of these two types of acetonitrile molecules as manifested in the orientationally averaged molecular hyperpolarizability. Based on these observations, a single-Lorentzian model was employed to fit the methyl symmetric stretch peak in the following experiments.

5.3.3 SFG Spectra of Acetonitrile from the Silica/Aqueous Interface at Various ACN Concentrations
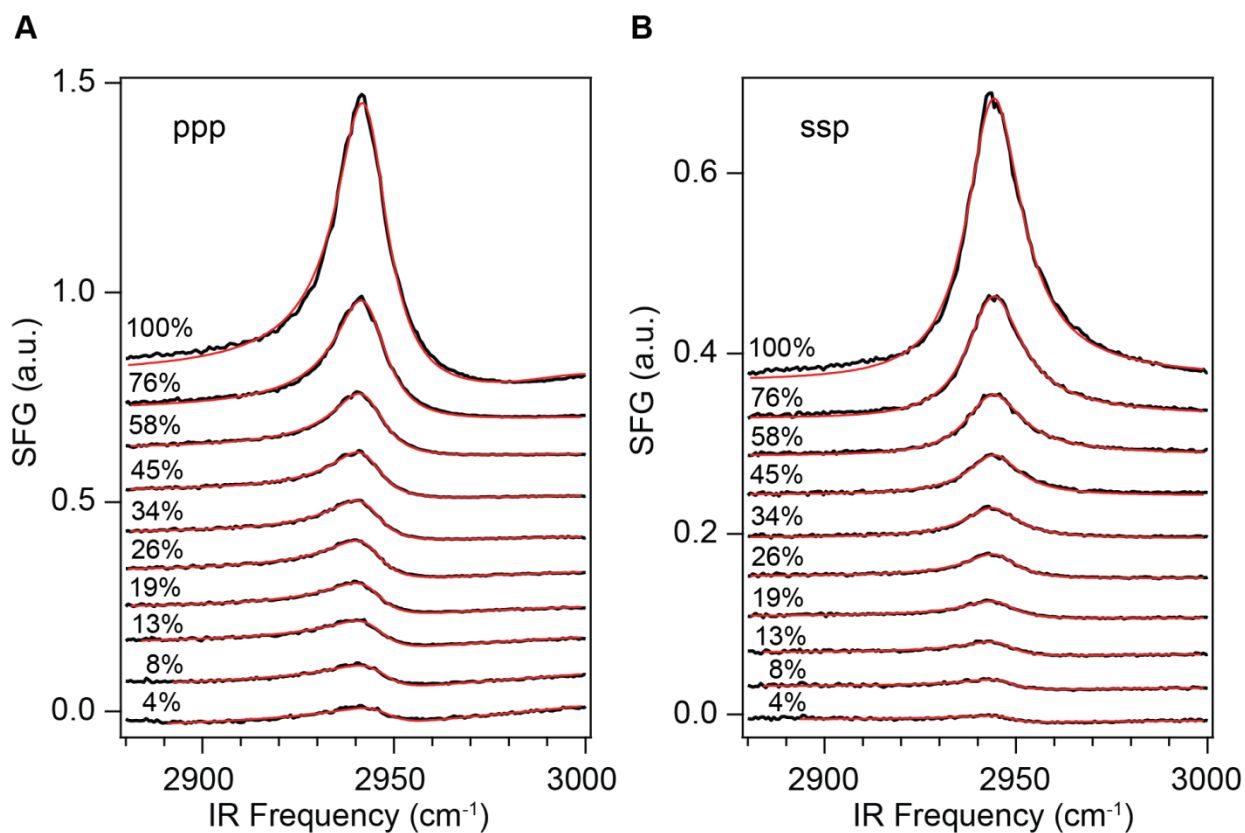
Figure 5.3 SFG spectra of acetonitrile in the C-H stretching region at the silica/aqueous interface with various acetonitrile concentrations under ppp (A) and ssp (B) polarization combinations. Ten concentrations were used in the study with acetonitrile mole fraction of 4%, 8%, 13%, 19%, 26%, 34%, 45%, 58%, 76% and 100% (pure acetonitrile). In the figure, the black dots are experimental data and the solid lines are the fit with equation 5.1 using a single Lorentzian for the methyl symmetric mode.

The SFG spectra of acetonitrile in the C-H stretch region were collected from the silica/aqueous interface at various acetonitrile concentrations, and the spectra were fit using the single-Lorentzian model (Figure 5.3). For the ppp spectra, in addition to the Lorentzian peak accounting for the methyl symmetric stretch, another broad Lorentzian peak arising from the

strongly hydrogen-bonded water that has a central frequency of 3200 cm^{-1}, was included at low acetonitrile concentrations (n_{ACN}% ≤ 45%, Figure 5.3A). For the ssp spectra, only one Lorentzian peak was used (Figure 5.3B).
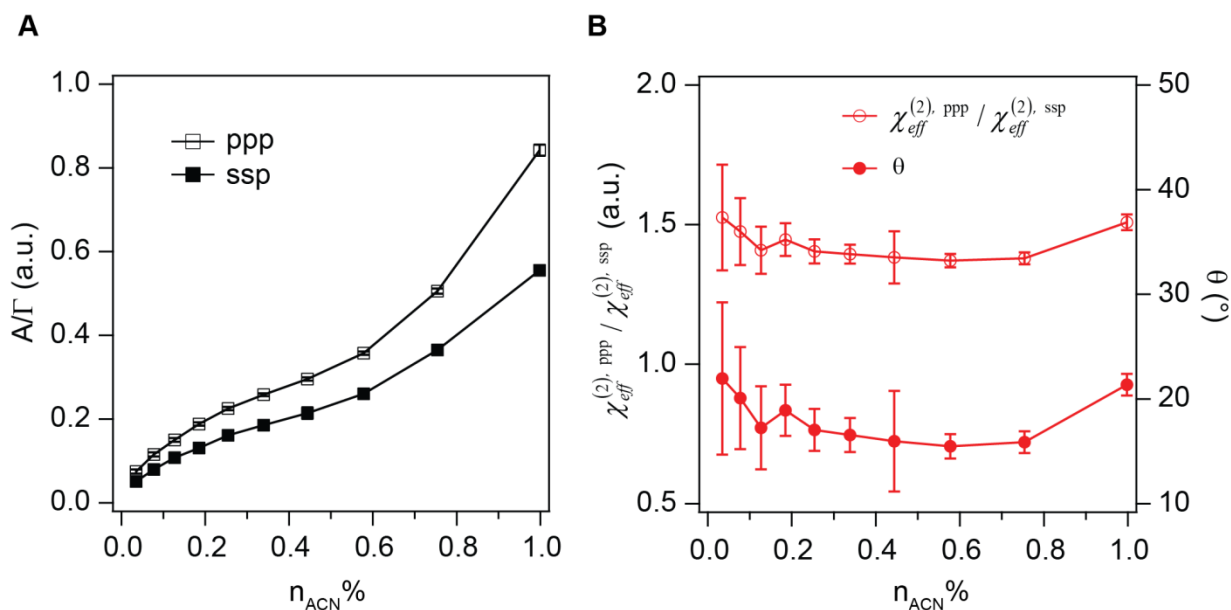
Figure 5.4 (A) The ratio of peak amplitude and peak width (A/Γ) for the methyl symmetric stretch mode at different acetonitrile mole fractions (n_{ACN}%) under ppp and ssp polarization combinations. (B) The value of $\chi_{eff}^{(2),\ ppp} / \chi_{eff}^{(2),\ ssp}$ and tilt angle θ at different n_{ACN}%.

As shown in Figure 5.4A, the ratio of peak amplitude and peak width (A/Γ) for the methyl symmetric stretch mode was plotted versus the concentration of acetonitrile (mole fraction). As expected, the A/Γ ratio for the methyl symmetric stretch mode decreased as the mole fraction of acetonitrile decreased from 100% to 4%.[250] This decrease may be attributed to two possible reasons: firstly, the number density of acetonitrile molecule in the interfacial region decreased as the concentration of acetonitrile decreased; secondly, the net orientation of acetonitrile molecules changed as the composition of the acetonitrile/water mixture changed.

For a rotationally isotropic interface like the silica/acetonitrile or silica/acetonitrile:water mixture interface studied in this project, which has the symmetry of C$_{\infty v}$, there are only seven non-zero second-order nonlinear susceptibility tensor elements.[62-64] By taking polarization-resolved SFG spectra, the relative amplitude of these non-zero tensor elements can be extracted. Determination of these non-zero tensor elements allows deduction of the orientation of the interfacial molecules.

For the methyl symmetric stretch mode (ss-CH$_3$), expressions for the effective second-order nonlinear susceptibility, $\chi_{eff}^{(2)}$, under different polarization combinations are shown in the following equations:[81, 87, 195, 267]

$$
\begin{aligned}
\chi_{eff}^{(2),\,ssp} &= L_{YY}(\omega_{SFG})L_{YY}(\omega_{vis})L_{ZZ}(\omega_{IR})\sin\beta_2\,\chi_{YYZ}^{(2)} \\
\chi_{eff}^{(2),\,sps} &= L_{YY}(\omega_{SFG})L_{ZZ}(\omega_{vis})L_{YY}(\omega_{IR})\sin\beta_1\,\chi_{YZY}^{(2)} \\
\chi_{eff}^{(2),\,pss} &= L_{ZZ}(\omega_{SFG})L_{YY}(\omega_{vis})L_{YY}(\omega_{IR})\sin\beta\,\chi_{ZYY}^{(2)} \\
\chi_{eff}^{(2),\,ppp} &= -L_{XX}(\omega_{SFG})L_{XX}(\omega_{vis})L_{ZZ}(\omega_{IR})\cos\beta\cos\beta_1\sin\beta_2\,\chi_{XXZ}^{(2)} \\
&\quad - L_{XX}(\omega_{SFG})L_{ZZ}(\omega_{vis})L_{XX}(\omega_{IR})\cos\beta\sin\beta_1\cos\beta_2\,\chi_{XZX}^{(2)} \\
&\quad + L_{ZZ}(\omega_{SFG})L_{XX}(\omega_{vis})L_{XX}(\omega_{IR})\sin\beta\cos\beta_1\cos\beta_2\,\chi_{ZXX}^{(2)} \\
&\quad + L_{ZZ}(\omega_{SFG})L_{ZZ}(\omega_{vis})L_{ZZ}(\omega_{IR})\sin\beta\sin\beta_1\sin\beta_2\,\chi_{ZZZ}^{(2)}
\end{aligned}
\tag{5.4}
$$

where X, Y and Z are the laboratory axes, L_{II} ($I = X, Y, Z$) is the Fresnel coefficient of the incident light polarized in the I direction, β_1 is the incidence angle of the visible light, β_2 is the incidence angle of the IR light, and β is the reflection angle of the generated SFG light.

For a single methyl group, the non-zero hyperpolarizability elements of the symmetric stretch mode (ss-CH$_3$) have the following relationship:[268-269]

$$
\beta_{xxz}^{(2)} = \beta_{yyz}^{(2)} \approx 2.2\beta_{zz}^{(2)}
\tag{5.5}
$$

where x, y and z are the molecular axes, and z is the long molecular axis along the C_3 axis of the methyl group.

Euler transformation is needed to correlate the molecular coordinate system (xyz) and the laboratory coordinate system (XYZ). Three Euler angles: the in-plane rotation angle ϕ, tilt angle θ and twist angle ψ, are involved in the transformation. Details about these three parameters have been described in Chapter 1. Considering the symmetry of the silica/ACN$_{(l)}$ and silica/ACN$_{(aq)}$ interface and the highly symmetric structure of acetonitrile molecule, it is reasonable to assume the interfacial acetonitrile molecule has a random distribution in both the in-plane rotation angle ϕ and twist angle ψ. Consequently, the tilt angle θ is the only parameter left to be determined, which represents the angle between the molecular axis z and the surface normal (laboratory axis Z). After simplification, for the methyl symmetric stretch mode (ss-CH$_3$), the non-zero susceptibility elements have the following expressions:[81, 87, 195, 267]

$$\chi_{XXZ}^{(2)} = \chi_{YYZ}^{(2)} = \frac{1}{2}N\left[\beta_{zz}^{(2)}\left(1-\cos^2\theta\right)\cos\theta + \beta_{xxz}^{(2)}\left(1+\cos^2\theta\right)\cos\theta\right]$$

$$\chi_{XZX}^{(2)} = \chi_{ZXX}^{(2)} = \chi_{YZY}^{(2)} = \chi_{ZYY}^{(2)} = \frac{1}{2}N\left[\left(\beta_{zz}^{(2)} - \beta_{xxz}^{(2)}\right)\times\left(1-\cos^2\theta\right)\cos\theta\right] \qquad (5.6)$$

$$\chi_{ZZZ}^{(2)} = N\left[\beta_{zz}^{(2)}\cos^3\theta + \beta_{xxz}^{(2)}\left(1-\cos^2\theta\right)\cos\theta\right]$$

where N is the number density of interfacial acetonitrile molecule.

At each acetonitrile concentration, knowing the value of A/Γ for the methyl symmetric stretch mode under ppp and ssp polarization combinations, it is easy to find the ratio of these two, which is proportional to the value of $\chi_{eff}^{(2),\,ppp} / \chi_{eff}^{(2),\,ssp}$. As shown in Figure 5.4B, the value of $\chi_{eff}^{(2),\,ppp} / \chi_{eff}^{(2),\,ssp}$ was plotted versus the concentration of acetonitrile. By using equation 5.4-5.6, the tilt angle θ can be readily determined at each acetonitrile concentration according to:

$$\theta = \arccos\sqrt{\dfrac{-\dfrac{\dfrac{\beta_{xxz}}{\beta_{zzz}}+1}{\dfrac{\beta_{xxz}}{\beta_{zzz}}-1}a_1 + a_2 + a_3 - \dfrac{\dfrac{2\beta_{xxz}}{\beta_{zzz}}}{\dfrac{\beta_{xxz}}{\beta_{zzz}}-1}a_4 + \dfrac{\dfrac{\beta_{xxz}}{\beta_{zzz}}+1}{\dfrac{\beta_{xxz}}{\beta_{zzz}}-1}\cdot\dfrac{\chi_{eff}^{(2),\,ppp}}{\chi_{eff}^{(2),\,ssp}}a_5}{a_1 + a_2 + a_3 - 2a_4 - \dfrac{\chi_{eff}^{(2),\,ppp}}{\chi_{eff}^{(2),\,ssp}}a_5}}$$

$$= \arccos\sqrt{\dfrac{-\dfrac{8}{3}a_1 + a_2 + a_3 - \dfrac{11}{3}a_4 + \dfrac{8}{3}\cdot\dfrac{\chi_{eff}^{(2),\,ppp}}{\chi_{eff}^{(2),\,ssp}}a_5}{a_1 + a_2 + a_3 - 2a_4 - \dfrac{\chi_{eff}^{(2),\,ppp}}{\chi_{eff}^{(2),\,ssp}}a_5}}$$

(5.7)

where a_1, a_2, a_3, a_4 and a_5 are constants with the following expression:

$$a_1 = L_{YY}(\omega_{SFG})L_{YY}(\omega_{vis})L_{ZZ}(\omega_{IR})\sin\beta_2$$
$$a_2 = -L_{XX}(\omega_{SFG})L_{XX}(\omega_{vis})L_{ZZ}(\omega_{IR})\cos\beta\cos\beta_1\sin\beta_2$$
$$a_3 = -L_{XX}(\omega_{SFG})L_{ZZ}(\omega_{vis})L_{XX}(\omega_{IR})\cos\beta\sin\beta_1\cos\beta_2$$
$$a_4 = L_{ZZ}(\omega_{SFG})L_{XX}(\omega_{vis})L_{XX}(\omega_{IR})\sin\beta\cos\beta_1\cos\beta_2$$
$$a_5 = L_{ZZ}(\omega_{SFG})L_{ZZ}(\omega_{vis})L_{ZZ}(\omega_{IR})\sin\beta\sin\beta_1\sin\beta_2$$

(5.8)

Assuming a narrow distribution, the tilt angle θ was found to be in the range of 15-21° for all acetonitrile concentrations, indicating there was no significant change in the net orientation of interfacial acetonitrile molecule as the mole fraction of acetonitrile decreased from 100% to 4%. In other words, the decrease in the number density of interfacial acetonitrile molecule is the dominant reason why the SFG intensity decreased at less acetonitrile concentration. The average value of 18° is similar to the values determined in previous studies at other mineral oxide surfaces. For example, Rabinowitz and co-workers found that acetonitrile bound to zirconia with a tilt angle of around 20°,[270-271] and Williams and co-workers found that acetonitrile bound to alumina with a tilt angle of approximately 21°, and bound to zirconia with a tilt angle of approximately 24°.[272]
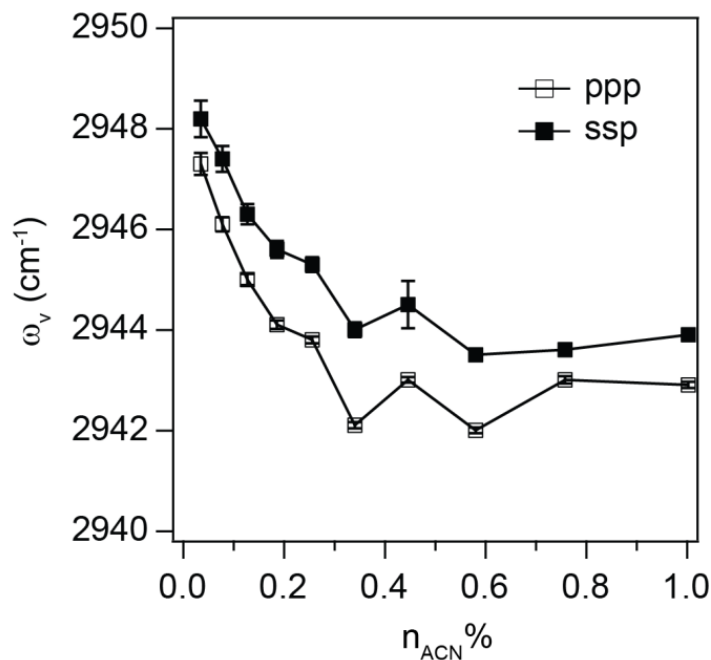
Figure 5.5 Frequency of the methyl symmetric stretch mode (ss-CH_3) at different acetonitrile concentrations under ppp and ssp polarization combinations.

In addition to analyzing the orientation of the methyl groups as a function of acetonitrile concentration, we also monitored the wavenumber of the methyl symmetric stretch at each acetonitrile concentration (Figure 5.5). We found as the acetonitrile concentration decreased gradually from 100% to 4%, the frequency of the methyl symmetric stretch had a blue shift by approximate 5 cm^{-1}. The exponential change is also consistent with the study by Fourkas and co-workers,[250] in which they found two types of methyl symmetric stretch modes at the silica/aqueous interface, and the frequencies of both blue shifted as the acetonitrile concentration decreased. This frequency blue shift for the methyl symmetric stretch was attributed to the interaction of water with the methyl groups.

5.3.4 SFG Spectra of Acetonitrile from Silica/Aqueous Interface at Various pH Values
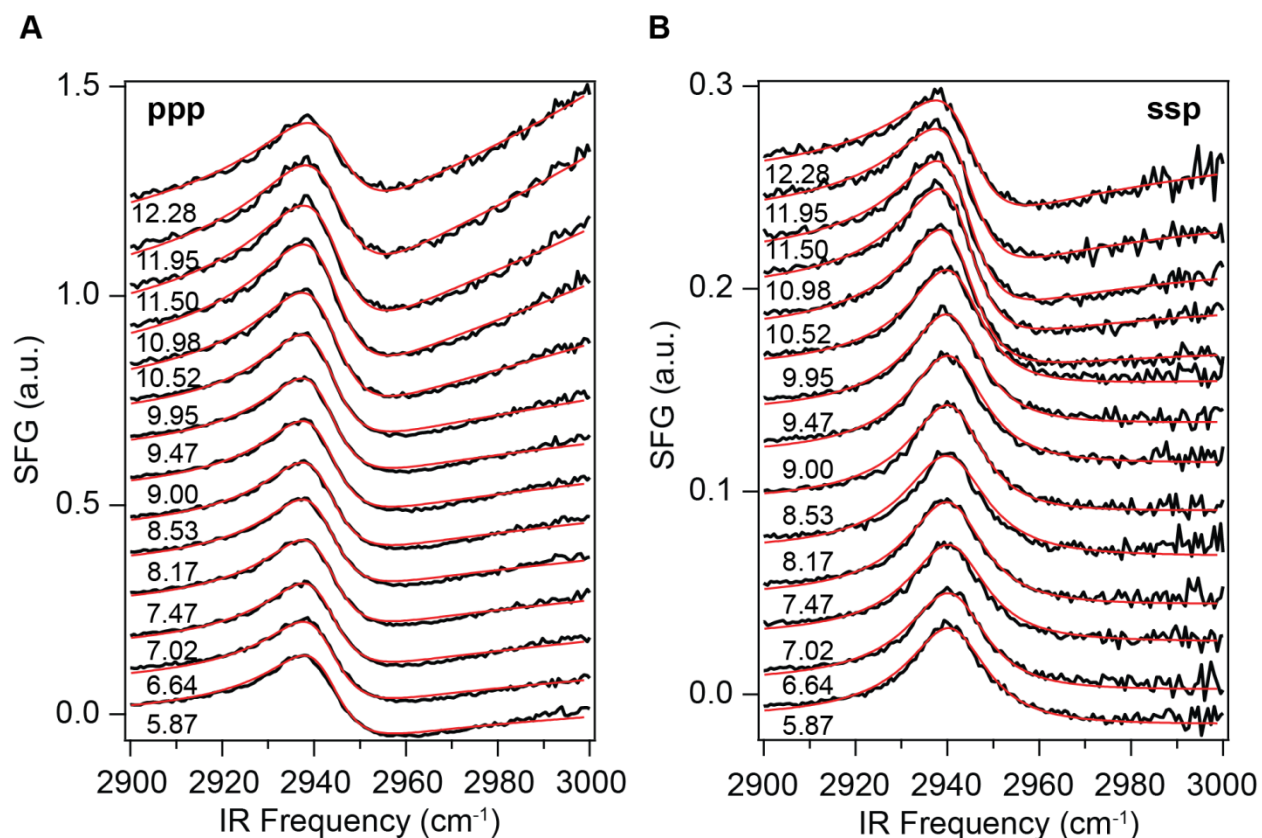
Figure 5.6 SFG spectra of acetonitrile in the C-H stretch region collected from silica/aqueous interface at various aqueous pH values under ppp (A) and ssp (B) polarization combinations. The mole fraction of acetonitrile in the mixture was 19%. The entire solution mixture contained 10 mM NaCl background salt. In the figure, the black dots are experimental data and the solid lines are theoretical fitting using equation 5.1.

SFG spectra of acetonitrile in the C-H stretch region were also collected from the silica/aqueous interface at various aqueous pH values. An aqueous stock solution (1 L) was stepwise adjusted from neutral pH (5.9) to strongly basic pH (12.3) using a concentrated NaOH aqueous solution. At each aqueous pH value, 6-mL aqueous solution was mixed with 4-mL acetonitrile to make 10 mL mixture solution, in which the mole fraction of acetonitrile was 19%. SFG spectra were collected for each mixture solution and fit using equation 5.1 with one peak

accounting for the methyl symmetric stretch and another peak accounting for the strongly hydrogen bonded water (Figure 5.6). As only the tail of the water peak was measured in the spectra, both the frequency and the damping coefficient of this water peak had to be held at 3200 cm^{-1} and 50 cm^{-1}, respectively, to achieve consistent fitting. This method did definitively affect the uncertainty of the peak amplitude extracted from fitting, especially at high pH conditions; however, it did not affect the trend in A/Γ values for the methyl symmetric stretch with increasing pH.
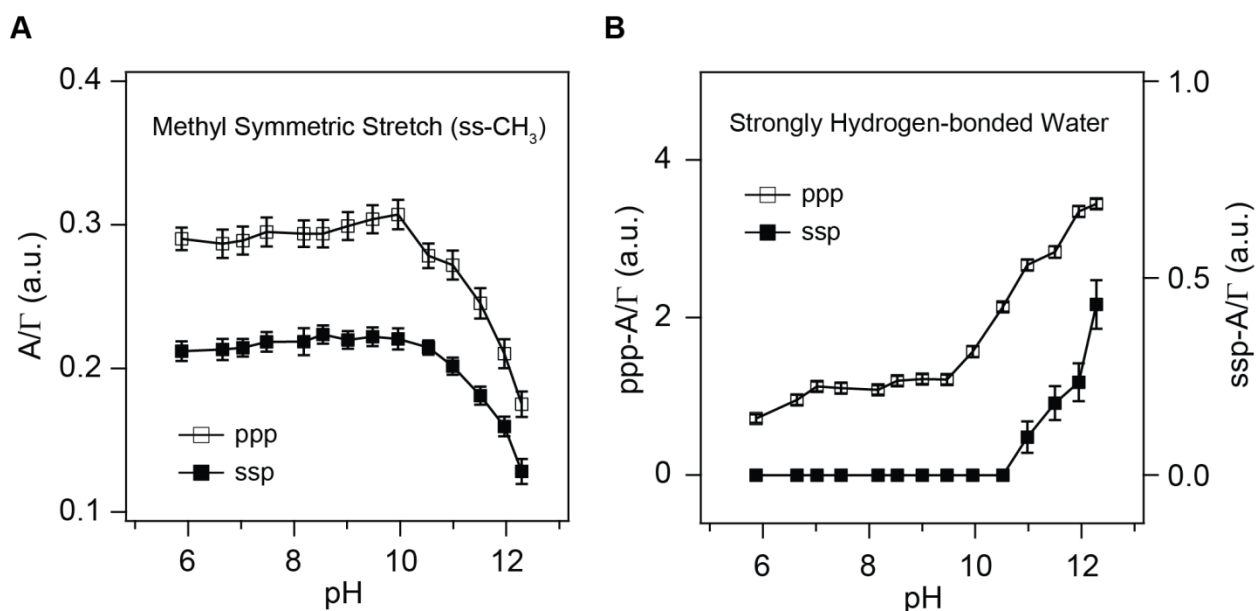
Figure 5.7 The ratio of peak amplitude and peak width (A/Γ) for methyl symmetric stretch mode (A) and strongly hydrogen bonded water O-H stretch mode (B) at different aqueous solution pH values under ppp and ssp polarization combinations. The mole fraction of acetonitrile in the acetonitrile/water mixture was 19%. The entire solution mixture contained 10 mM NaCl background salt. The frequency of the water O-H stretch peak had to be held as 3200 cm^{-1} with a peak width of 50 cm^{-1}, as only the tail of this peak was measured in the spectra.

After fitting, the ratio of the peak amplitude and peak width (A/Γ) for the methyl symmetric

stretch was plotted versus solution pH in Figure 5.7A. The A/Γ value did not change much when pH < 10, yet underwent a dramatic decrease when pH > 10. At the same time, for the strongly hydrogen bonded water peak, the A/Γ value did not change much either when pH < 10, but underwent a dramatic increase when pH > 10.

At neutral pH, the silica surface is negatively charged, and the surface charge generates an electric field, which induces the alignment of water molecules in the interfacial region leading to the water tail in the C-H stretching region, which is only notable in the ppp spectrum. According to the SFG study by Shen and co-workers at the silica/water interface, as the solution pH is increased, more surface silanol groups are deprotonated which results in a stronger interfacial potential and more aligned water molecules. Consequently a stronger SFG signal in the water O-H stretch region is observed.[273] Our fitting result of the water peak is consistent with this interpretation, indicating more water molecules were aligned at the interface as the pH increased, although acetonitrile existed in the mixture (Figure 5.7B). The striking plateau in the A/Γ value between pH 6 and 10 is similar to the changes in water spectrum for the pure water interface.[273] This indicates that the presence of acetonitrile does not affect the silica surface deprotonation while the solution changes from neutral to basic.

The decrease of the A/Γ value for the methyl symmetric stretch peak under both ppp and ssp polarization suggested that the number of acetonitrile molecule aligned in the interfacial region decreased as solution pH increased. This observation was not surprising as acetonitrile is known to form hydrogen bonds by donation of surface silanol groups to the hydrogen-bond accepting cyanide group. As the solution pH increased, more silanol groups were deprotonated to siloxides, which effectively form hydrogen bonds with water (now as hydrogen-bond acceptors), but not acetonitrile. At high solution pH, acetonitrile molecules may still align within the

interfacial water layer through hydrogen bonds between cyanide and the remaining silanols (80% remain even at pH 12),[274] retaining a certain amount of acetonitrile in the interfacial region. Although a high density of silanols remain even at high pH, the loss of more than half of the aligned acetonitrile molecules based on the change in A/Γ indicates that the more negative interfacial potential makes it more difficult to align ACN, which has its dipole moment pointed towards the negatively charged interface.

5.4 Conclusion

In conclusion, the SFG spectra of acetonitrile in the C-H stretch region were collected from the silica/aqueous interface at various acetonitrile concentrations and at a variety of pH values. As expected based on previous work a strong peak attributed to the methyl symmetric stretch within acetonitrile molecule was observed in both ppp and ssp spectra. Unlike previous studies, however, in which double-Lorentzian models were necessary to fit this peak, a single Lorentzian model was found to be suitable to fit our data. Additionally, orientation analysis of this mode suggested that the net orientation of interfacial acetonitrile molecules did not change significantly as the acetonitrile concentration decreased. At a certain acetonitrile/water composition ($n_{ACN}\% = 19\%$), increasing solution pH from neutral value to strongly basic value effectively decreased the number density of interfacial acetonitrile molecule also without significantly altering their average tilt angle. This work indicates that the bilayer structure at the silica interface changes density but not the overall ordering of the acetonitrile molecules based on their consistent tilt angles even with significant changes to the mixture composition and pH. Furthermore, the trend in the amount of aligned acetonitrile with increasing pH indicated that the

amount of deprotonated silanols remained constant between pH 6 and pH 10, which is similar to

the acid-base behavior of the pure water/silica interface.[273]

Chapter 6

General Conclusion and Future Work

6.1 General Conclusion and Future Work

This thesis mainly has focused on characterizing the structure and order of molecules at silica and functionalized silica surfaces and investigating the thermodynamics and kinetics of processes at the silica/liquid and functionalized silica/liquid interfaces using the nonlinear optical techniques vibrational sum frequency generation (SFG) and second harmonic generation (SHG). Taking advantage of these surface-specific techniques, we were able to follow processes at interfaces in real-time and extract information about specific interfacial phenomena.

In Chapter 2, we prepared two kinds of organocatalysts, silica supported amine and silica supported ureido monolayers. At the acetonitrile/solid interface, the binding of a model reactant 4-nitroacetophenone with these silica-supported monolayers was studied using a combination of SHG and vibrational SFG. Binding isotherms yielded binding energies consistent with the formation of hydrogen bond between carbonyl groups in the model reactant and the hydrogen bond accepter on the modified silica surface. We also found, the local environment of the silica supported organocatalysts had a strong effect on the binding affinity of the model reactant. Specifically, the binding energy of 4-nitroacetophenone on ureido monolayers was much less than the binding energy on amine monolayers despite the fact that urea can form two hydrogen bonds with carbonyl groups. The SFG study indicated that the presence of a hydrogen bond network within ureido monolayers that must be disrupted to facilitate ketone binding is responsible for the lower binding affinity of 4-nitroacetoohenone on ureido monolayers.

Overall, this project focused on the study of mono-functionalized silica catalyst, in which only one kind of organocatalyst molecule is immobilized on the silica support. Other than mono-functionalized silica catalysts, multi-functionalized silica catalysts, which consist of two or more kinds of organocatalyst molecules on the same solid support, is another class of important

heterogeneous catalysts.[9, 275-283] For example, Lin proposed a bifunctional catalytic system consisting of a Lewis basic amine (for activating a nucleophile) and a Lewis acidic urea (for activating an electrophile). This combination can catalyze several different reactions involving carbonyl and nucleophile activation by a cooperative effect.[140] Although the components of this bifunctional system, silica-supported amine or silica-supported urea monolayers, can still catalyze some of the same reactions separately, the bifunctional system was found to be much more effective. In order to gain more understanding of the cooperative mechanism, exploring the interactions between the reactant and the bifunctional catalytic system would be the first step. For future work, we may prepare bifunctional silica supported catalyst systems, which consists of both amine and ureido monolayers on the same piece of silica support, and study its performance in related catalytic reactions. Similarly, the bonding affinity of a model reactant on the bifunctional silica surface can be determined using resonant SHG, then the mole ratio of the two components on the silica surface will be optimized to seek a maximum binding affinity. Taking advantage of the sensitivity of vibrational signatures of molecule, SFG can be employed to study the structure and orientation of the surface catalyst molecule and bonded model reactant molecule.

In Chapter 3, we studied the reaction mechanism of the Cu(I)-catalyzed 1,3-dipolar azide-alkyne cycloaddition (CuAAC) at the silica interface using SFG. An organo azide monolayer was prepared on a CaF_2-supported silica surface and a strong peak at 2096 cm^{-1} assigned to the asymmetric stretch of azide group was observed at the silica/methanol interface for the first time by SFG. Using a cyano-substituted alkyne, the surface CuAAC reaction was followed by monitoring the decrease of the azide peak and the increase of the cyano peak in the SFG spectra.

Kinetic analysis revealed that the reaction order with respect to copper was 2.1, suggesting that two coppers are needed in the rate determining step.

In this project, we found the azide group and its reactivity can be followed in real time using vibrational SFG. As the azide is unreactive with functional groups that occur in biological systems, it can be used as an SFG label to investigate the thermodynamics and kinetics of interfacial biochemical reactions, for example, the phospholipase catalyzed hydrolysis of lipid bilayer. As interfacial enzymes that catalyze the hydrolysis of cellular L-phospholipids, phospholipase play an important role in many biochemical processes.[284-285] In order to improve the understanding of phospholipase and the mechanism of phospholipase-catalyzed hydrolysis process, planar supported lipid bilayer has been used as a model to mimic many aspects of cell membrane behavior,[120, 286-293] and SFG has been employed to study the reaction kinetics of phospholipase-catalyzed hydrolysis.[107] The behavior of lipid bilayers was studied with SFG by monitoring different vibrational modes within the lipid molecule, and the most common region of interest is the C-H stretch region, as lipid molecules are rich in C-H groups including methyl, methylene and methine. There are some downsides of this approach. Firstly, D_2O is usually used to avoid the disturbance of the strongly hydrogen bonded water peak, which has a center frequency of 3200 cm^{-1} and has a intense tail in the C-H stretch region in SFG spectra. Secondly, the C-H stretching region is congested with multiple vibrational modes, so peak assignment becomes difficult. To solve these problems, we can introduce azide groups into the lipid molecule.[294] By using azide-modified lipid bilayers, the enzyme catalyzed hydrolysis reaction can be followed in the azide asymmetric stretch region, and information about the reaction mechanism can be easily extracted.

In Chapter 4, we monitored the thermal dissociation of immobilized DNA duplexes using vibrational SFG. A thymidine 15-mer (T_{15}) monolayer was immobilized on silica using the CuAAC reaction, and the interactions of the silica supported T_{15} strands with complementary A_{15} strands from solution were studied using SFG in the C-H stretch region. The most temperature-sensitive mode was attributed to the methyl groups on the T_{15} strand, which should experience significant reorientation upon duplex dissociation. Fitting of the ratio of peak amplitude and peak width of the methyl symmetric stretch peak versus temperature revealed a melting temperature that is ~ 12 °C lower than the solution-phase melting temperature, indicating that immobilization on silica destabilized the DNA duplexes leading to a low dissociation temperature. This conclusion is important for the application of DNA microarray chips, which are of great use in disease diagnostics and pathogen detection,[295-296] as thermal stringency washes are normally used to remove all the mismatched DNA sequences after hybridization of the immobilized DNA single strand with the complementary stand in solution. It is necessary to control the highest temperature of thermal stringency to avoid the dissociation of perfectly hybridized DNA sequences.[162, 214, 248]

In this project, the experiment was done using a buffer solution, which kept the solution pH unchanged during the whole hybridization and dissociation process. But the solution pH is another factor that can affect the hybridization of immobilized DNA duplexes,[297] so future work may aim to understand the pH dependent behavior of immobilized DNA and the influence of pH on the hybridization and dissociation of immobilized DNA duplexes on silica. SFG spectra in this project were collected in the C-H stretch region, but as mentioned early, there are some disadvantages of collecting spectra in this region. To improve this method, we can also introduce azide groups into the structure of the DNA strand, then the hybridization of immobilized DNA

duplexes can be monitored in the azide asymmetric stretch region using SFG without the disturbance of the water peak.

In Chapter 5, we studied the interfacial organization of acetonitrile at the silica surface using SFG with and without the presence of water as a co-solvent. SFG spectra were collected in the C-H stretching region from the silica/aqueous interface at various acetonitrile concentrations, and a strong peak attributed to the methyl symmetric stretch of acetonitrile was observed in both ppp and ssp spectra. A single-Lorentzian model was employed to fit the spectra, and orientation analysis indicated the net orientation of interfacial acetonitrile molecules did not change much as the acetonitrile concentration decreased. At a certain acetonitrile/water composition, increasing the solution pH from a neutral value to a strongly basic value effectively decreased the number density of interfacial acetonitrile molecules. As the acetonitrile/water mixture is a widely used mobile phase in chromatography,[251-258] the study of the interfacial organization of acetonitrile molecules at the silica surface under different solution compositions and pH will help the understanding of the movement and separation of different components in chromatography. Future work will be done by collecting SFG spectra under different solution pH conditions at various acetonitrile/water compositions. Meanwhile, as buffer is usually used instead of pure water in chromatography, the presence of salt may be another factor that can affect the interfacial organization of acetonitrile molecules. So the effect of salt concentration on the interfacial organization of acetonitrile will be another interesting topic to study. Furthermore, the SFG spectra in this project were collected in the C-H stretch region, and in order to get more complementary information, SFG spectra can be also collected in the cyano stretch region (2230-2260 cm^{-1}).

6.2 Perspective

As surface-specific techniques, SHG and SFG are well-suited to study the properties of interfacial molecules, and consequently they have been employed to study various interfacial phenomena in different areas. The advantages of these nonlinear optical techniques become more noticeable when the application involves buried interfaces and insulator substrate. The application of these techniques to the study of immobilized catalysts, particularly on insulators like silica which is the most commonly used substrate for catalyst immobilization, has a great deal of potential because of the difficulty in monitoring processes on such surfaces.

To study interfaces involving organic molecules, there are some specific issues to note. First of all, during exposure to laser beams, the stability of a molecule is the first factor that has to be considered. Normally, relatively low laser power has to be used to avoid damaging the sample. However, the nonlinear response of the system with respect to incident electric field is only generated when the incident electric field is high enough. The sensitivity of the interface to laser intensity was a particular problem in SHG experiments at the acetonitrile/silica interface but we were able to achieve satisfactory signal levels with attenuated power. For some extremely unstable systems, however, instead of using lower laser power, a computer-controlled moving sample stage may be needed to solve this problem.

Secondly, for studies involving immobilized molecules, the preparation and characterization of the immobilized monolayer is important. Especially, when a mixed monolayer or a bifunctional system is studied, the preparation and characterization step will be difficult but critical. The performance of the surface determines the results from laser experiments to a great extent.

References

1.   Cao, H.; Zhou, C.; Ma, J.; Wu, J.; Li, S., High-Efficiency Fused-Silica Reflection Grism. *Appl. Opt.* **2014**, *23*, 2802-2805.

2.   Hung, T. Y.; Su, C. S., Fused-Silica Focusing Lens for Deep UV Laser Processing. *Appl. Opt.* **1992**, *31*, 4397-4404.

3.   Scaggs, M.; Haas, G., Thermal Lensing Compensation Optic for High Power Lasers. In *Proc. SPIE 7913, Laser Resonators and Beam Control XIII*, San Francisco, CA, 2011; p 79130C.

4.   Ge, T. S.; Dai, Y. J.; Wang, R. Z., Desiccant Materials and Their Applications. In *Advances in Adsorption Technology*, Saha, B. B.; Ng, K. C., Eds. Nova Science Publishers, Inc: Hauppauge, 2010; pp 367-394.

5.   Sajewicz, M.; Kowalska, T., On the Mechanisms of Enantiomer Separations by Chiral Thin-Layer Chromatography on Silica Gel, and Implications When Densitometric Detection Is Used. A Mini Review. *Acta Chromatogr.* **2010**, *22*, 499-513.

6.   Bergna, H. E.; Roberts, W. O., *Colloidal Silica: Fundamentals and Applications*; Boca Raton, FL: CRC Taylor & Francis, 2006.

7.   Corma, A.; Garcia, H., Silica-Bound Homogenous Catalysts as Recoverable and Reusable Catalysts in Organic Synthesis. *Adv. Synth. Catal.* **2006**, *348*, 1391-1412.

8.   Gruttadauria, M.; Giacalone, F.; Noto, R., Supported Proline and Proline-Derivatives as Recyclable Organocatalysts. *Chem. Soc. Rev.* **2008**, *37*, 1666-1688.

9.   Rostamnia, S.; Doustkhah, E., Nanoporous Silica-Supported Organocatalyst: A Heterogeneous and Green Hybrid Catalyst for Organic Transformations. *RSC Adv.* **2014**, 28238-28248.

10.   Shylesh, S.; Wagner, A.; Seifert, A.; Ernst, S.; Thiel, W. R., Cooperative Acid-Base Effects with Functionalized Mesoporous Silica Nanoparticles: Applications in Carbon-Carbon Bond-Formation Reactions. *Chem. Eur. J.* **2009**, *15*, 7052-7062.

11.   Yokoi, T.; Kubota, Y.; Tatsumi, T., Amino-Functionalized Mesoporous Silica as Base Catalyst and Adsorbent. *Appl. Catal. A-Gen.* **2012**, *421*, 14-37.

12.   Ispas, C.; Sokolov, I.; Andreescu, S., Enzyme-Functionalized Mesoporous Silica for Bioanalytical Applications. *Anal. Bioanal. Chem.* **2009**, *393*, 543-554.

13.   Phaner-Goutorbe, M.; Dugas, V.; Chevolot, Y.; Souteyrand, E., Silanization of Silica and Glass Slides for DNA Microarrays by Impregnation and Gas Phase Protocols: A Comparative Study. *Mater. Sci. Eng. C* **2011**, *31*, 384-390.

14.   Bae, S. W.; Cho, M. S.; Hur, S. S.; Chae, C. B.; Chung, D. S.; Yeo, W. S.; Hong, J. I., A Doubly Signal-Amplified DNA Detection Method Based on Pre-Complexed $[Ru(Bpy)_3]^{2+}$-Doped Silica Nanoparticles. *Chem. Eur. J.* **2010**, *16*, 11572-11575.

15.   Bras, M.; Dugas, V.; Bessueille, F.; Cloarec, J. P.; Martin, J. R.; Cabrera, M.; Chauvet, J. P.; Souteyrand, E.; Garrigues, M., Optimisation of a Silicon/Silicon Dioxide Substrate for a Fluorescence DNA Microarray. *Biosens. Bioelectron.* **2004**, *20*, 797-806.

16.   Adamson, A. W.; Gast, A. P., *Physical Chemistry of Surfaces, 6th Ed.*; New York: Wiley, 1997.

17.   Williams, C. T.; Beattie, D. A., Probing Buried Interfaces with Non-Linear Optical Spectroscopy. *Surf. Sci.* **2002**, *500*, 545-576.

18.   Ulman, A., Formation and Structure of Self-Assembled Monolayers. *Chem. Rev.* **1996**, *96*, 1533-1554.

19.	Love, J. C.; Estroff, L. A.; Kriebel, J. K.; Nuzzo, R. G.; Whitesides, G. M., Self-Assembled Monolayers of Thiolates on Metals as a Form of Nanotechnology. *Chem. Rev.* **2005**, *105*, 1103-1169.

20.	Schreiber, F., Structure and Growth of Self-Assembling Monolayers. *Prog. Surf. Sci.* **2000**, *65*, 151-256.

21.	Feng, X.; Fryxell, G. E.; Wang, L. Q.; Kim, A. Y.; Liu, J.; Kemner, K. M., Functionalized Monolayers on Ordered Mesoporous Supports. *Science* **1997**, *276*, 923-926.

22.	Kumar, A.; Biebuyck, H. A.; Whitesides, G. M., Patterning Self-Assembled Monolayers - Applications in Materials Science. *Langmuir* **1994**, *10*, 1498-1511.

23.	Luderer, F.; Walschus, U., Immobilization of Oligonucleoticles for Biochemical Sensing by Self-Assembled Monolayers: Thiol-Organic Bonding on Gold and Silanization on Silica Surfaces. In *Immobilisation of DNA on Chips I, Topics in Current Chemistry*, Wittmann, C., Ed. Springer-Verlag Berlin: 2005; Vol. 260, pp 37-56.

24.	Zucca, P.; Sanjust, E., Inorganic Materials as Supports for Covalent Enzyme Immobilization: Methods and Mechanisms. *Molecules* **2014**, *19*, 14139-14194.

25.	Zhao, X.; Kopelman, R., Mechanism of Organosilane Self-Assembled Monolayer Formation on Silica Studied by Second-Harmonic Generation. *J. Phys. Chem.* **1996**, *100*, 11014-11018.

26.	Silberzan, P.; Leger, L.; Ausserre, D.; Benattar, J. J., Silanation of Silica Surfaces. A New Method of Constructing Pure or Mixed Monolayers. *Langmuir* **1991**, *7*, 1647-1651.

27.	Mittal, K. L., *Advances in Contact Angle, Wettability and Adhesion*; Salem, Mass.: Scrivener/Wiley, 2013.

28. Janssen, D.; De Palma, R.; Verlaak, S.; Heremans, P.; Dehaen, W., Static Solvent Contact Angle Measurements, Surface Free Energy and Wettability Determination of Various Self-Assembled Monolayers on Silicon Dioxide. *Thin Solid Films* **2006**, *515*, 1433-1438.

29. Dulcey, C. S.; Georger, J. H.; Chen, M.-S.; McElvany, S. W.; O'Ferrall, C. E.; Benezra, V. I.; Calvert, J. M., Photochemistry and Patterning of Self-Assembled Monolayer Films Containing Aromatic Hydrocarbon Functional Groups. *Langmuir* **1996**, *12*, 1638-1650.

30. Haugstad, G., *Atomic Force Microscopy: Understanding Basic Modes and Advanced Applications*; Hoboken, N.J.: Wiley, 2012.

31. McGovern, M. E.; Kallury, K. M. R.; Thompson, M., Role of Solvent on the Silanization of Glass with Octadecyltrichlorosilane. *Langmuir* **1994**, *10*, 3607-3614.

32. Krasnoslobodtsev, A. V.; Smirnov, S. N., Effect of Water on Silanization of Silica by Trimethoxysilanes. *Langmuir* **2002**, *18*, 3181-3184.

33. Howarter, J. A.; Youngblood, J. P., Optimization of Silica Silanization by 3-Aminopropyltriethoxysilane. *Langmuir* **2006**, *22*, 11142-11147.

34. Zhang, F.; Srinivasan, M. P., Self-Assembled Molecular Films of Aminosilanes and Their Immobilization Capacities. *Langmuir* **2004**, *20*, 2309-2314.

35. Tompkins, H. G.; Irene, E. A., *Handbook of Ellipsometry*; Norwich, NY: William Andrew Pub.; Heidelberg, Germany: Springer, 2005.

36. Van der Heide, P., *X-Ray Photoelectron Spectroscopy: An Introduction to Principles and Practices*; Hoboken, N.J.: Wiley, 2012.

37. Brewer, S. H.; Anthireya, S. J.; Lappi, S. E.; Drapcho, D. L.; Franzen, S., Detection of DNA Hybridization on Gold Surfaces by Polarization Modulation Infrared Reflection Absorption Spectroscopy. *Langmuir* **2002**, *18*, 4460-4464.

38.   Ishibashi, K.; Tanaka, K.; Hirano-Iwata, A.; Miyamoto, K.; Kimura, Y.; Niwano, M., In Situ Study of DNA Attachment and Hybridization at Silicon Surfaces by Infrared Absorption Spectroscopy. *Jpn. J. Appl. Phys.* **2008**, *47*, 3204-3208.

39.   Moses, S.; Brewer, S. H.; Lowe, L. B.; Lappi, S. E.; Gilvey, L. B. G.; Sauthier, M.; Tenent, R. C.; Feldheim, D. L.; Franzen, S., Characterization of Single- and Double-Stranded DNA on Gold Surfaces. *Langmuir* **2004**, *20*, 11134-11140.

40.   Riccardi, C. S.; Hess, D. W.; Mizaikoff, B., Surface-Modified ZnSe Waveguides for Label-Free Infrared Attenuated Total Reflection Detection of DNA Hybridization. *Analyst* **2011**, *136*, 4906-4911.

41.   Tanaka, K.; Hirano-Iwata, A.; Miyamoto, K.-i.; Kimura, Y.; Niwano, M., In Situ Surface Infrared Study of DNA Hybridization on Au Island Films Evaporated on Silicon Surfaces. *Jpn. J. Appl. Phys.* **2009**, *48*, 04C186.

42.   Barhoumi, A.; Zhang, D.; Tam, F.; Halas, N. J., Surface-Enhanced Raman Spectroscopy of DNA. *J. Am. Chem. Soc.* **2008**, *130*, 5523-5529.

43.   Braun, G.; Lee, S. J.; Dante, M.; Nguyen, T. Q.; Moskovits, M.; Reich, N., Surface-Enhanced Raman Spectroscopy for DNA Detection by Nanoparticle Assembly onto Smooth Metal Films. *J. Am. Chem. Soc.* **2007**, *129*, 6378-6379.

44.   Papadopoulou, E.; Bell, S. E. J., DNA Reorientation on Au Nanoparticles: Label-Free Detection of Hybridization by Surface Enhanced Raman Spectroscopy. *Chem. Commun.* **2011**, *47*, 10966-10968.

45.   Touahir, L.; Galopin, E.; Boukherroub, R.; Gouget-Laemmel, A. C.; Chazalviel, J. N.; Ozanam, F.; Szunerits, S., Localized Surface Plasmon-Enhanced Fluorescence Spectroscopy for

Highly-Sensitive Real-Time Detection of DNA Hybridization. *Biosens. Bioelectron.* **2010**, *25*, 2579-2585.

46.   Sapsford, K. E.; Ligler, F. S., Real-Time Analysis of Protein Adsorption to a Variety of Thin Films. *Biosens. Bioelectron.* **2004**, *19*, 1045-1055.

47.   Lehr, H. P.; Reimann, M.; Brandenburg, A.; Sulz, G.; Klapproth, H., Real-Time Detection of Nucleic Acid Interactions by Total Internal Reflection Fluorescence. *Anal. Chem.* **2003**, *75*, 2414-2420.

48.   Bain, C. D., Sum-Frequency Vibrational Spectroscopy of the Solid/Liquid Interface. *J. Chem. Soc. Faraday Trans.* **1995**, *91*, 1281-1296.

49.   Chen, Z., Investigating Buried Polymer Interfaces Using Sum Frequency Generation Vibrational Spectroscopy. *Prog. Polym. Sci.* **2010**, *35*, 1376-1402.

50.   Eisenthal, K. B., Liquid Interfaces Probed by Second-Harmonic and Sum-Frequency Spectroscopy. *Chem. Rev.* **1996**, *96*, 1343-1360.

51.   Fu, L.; Wang, Z.; Yan, E. C. Y., Chiral Vibrational Structures of Proteins at Interfaces Probed by Sum Frequency Generation Spectroscopy. *Int. J. Mol. Sci.* **2011**, *12*, 9404-9425.

52.   Geiger, F. M., Second Harmonic Generation, Sum Frequency Generation, and $\chi^{(3)}$: Dissecting Environmental Interfaces with a Nonlinear Optical Swiss Army Knife. *Annu. Rev. Phys. Chem.* **2009**, *60*, 61-83.

53.   Richmond, G. L., Molecular Bonding and Interactions at Aqueous Surfaces as Probed by Vibrational Sum Frequency Spectroscopy. *Chem. Rev.* **2002**, *102*, 2693-2724.

54.   Shen, Y. R., Surface Properties Probed by Second-Harmonic and Sum-Frequency Generation. *Nature* **1989**, *337*, 519-525.

55. Ong, S.; Zhao, X.; Eisenthal, K. B., Polarization of Water Molecules at a Charged Interface: Second Harmonic Studies of the Silica/Water Interface. *Chem. Phys. Lett.* **1992**, *191*, 327-335.

56. Zhao, X.; Ong, S.; Eisenthal, K. B., Polarization of Water Molecules at a Charged Interface. Second Harmonic Studies of Charged Monolayers at the Air/Water Interface. *Chem. Phys. Lett.* **1993**, *202*, 513-520.

57. Chen, Z.; Shen, Y. R.; Somorjai, G. A., Studies of Polymer Surfaces by Sum Frequency Generation Vibrational Spectroscopy. *Annu. Rev. Phys. Chem.* **2002**, *53*, 437-465.

58. Kubota, J.; Domen, K., Study of the Dynamics of Surface Molecules by Time-Resolved Sum-Frequency Generation Spectroscopy. *Anal. Bioanal. Chem.* **2007**, *388*, 17-27.

59. Fournier, F.; Zheng, W. Q.; Carrez, S.; Dubost, H.; Bourguignon, B., Vibrational Dynamics of Adsorbed Molecules under Conditions of Photodesorption: Pump-Probe SFG Spectra of CO/Pt(111). *J. Chem. Phys.* **2004**, *121*, 4839-4847.

60. Carter, J. A.; Wang, Z.; Dlott, D. D., Ultrafast Nonlinear Coherent Vibrational Sum-Frequency Spectroscopy Methods to Study Thermal Conductance of Molecules at Interfaces. *Acc. Chem. Res.* **2009**, *42*, 1343-1351.

61. Sutherland, R. L.; McLean, D. G.; Kirkpatrick, S., *Handbook of Nonlinear Optics, 2nd Ed.*; New York: Marcel Dekker, 2003.

62. Boyd, R. W., *Nonlinear Optics, 3rd Ed.*; Burlington, MA: Academic Press, 2008.

63. Shen, Y. R., *The Principles of Nonlinear Optics*; New York: J. Wiley, 1984.

64. Verbiest, T.; Clays, K.; Rodriguez, V., *Second-Order Nonlinear Optical Characterization Techniques: An Introduction*; Boca Raton: CRC Press, 2009.

65.   Davis, R. P.; Moad, A. J.; Goeken, G. S.; Wampler, R. D.; Simpson, G. J., Selection Rules and Symmetry Relations for Four-Wave Mixing Measurements of Uniaxial Assemblies. *J. Phys. Chem. B* **2008**, *112*, 5834-5848.

66.   Pavone, F. S.; Campagnola, P. J., *Second Harmonic Generation Imaging*; Boca Raton, CRC Press, 2014.

67.   Moad, A. J.; Simpson, G. J., A Unified Treatment of Selection Rules and Symmetry Relations for Sum-Frequency and Second Harmonic Spectroscopies. *J. Phys. Chem. B* **2004**, *108*, 3548-3562.

68.   Wang, H.-F.; Gan, W.; Lu, R.; Rao, Y.; Wu, B.-H., Quantitative Spectral and Orientational Analysis in Surface Sum Frequency Generation Vibrational Spectroscopy (SFG-VS). *Int. Rev. Phys. Chem.* **2005**, *24*, 191-256.

69.   Corn, R. M.; Higgins, D. A., Optical Second Harmonic Generation as a Probe of Surface Chemistry. *Chem. Rev.* **1994**, *94*, 107-125.

70.   Brindza, M. R.; Walker, R. A., Differentiating Solvation Mechanisms at Polar Solid/Liquid Interfaces. *J. Am. Chem. Soc.* **2009**, *131*, 6207-6214.

71.   Simpson, G. J.; Rowlen, K. L., Orientation-Insensitive Methodology for Second Harmonic Generation. 1. Theory. *Anal. Chem.* **2000**, *72*, 3399-3406.

72.   Simpson, G. J.; Rowlen, K. L., Orientation-Insensitive Methodology for Second Harmonic Generation. 2. Application to Adsorption Isotherm and Kinetics Measurements. *Anal. Chem.* **2000**, *72*, 3407-3411.

73.   Dick, B.; Gierulski, A.; Marowsky, G.; Reider, G. A., Determination of the Nonlinear Optical Susceptibility $\chi^{(2)}$ of Surface Layers by Sum and Difference Frequency Generation in Reflection and Transmission. *Appl. Phys. B* **1985**, *38*, 107.

74.   Simpson, G. J.; Westerbuhr, S. G.; Rowlen, K. L., Molecular Orientation and Angular Distribution Probed by Angle-Resolved Absorbance and Second Harmonic Generation. *Anal. Chem.* **2000**, *72*, 887-898.

75.   Zhang, T. G.; Zhang, C. H.; Wong, G. K., Determination of Molecular Orientation in Molecular Monolayers by Second-Harmonic Generation. *J. Opt. Soc. Am. B* **1990**, *7*, 902-907.

76.   Zhang, X. Y.; Cunningham, M. M.; Walker, R. A., Solvent Polarity at Polar Solid Surfaces: The Role of Solvent Structure. *J. Phys. Chem. B* **2003**, *107*, 3183-3195.

77.   Simpson, G. J.; Perry, J. M.; Ashmore-Good, C. L., Molecular and Surface Hyperpolarizability of Oriented Chromophores of Low Symmetry. *Phys. Rev. B* **2002**, *66*, 165437.

78.   Delgado, M. C. R.; Orduna, J.; Oliva, M. M.; Casado, J.; Navarrete, J. T. L., Theoretical Understanding of the Increment of Beta Upon Protonation of Pyridine Peripheral Octupolar Molecules: Toward Nonlinear Optical Sensors. *J. Chem. Phys.* **2007**, *127*, 164704.

79.   Svechkarev, D.; Kolodezny, D.; Mosquera-Vazquez, S.; Vauthey, E., Complementary Surface Second Harmonic Generation and Molecular Dynamics Investigation of the Orientation of Organic Dyes at a Liquid/Liquid Interface. *Langmuir* **2014**, *30*, 13869-13876.

80.   Fumito Araoka; Byoungchoo Park; Yoshitaka Kinoshita; Ken Ishikawa; Hideo Takezoe; Jirakorn Thisayukta; Junji Watanabe, Evaluation of the First-Order Hyperpolarizability Tensor of Bent Molecules by Means of Hyper-Rayleigh Scattering Method. *Jpn. J. Appl. Phys.* **1999**, *38*, 3526.

81.   Liu, W.-T.; Zhang, L.; Shen, Y. R., Interfacial Structures of Methanol:Water Mixtures at a Hydrophobic Interface Probed by Sum-Frequency Vibrational Spectroscopy. *J. Chem. Phys.* **2006**, *125*, 144711.

82.   Miranda, P. B.; Pflumio, V.; Saijo, H.; Shen, Y. R., Chain-Chain Interaction between Surfactant Monolayers and Alkanes or Alcohols at Solid/Liquid Interfaces. *J. Am. Chem. Soc.* **1998**, *120*, 12092-12099.

83.   Shen, Y. R.; Ostroverkhov, V., Sum-Frequency Vibrational Spectroscopy on Water Interfaces: Polar Orientation of Water Molecules at Interfaces. *Chem. Rev.* **2006**, *106*, 1140-1154.

84.   Rao, Y.; Turro, N. J.; Eisenthal, K. B., Water Structure at Air/Acetonitrile Aqueous Solution Interfaces. *J. Phys. Chem. C* **2009**, *113*, 14384-14389.

85.   Chen, X.; Sagle, L. B.; Cremer, P. S., Urea Orientation at Protein Surfaces. *J. Am. Chem. Soc.* **2007**, *129*, 15104-15105.

86.   Richmond, G. L., Structure and Bonding of Molecules at Aqueous Surfaces. *Annu. Rev. Phys. Chem.* **2001**, *52*, 357-389.

87.   Lu, R.; Gan, W.; Wu, B.-h.; Zhang, Z.; Guo, Y.; Wang, H.-f., C-H Stretching Vibrations of Methyl, Methylene and Methine Groups at the Vapor/Alcohol (N = 1−8) Interfaces. *J. Phys. Chem. B* **2005**, *109*, 14118-14129.

88.   Ma, G.; Allen, H. C., Dppc Langmuir Monolayer at the Air-Water Interface: Probing the Tail and Head Groups by Vibrational Sum Frequency Generation Spectroscopy. *Langmuir* **2006**, *22*, 5341-5349.

89.   Gan, W.; Zhang, Z.; Feng, R. R.; Wang, H. F., Spectral Interference and Molecular Conformation at Liquid Interface with Sum Frequency Generation Vibrational Spectroscopy (SFG-VS). *J. Phys. Chem. C* **2007**, *111*, 8726-8738.

90.   Hung, K. K.; Stege, U.; Hore, D. K., IR Absorption, Raman Scattering, and IR-Vis Sum-Frequency Generation Spectroscopy as Quantitative Probes of Surface Structure. *Appl. Spectrosc. Rev.* **2015**, *50*, 351-376.

91.   Ye, S. J.; Wei, F.; Li, H. C.; Tian, K. Z.; Luo, Y., Structure and Orientation of Interfacial Proteins Determined by Sum Frequency Generation Vibrational Spectroscopy: Method and Application. *Adv. Protein Chem. Struct. Biol.* **2013**, *93*, 213-255.

92.   Friedbacher, G.; Bubert, H., *Surface and Thin Film Analysis: A Compendium of Principles, Instrumentation and Applications, 2nd Ed.*; Weinheim: Wiley-VCH, 2011.

93.   Ji, N.; Ostroverkhov, V.; Tian, C. S.; Shen, Y. R., Characterization of Vibrational Resonances of Water-Vapor Interfaces by Phase-Sensitive Sum-Frequency Spectroscopy. *Phys. Rev. Lett.* **2008**, *100*, 096102.

94.   Shen, Y. R., Phase-Sensitive Sum-Frequency Spectroscopy. *Annu. Rev. Phys. Chem.* **2013**, *64*, 129-150.

95.   Mondal, J. A.; Nihonyanagi, S.; Yamaguchi, S.; Tahara, T., Structure and Orientation of Water at Charged Lipid Monolayer/Water Interfaces Probed by Heterodyne-Detected Vibrational Sum Frequency Generation Spectroscopy. *J. Am. Chem. Soc.* **2010**, *132*, 10656-10657.

96.   Nihonyanagi, S.; Mondal, J. A.; Yamaguchi, S.; Tahara, T., Structure and Dynamics of Interfacial Water Studied by Heterodyne-Detected Vibrational Sum-Frequency Generation. *Annu. Rev. Phys. Chem.* **2013**, *64*, 579-603.

97.   Mifflin, A. L.; Gerth, K. A.; Geiger, F. M., Kinetics of Chromate Adsorption and Desorption at Fused Quartz/Water Interfaces Studied by Second Harmonic Generation. *J. Phys. Chem. A* **2003**, *107*, 9620-9627.

98.   Malin, J. N.; Geiger, F. M., Uranyl Adsorption and Speciation at the Fused Silica/Water Interface Studied by Resonantly Enhanced Second Harmonic Generation and the $\chi^{(3)}$ Method. *J. Phys. Chem. A* **2010**, *114*, 1797-1805.

99.   Gibbs-Davis, J. M.; Hayes, P. L.; Scheidt, K. A.; Geiger, F. M., Anion Chelation by Amido Acid Functionalized Fused Quartz/Water Interfaces Studied by Nonlinear Optics. *J. Am. Chem. Soc.* **2007**, *129*, 7175-7184.

100.   Yan, E. C. Y.; Fu, L.; Wang, Z.; Liu, W., Biological Macromolecules at Interfaces Probed by Chiral Vibrational Sum Frequency Generation Spectroscopy. *Chem. Rev.* **2014**, *114*, 8471-8498.

101.   Somorjai, G. A.; Rupprechter, G., Molecular Studies of Catalytic Reactions on Crystal Surfaces at High Pressures and High Temperatures by Infrared-Visible Sum Frequency Generation (SFG) Surface Vibrational Spectroscopy. *J. Phys. Chem. B* **1999**, *103*, 1623-1638.

102.   Somorjai, G. A.; York, R. L.; Butcher, D.; Park, J. Y., The Evolution of Model Catalytic Systems: Studies of Structure, Bonding and Dynamics from Single Crystal Metal Surfaces to Nanoparticles, and from Low Pressure ($< 10^{-3}$ Torr) to High Pressure ($> 10^{-3}$ Torr) to Liquid Interfaces. *Phys. Chem. Chem. Phys.* **2007**, *9*, 3500-3513.

103.   Somorjai, G. A.; Park, J. Y., Molecular Surface Chemistry by Metal Single Crystals and Nanoparticles from Vacuum to High Pressure. *Chem. Soc. Rev.* **2008**, *37*, 2155-2162.

104.   Chou, K. C.; Markovic, N. M.; Kim, J.; Ross, P. N.; Somorjai, G. A., An in Situ Time-Dependent Study of CO Oxidation on Pt(111) in Aqueous Solution by Voltammetry and Sum Frequency Generation. *J. Phys. Chem. B* **2003**, *107*, 1840-1844.

105.   Hoffer, S.; Baldelli, S.; Chou, K.; Ross, P.; Somorjai, G. A., CO Oxidation on Electrified Platinum Surfaces in Acetonitrile/Water Solutions Studied by Sum Frequency Generation and Cyclic Voltammetry. *J. Phys. Chem. B* **2002**, *106*, 6473-6478.

106.   Kutz, R. B.; Braunschweig, B.; Mukherjee, P.; Dlott, D. D.; Wieckowski, A., Study of Ethanol Electrooxidation in Alkaline Electrolytes with Isotope Labels and Sum-Frequency Generation. *J. Phys. Chem. Lett.* **2011**, *2*, 2236-2240.

107.   Tong, Y.; Li, N.; Liu, H.; Ge, A.; Osawa, M.; Ye, S., Mechanistic Studies by Sum-Frequency Generation Spectroscopy: Hydrolysis of a Supported Phospholipid Bilayer by Phospholipase A$_2$. *Angew. Chem. Int. Ed.* **2010**, *49*, 2319-2323.

108.   Jordan, D. S.; Malin, J. N.; Geiger, F. M., Interactions of Al(III), La(III), Gd(III), and Lu(III) with the Fused Silica/Water Interface Studied by Second Harmonic Generation. *Environ. Sci. Technol.* **2010**, *44*, 5862-5867.

109.   Chen, E. H.; Geiger, F. M., Zinc Interaction with Glucosamine-Functionalized Fused Silica/Water Interfaces at pH 7 and 10 mM NaCl Studied by Second Harmonic and Vibrational Sum Frequency Generation. *Geochim. Cosmochim. Acta* **2010**, *74*, A167-A167.

110.   Chen, E. H.; Hayes, P. L.; Nguyen, S. T.; Geiger, F. M., Zinc Interactions with Glucosamine-Functionalized Fused Silica/Water Interfaces. *J. Phys. Chem. C* **2010**, *114*, 19483-19488.

111.   Malin, J. N.; Holland, J. G.; Geiger, F. M., Free Energy Relationships in the Electric Double Layer and Alkali Earth Speciation at the Fused Silica/Water Interface. *J. Phys. Chem. C* **2009**, *113*, 17795-17802.

112.   Malin, J. N.; Hayes, P. L.; Geiger, F. M., Interactions of Ca, Zn, and Cd Ions at Buried Solid/Water Interfaces Studied by Second Harmonic Generation. *J. Phys. Chem. C* **2009**, *113*, 2041-2052.

113.   Azam, M. S.; Weeraman, C. N.; Gibbs-Davis, J. M., Specific Cation Effects on the Bimodal Acid-Base Behavior of the Silica/Water Interface. *J. Phys. Chem. Lett.* **2012**, *3*, 1269-1274.

114.   Azam, M. S.; Darlington, A.; Gibbs-Davis, J. M., The Influence of Concentration on Specific Ion Effects at the Silica/Water Interface. *J. Phys. Condens. Matter* **2014**, *26*, 244107.

115.   Azam, M. S.; Weeraman, C. N.; Gibbs-Davis, J. M., Halide-Induced Cooperative Acid-Base Behavior at a Negatively Charged Interface. *J. Phys. Chem. C* **2013**, *117*, 8840-8850.

116.   Roke, S.; Gonella, G., Nonlinear Light Scattering and Spectroscopy of Particles and Droplets in Liquids. *Annu. Rev. Phys. Chem.* **2012**, *63*, 353-378.

117.   Gonella, G.; Dai, H. L., Second Harmonic Light Scattering from the Surface of Colloidal Objects: Theory and Applications. *Langmuir* **2014**, *30*, 2588-2599.

118.   Lis, D.; Backus, E. H. G.; Hunger, J.; Parekh, S. H.; Bonn, M., Liquid Flow Along a Solid Surface Reversibly Alters Interfacial Chemistry. *Science* **2014**, *344*, 1138-1142.

119.   Anglin, T. C.; Conboy, J. C., Kinetics and Thermodynamics of Flip-Flop in Binary Phospholipid Membranes Measured by Sum-Frequency Vibrational Spectroscopy. *Biochemistry* **2009**, *48*, 10220-10234.

120.   Anglin, T. C.; Cooper, M. P.; Li, H.; Chandler, K.; Conboy, J. C., Free Energy and Entropy of Activation for Phospholipid Flip-Flop in Planar Supported Lipid Bilayers. *J. Phys. Chem. B* **2010**, *114*, 1903-1914.

121.   Liu, J.; Conboy, J. C., Asymmetric Distribution of Lipids in a Phase Segregated Phospholipid Bilayer Observed by Sum-Frequency Vibrational Spectroscopy. *J. Phys. Chem. C* **2007**, *111*, 8988-8999.

122.   Chen, X.; Chen, Z., Sfg Studies on Interactions between Antimicrobial Peptides and Supported Lipid Bilayers. *BBA-Biomembranes* **2006**, *1758*, 1257-1273.

123.   Liu, Y.; Jasensky, J.; Chen, Z., Molecular Interactions of Proteins and Peptides at Interfaces Studied by Sum Frequency Generation Vibrational Spectroscopy. *Langmuir* **2012**, *28*, 2113-2121.

124.   Schaller, R. D.; Johnson, J. C.; Wilson, K. R.; Lee, L. F.; Haber, L. H.; Saykally, R. J., Nonlinear Chemical Imaging Nanomicroscopy: From Second and Third Harmonic Generation to Multiplex (Broad-Bandwidth) Sum Frequency Generation Near-Field Scanning Optical Microscopy. *J. Phys. Chem. B* **2002**, *106*, 5143-5154.

125.   Clark, J. H., Green Chemistry: Today (and Tomorrow). *Green Chem.* **2006**, *8*, 17-21.

126.   Corma, A.; Garcia, H., Lewis Acids: From Conventional Homogeneous to Green Homogeneous and Heterogeneous Catalysis. *Chem. Rev.* **2003**, *103*, 4307-4365.

127.   Cozzi, F., Immobilization of Organic Catalysts: When, Why, and How. *Adv. Synth. Catal.* **2006**, *348*, 1367-1390.

128.   Baleizao, C.; Garcia, H., Chiral Salen Complexes: An Overview to Recoverable and Reusable Homogeneous and Heterogeneous Catalysts. *Chem. Rev.* **2006**, *106*, 3987-4043.

129.   Kim, J.-H.; Kim, G.-J., Enantioselectivities of Chiral Ti(IV) Salen Complexes Immobilized on MCM-41 in Asymmetric Trimethylsilylcyanation of Benzaldehyde. *Catal. Lett.* **2004**, *92*, 123-130.

130.   MacMillan, D. W. C., The Advent and Development of Organocatalysis. *Nature* **2008**, *455*, 304-308.

131.   Bertelsen, S.; Jorgensen, K. A., Organocatalysis - after the Gold Rush. *Chem. Soc. Rev.* **2009**, *38*, 2178-2189.

132.   Dalko, P. I.; Moisan, L., Enantioselective Organocatalysis. *Angew. Chem. Int. Ed.* **2001**, *40*, 3726-3748.

133.   Dalko, P. I.; Moisan, L., In the Golden Age of Organocatalysis. *Angew. Chem. Int. Ed.* **2004**, *43*, 5138-5175.

134.   Pellissier, H., Asymmetric Organocatalysis. *Tetrahedron* **2007**, *63*, 9267-9331.

135.   Kristensen, T. E.; Hansen, T., Polymer-Supported Chiral Organocatalysts: Synthetic Strategies for the Road Towards Affordable Polymeric Immobilization. *Eur. J. Org. Chem.* **2010**, 3179-3204.

136.   Mrowczynski, R.; Nan, A.; Liebscher, J., Magnetic Nanoparticle-Supported Organocatalysts - an Efficient Way of Recycling and Reuse. *RSC Adv.* **2014**, *4*, 5927-5952.

137.   Connon, S. J., The Design of Novel, Synthetically Useful (Thio)Urea-Based Organocatalysts. *Synlett* **2009**, 354-376.

138.   Pihko, P. M., Activation of Carbonyl Compounds by Double Hydrogen Bonding: An Emerging Tool in Asymmetric Catalysis. *Angew. Chem. Int. Ed.* **2004**, *43*, 2062-2064.

139.   Chen, H.-T.; Trewyn, B. G.; Wiench, J. W.; Pruski, M.; Lin, V. S. Y., Urea and Thiourea-Functionalized Mesoporous Silica Nanoparticle Catalysts with Enhanced Catalytic Activity for Diels-Alder Reaction. *Top. Catal.* **2010**, *53*, 187-191.

140.   Huh, S.; Chen, H. T.; Wiench, J. W.; Pruski, M.; Lin, V. S. Y., Cooperative Catalysis by General Acid and Base Bifunctionalized Mesoporous Silica Nanospheres. *Angew. Chem. Int. Ed.* **2005**, *44*, 1826-1830.

141.   Azam, M. S.; Fenwick, S. L.; Gibbs-Davis, J. M., Orthogonally Reactive SAMs as a General Platform for Bifunctional Silica Surfaces. *Langmuir* **2011**, *27*, 741-750.

142.   Ding, F.; Hu, Z.; Zhong, Q.; Manfred, K.; Gattass, R. R.; Brindza, M. R.; Fourkas, J. T.; Walker, R. A.; Weeks, J. D., Interfacial Organization of Acetonitrile: Simulation and Experiment. *J. Phys. Chem. C* **2010**, *114*, 17651-17659.

143.   Mifflin, A. L.; Musorrafiti, M. J.; Konek, C. T.; Geiger, F. M., Second Harmonic Generation Phase Measurements of Cr(VI) at a Buried Interface. *J. Phys. Chem. B* **2005**, *109*, 24386-24390.

144.   Wang, H. F.; Yan, E. C. Y.; Liu, Y.; Eisenthal, K. B., Energetics and Population of Molecules at Microscopic Liquid and Solid Surfaces. *J. Phys. Chem. B* **1998**, *102*, 4446-4450.

145.   List, B., Enamine Catalysis Is a Powerful Strategy for the Catalytic Generation and Use of Carbanion Equivalents. *Acc. Chem. Res.* **2004**, *37*, 548-557.

146.   Sorrell, T. N., *Organic Chemistry, 2nd Ed.*; University Science Books: Sausalito, Calif., 2006.

147.   Bass, J. D.; Solovyov, A.; Pascall, A. J.; Katz, A., Acid-Base Bifunctional and Dielectric Outer-Sphere Effects in Heterogeneous Catalysis: A Comparative Investigation of Model Primary Amine Catalysts. *J. Am. Chem. Soc.* **2006**, *128*, 3737-3747.

148.   Sharma, K. K.; Asefa, T., Efficient Bifunctional Nanocatalysts by Simple Postgrafting of Spatially Isolated Catalytic Groups on Mesoporous Materials. *Angew. Chem. Int. Ed.* **2007**, *46*, 2879-2882.

149.   Baitinger, W. F.; Robinson, L.; Schleyer, P. V.; Murty, T. S. S., Nitro Groups as Proton Acceptors in Hydrogen Bonding. *Tetrahedron* **1964**, *20*, 1635-1647.

150.   Gilli, P.; Pretto, L.; Bertolasi, V.; Gilli, G., Predicting Hydrogen-Bond Strengths from Acid-Base Molecular Properties. The pK$_a$ Slide Rule: Toward the Solution of a Long-Lasting Problem. *Acc. Chem. Res.* **2009**, *42*, 33-44.

151.   Johnstone, R. A. W.; Loureiro, R. M. S.; Cristiano, M. L. S.; Labat, G., Bond Energy/Bond Order Relationships for N-O Linkages and a Quantitative Measure of Ionicity: The Role of Nitro Groups in Hydrogen-Bonding. *ARKIVOC* **2010**, 142-169.

152.   Chang, Y. L.; West, M. A.; Fowler, F. W.; Lauher, J. W., An Approach to the Design of Molecular Solids. Strategies for Controlling the Assembly of Molecules into Two-Dimensional Layered Structures. *J. Am. Chem. Soc.* **1993**, *115*, 5991-6000.

153.   Zhao, X.; Chang, Y.; Fowler, F. W.; Lauher, J. W., An Approach to the Design of Molecular Solids. The Ureylenedicarboxylic Acids. *J. Am. Chem. Soc.* **1990**, *112*, 6627-6634.

154.   Jadzyn, J.; Stockhausen, M.; Zywucki, B., Structure of Hydrogen-Bonded Sym-Dialkylureas in Nonpolar Organic Media. *J. Phys. Chem.* **1987**, *91*, 754-757.

155.   Simpson, G. J.; Rowlen, K. L., An Shg Magic Angle: Dependence of Second Harmonic Generation Orientation Measurements on the Width of the Orientation Distribution. *J. Am. Chem. Soc.* **1999**, *121*, 2635-2636.

156.   Du, Q.; Freysz, E.; Shen, Y. R., Vibrational Spectra of Water Molecules at Quartz/Water Interfaces. *Phys. Rev. Lett.* **1994**, *72*, 238-241.

157.   Hopkins, A. J.; McFearin, C. L.; Richmond, G. L., Investigations of the Solid-Aqueous Interface with Vibrational Sum-Frequency Spectroscopy. *Curr. Opin. Solid State Mater. Sci.* **2005**, *9*, 19-27.

158. Piasek, Z.; Urbanski, T., The Infrared Absorption Spectrum and Structure of Urea. *Bull. Acad. Polon. Sci., Ser. Sci. Chim.* **1962**, *10*, 113-120.

159. Xu, M.; Liu, D. F.; Allen, H. C., Ethylenediamine at Air/Liquid and Air/Silica Interfaces: Protonation Versus Hydrogen Bonding Investigated by Sum Frequency Generation Spectroscopy. *Environ. Sci. Technol.* **2006**, *40*, 1566-1572.

160. Beaucage, S. L., Strategies in the Preparation of DNA Oligonucleotide Arrays for Diagnostic Applications. *Curr. Med. Chem.* **2001**, *8*, 1213-1244.

161. Samanta, D.; Sarkar, A., Immobilization of Bio-Macromolecules on Self-Assembled Monolayers: Methods and Sensor Applications. *Chem. Soc. Rev.* **2011**, *40*, 2567-2592.

162. Azam, M. S.; Gibbs-Davis, J. M., Monitoring DNA Hybridization and Thermal Dissociation at the Silica/Water Interface Using Resonantly Enhanced Second Harmonic Generation Spectroscopy. *Anal. Chem.* **2013**, *85*, 8031-8038.

163. Miranda, P. B.; Shen, Y. R., Liquid Interfaces: A Study by Sum-Frequency Vibrational Spectroscopy. *J. Phys. Chem. B* **1999**, *103*, 3292-3307.

164. Stokes, G. Y.; Buchbinder, A. M.; Gibbs-Davis, J. M.; Scheidt, K. A.; Geiger, F. M., Heterogeneous Ozone Oxidation Reactions of 1-Pentene, Cyclopentene, Cyclohexene, and a Menthenol Derivative Studied by Sum Frequency Generation. *J. Phys. Chem. A* **2008**, *112*, 11688-11698.

165. Rostovtsev, V. V.; Green, L. G.; Fokin, V. V.; Sharpless, K. B., A Stepwise Huisgen Cycloaddition Process: Copper(I)-Catalyzed Regioselective "Ligation" of Azides and Terminal Alkynes. *Angew. Chem. Int. Ed.* **2002**, *41*, 2596-2599.

166.   Tornoe, C. W.; Christensen, C.; Meldal, M., Peptidotriazoles on Solid Phase: 1,2,3-Triazoles by Regiospecific Copper(I)-Catalyzed 1,3-Dipolar Cycloadditions of Terminal Alkynes to Azides. *J. Org. Chem.* **2002**, *67*, 3057-3064.

167.   Fournier, D.; Hoogenboom, R.; Schubert, U. S., Clicking Polymers: A Straightforward Approach to Novel Macromolecular Architectures. *Chem. Soc. Rev.* **2007**, *36*, 1369-1380.

168.   Gramlich, P. M. E.; Wirges, C. T.; Manetto, A.; Carell, T., Postsynthetic DNA Modification through the Copper-Catalyzed Azide-Alkyne Cycloaddition Reaction. *Angew. Chem. Int. Ed.* **2008**, *47*, 8350-8358.

169.   Winz, M. L.; Samanta, A.; Benzinger, D.; Jaschke, A., Site-Specific Terminal and Internal Labeling of RNA by Poly(A) Polymerase Tailing and Copper-Catalyzed or Copper-Free Strain-Promoted Click Chemistry. *Nucleic Acids Res.* **2012**, *40*, e78.

170.   Lin, P. C.; Ueng, S. H.; Yu, S. C.; Jan, M. D.; Adak, A. K.; Yu, C. C.; Lin, C. C., Surface Modification of Magnetic Nanoparticle Via Cu(I)-Catalyzed Alkyne-Azide [2+3] Cycloaddition. *Org. Lett.* **2007**, *9*, 2131-2134.

171.   Thode, C. J.; Williams, M. E., Kinetics of 1,3-Dipolar Cycloaddition on the Surfaces of Au Nanoparticles. *J. Colloid Interface Sci.* **2008**, *320*, 346-352.

172.   Ciampi, S.; Bocking, T.; Kilian, K. A.; Harper, J. B.; Gooding, J. J., Click Chemistry in Mesoporous Materials: Functionalization of Porous Silicon Rugate Filters. *Langmuir* **2008**, *24*, 5888-5892.

173.   Chen, E. H.; Walter, S. R.; Nguyen, S. T.; Geiger, F. M., Arylsilanated SiO_x Surfaces for Mild and Simple Two-Step Click Functionalization with Small Molecules and Oligonucleotides. *J. Phys. Chem. C* **2012**, *116*, 19886-19892.

174.   Lummerstorfer, T.; Hoffmann, H., Click Chemistry on Surfaces: 1,3-Dipolar Cycloaddition Reactions of Azide-Terminated Monolayers on Silica. *J. Phys. Chem. B* **2004**, *108*, 3963-3966.

175.   Devaraj, N. K.; Collman, J. P., Copper Catalyzed Azide-Alkyne Cycloadditions on Solid Surfaces: Applications and Future Directions. *QSAR Comb. Sci.* **2007**, *26*, 1253-1260.

176.   Devaraj, N. K.; Miller, G. P.; Ebina, W.; Kakaradov, B.; Collman, J. P.; Kool, E. T.; Chidsey, C. E. D., Chemoselective Covalent Coupling of Oligonucleotide Probes to Self-Assembled Monolayers. *J. Am. Chem. Soc.* **2005**, *127*, 8600-8601.

177.   Hein, J. E.; Fokin, V. V., Copper-Catalyzed Azide-Alkyne Cycloaddition (CuAAC) and Beyond: New Reactivity of Copper(I) Acetylides. *Chem. Soc. Rev.* **2010**, *39*, 1302-1315.

178.   Hein, J. E.; Tripp, J. C.; Krasnova, L. B.; Sharpless, K. B.; Fokin, V. V., Copper(I)-Catalyzed Cycloaddition of Organic Azides and 1-Iodoalkynes. *Angew. Chem. Int. Ed.* **2009**, *48*, 8018-8021.

179.   Himo, F.; Lovell, T.; Hilgraf, R.; Rostovtsev, V. V.; Noodleman, L.; Sharpless, K. B.; Fokin, V. V., Copper(I)-Catalyzed Synthesis of Azoles. DFT Study Predicts Unprecedented Reactivity and Intermediates. *J. Am. Chem. Soc.* **2005**, *127*, 210-216.

180.   Kuang, G.-C.; Guha, P. M.; Brotherton, W. S.; Simmons, J. T.; Stankee, L. A.; Nguyen, B. T.; Clark, R. J.; Zhu, L., Experimental Investigation on the Mechanism of Chelation-Assisted, Copper(II) Acetate-Accelerated Azide-Alkyne Cycloaddition. *J. Am. Chem. Soc.* **2011**, *133*, 13984-14001.

181.   Rodionov, V. O.; Fokin, V. V.; Finn, M. G., Mechanism of the Ligand-Free Cu(I)-Catalyzed Azide-Alkyne Cycloaddition Reaction. *Angew. Chem. Int. Ed.* **2005**, *44*, 2210-2215.

182.	Rodionov, V. O.; Presolski, S. I.; Diaz, D. D.; Fokin, V. V.; Finn, M. G., Ligand-Accelerated Cu-Catalyzed Azide-Alkyne Cycloaddition: A Mechanistic Report. *J. Am. Chem. Soc.* **2007**, *129*, 12705-12712.

183.	Worrell, B. T.; Malik, J. A.; Fokin, V. V., Direct Evidence of a Dinuclear Copper Intermediate in Cu(I)-Catalyzed Azide-Alkyne Cycloadditions. *Science* **2013**, *340*, 457-460.

184.	Lewis, W. G.; Magallon, F. G.; Fokin, V. V.; Finn, M. G., Discovery and Characterization of Catalysts for Azide-Alkyne Cycloaddition by Fluorescence Quenching. *J. Am. Chem. Soc.* **2004**, *126*, 9152-9153.

185.	Zhang, S.; Koberstem, J. T., Azide Functional Monolayers Grafted to a Germanium Surface: Model Substrates for ATR-IR Studies of Interfacial Click Reactions. *Langmuir* **2012**, *28*, 486-493.

186.	Collman, J. P.; Devaraj, N. K.; Eberspacher, T. P. A.; Chidsey, C. E. D., Mixed Azide-Terminated Monolayers: A Platform for Modifying Electrode Surfaces. *Langmuir* **2006**, *22*, 2457-2464.

187.	Rusen, E.; Marculescu, B.; Butac, L.; Preda, N.; Mihut, L., The Synthesis and Characterization of Poly Vinyl Chloride Chemically Modified with C_{60}. *Fuller. Nanotub. Car. N.* **2008**, *16*, 178-185.

188.	Palla, M.; Guo, W.; Shi, S.; Li, Z.; Wu, J.; Jockusch, S.; Guo, C.; Russo, J. J.; Turro, N. J.; Ju, J., DNA Sequencing by Synthesis Using 3'-O-Azidomethyl Nucleotide Reversible Terminators and Surface-Enhanced Raman Spectroscopic Detection. *RSC Adv.* **2014**, *4*, 49342-49346.

189.   Padermshoke, A.; Konishi, S.; Ara, M.; Tada, H.; Ishibashi, T. A., Novel SiO_2-Deposited CaF_2 Substrate for Vibrational Sum-Frequency Generation (SFG) Measurements of Chemisorbed Mono Layers in an Aqueous Environment. *Appl. Spectrosc.* **2012**, *66*, 711-718.

190.   Eftekhari-Bafrooei, A.; Nihonyanagi, S.; Borguet, E., Spectroscopy and Dynamics of the Multiple Free OH Species at an Aqueous/Hydrophobic Interface. *J. Phys. Chem. C* **2012**, *116*, 21734-21741.

191.   Nihonyanagi, S.; Eftekhari-Bafrooei, A.; Borguet, E., Ultrafast Vibrational Dynamics and Spectroscopy of a Siloxane Self-Assembled Monolayer. *J. Chem. Phys.* **2011**, *134*, 084701.

192.   Schei, S. H.; Priebe, H.; Nielsen, C. J.; Klaeboe, P., The Vibrational Spectra, Molecular Structure and Conformation of Organic Azides. 2. 2-Azido-1,3-Butadiene. *J. Mol. Struct.* **1986**, *147*, 203-215.

193.   Waldrup, S. B.; Williams, C. T., In Situ Investigation of Acetonitrile Adsorption on Al_2O_3-Coated CaF_2 Using Sum-Frequency Spectroscopy. *J. Phys. Chem. B* **2006**, *110*, 16633-16639.

194.   Soule, M. C. K.; Hore, D. K.; Jaramillo-Fellin, D. M.; Richmond, G. L., Differing Adsorption Behavior of Environmentally Important Cyanophenol Isomers at the Air-Water Interface. *J. Phys. Chem. B* **2006**, *110*, 16575-16583.

195.   Zhuang, X.; Miranda, P. B.; Kim, D.; Shen, Y. R., Mapping Molecular Orientation and Conformation at Interfaces by Surface Nonlinear Optics. *Phys. Rev. B* **1999**, *59*, 12632-12640.

196.   Stiopkin, I. V.; Jayathilake, H. D.; Weeraman, C.; Benderskii, A. V., Temporal Effects on Spectroscopic Line Shapes, Resolution, and Sensitivity of the Broad-Band Sum Frequency Generation. *J. Chem. Phys.* **2010**, *132*, 234503.

197.   Anand, G. S.; Gopalan, A. I.; Kang, S. W.; Lee, K. P., Development of a Surface Plasmon Assisted Label-Free Calorimetric Method for Sensitive Detection of Mercury Based on Functionalized Gold Nanorods. *J. Anal. At. Spectrom.* **2013**, *28*, 488-498.

198.   Kifle, D.; Wibetoe, G., Retention and Elution of Precious Metals on Cyano-Modified Solid Phase Microparticle Sorbent. *Microchim. Acta* **2013**, *180*, 981-987.

199.   Li, Y. R.; Ashizawa, M.; Uchida, S.; Michinobu, T., A Novel Polymeric Chemosensor: Dual Colorimetric Detection of Metal Ions through Click Synthesis. *Macromol. Rapid Commun.* **2011**, *32*, 1804-1808.

200.   Li, Y. R.; Ashizawa, M.; Uchida, S.; Michinobu, T., Colorimetric Sensing of Cations and Anions by Clicked Polystyrenes Bearing Side Chain Donor-Acceptor Chromophores. *Polym. Chem.* **2012**, *3*, 1996-2005.

201.   Li, Y. R.; Michinobu, T., Multi-Coloration of Polyurethane Derivatives through Click Postfunctionalization, Electrochemical Oxidation, and Ag^+ Ion Complexation. *J. Mater. Chem.* **2012**, *22*, 9513-9521.

202.   Michinobu, T.; Li, Y. R.; Hyakutake, T., Polymeric Ion Sensors with Multiple Detection Modes Achieved by a New Type of Click Chemistry Reaction. *Phys. Chem. Chem. Phys.* **2013**, *15*, 2623-2631.

203.   Philips, M. F.; Gopalan, A. I.; Lee, K. P., Development of a Novel Cyano Group Containing Electrochemically Deposited Polymer Film for Ultrasensitive Simultaneous Detection of Trace Level Cadmium and Lead. *J. Hazard. Mater.* **2012**, *237*, 46-54.

204.   Kwon, Y.; Mrksich, M., Dependence of the Rate of an Interfacial Diels-Alder Reaction on the Steric Environment of the Immobilized Dienophile: An Example of Enthalpy-Entropy Compensation. *J. Am. Chem. Soc.* **2002**, *124*, 806-812.

205.   Zhang, D.; Gutow, J.; Eisenthal, K. B., Vibrational Spectra, Orientations, and Phase Transitions in Long-Chain Amphiphiles at the Air/Water Interface: Probing the Head and Tail Groups by Sum Frequency Generation. *J. Phys. Chem.* **1994**, *98*, 13729-13734.

206.   Zhang, Z.; Guo, Y.; Lu, Z.; Velarde, L.; Wang, H. F., Resolving Two Closely Overlapping -CN Vibrations and Structure in the Langmuir Mono Layer of the Long-Chain Nonadecanenitrile by Polarization Sum Frequency Generation Vibrational Spectroscopy. *J. Phys. Chem. C* **2012**, *116*, 2976-2987.

207.   Guo, Z.; Guilfoyle, R. A.; Thiel, A. J.; Wang, R.; Smith, L. M., Direct Fluorescence Analysis of Genetic Polymorphisms by Hybridization with Oligonucleotide Arrays on Glass Supports. *Nucleic Acids Res.* **1994**, *22*, 5456-5465.

208.   Heise, C.; Bier, F. F., Immobilization of DNA on Microarrays. *Top. Curr. Chem.* **2006**, *261*, 1-25.

209.   Miller, M. B.; Tang, Y.-W., Basic Concepts of Microarrays and Potential Applications in Clinical Microbiology. *Clin. Microbiol. Rev.* **2009**, *22*, 611-633.

210.   Ge, D.; Wang, X.; Williams, K.; Levicky, R., Thermostable DNA Immobilization and Temperature Effects on Surface Hybridization. *Langmuir* **2012**, *28*, 8446-8455.

211.   Levicky, R.; Horgan, A., Physicochemical Perspectives on DNA Microarray and Biosensor Technologies. *Trends Biotechnol.* **2005**, *23*, 143-149.

212.   Pozhitkov, A. E.; Tautz, D.; Noble, P. A., Oligonucleotide Microarrays: Widely Applied-Poorly Understood. *Brief. Funct. Genomics Proteomics* **2007**, *6*, 141-148.

213.   Wu, P.; Castner, D. G.; Grainger, D. W., Diagnostic Devices as Biomaterials: A Review of Nucleic Acid and Protein Microarray Surface Performance Issues. *J. Biomater. Sci., Polym. Ed.* **2008**, *19*, 725-753.

214.   Poulsen, L.; Søe, M. J.; Snakenborg, D.; Møller, L. B.; Dufva, M., Multi-Stringency Wash of Partially Hybridized 60-mer Probes Reveals That the Stringency Along the Probe Decreases with Distance from the Microarray Surface. *Nucleic Acids Res.* **2008**, *36*, e132.

215.   Chen, Q. B.; Kang, X. L.; Li, R.; Du, X. Z.; Shang, Y. Z.; Liu, H. L.; Hu, Y., Structure of the Complex Monolayer of Gemini Surfactant and DNA at the Air/Water Interface. *Langmuir* **2012**, *28*, 3429-3438.

216.   Hirano-Iwata, A.; Yamaguchi, R.-t.; Miyamoto, K.-i.; Kimura, Y.; Niwano, M., In Situ Real-Time Monitoring of Biomolecular Interactions by Using Surface Infrared Spectroscopy. *J. Appl. Phys.* **2009**, *105*, 102039.

217.   Walter, S. R.; Geiger, F. M., DNA on Stage: Showcasing Oligonucleotides at Surfaces and Interfaces with Second Harmonic and Vibrational Sum Frequency Generation. *J. Phys. Chem. Lett.* **2010**, *1*, 9-15.

218.   Campen, R. K.; Ngo, T. T. M.; Sovago, M.; Ruysschaert, J. M.; Bonn, M., Molecular Restructuring of Water and Lipids upon the Interaction of DNA with Lipid Monolayers. *J. Am. Chem. Soc.* **2010**, *132*, 8037-8047.

219.   Wurpel, G. W. H.; Sovago, M.; Bonn, M., Sensitive Probing of DNA Binding to a Cationic Lipid Monolayer. *J. Am. Chem. Soc.* **2007**, *129*, 8420-8421.

220.   Boman, F. C.; Gibbs-Davis, J. M.; Heckman, L. M.; Stepp, B. R.; Nguyen, S. T.; Geiger, F. M., DNA at Aqueous/Solid Interfaces: Chirality-Based Detection via Second Harmonic Generation Activity. *J. Am. Chem. Soc.* **2009**, *131*, 844-848.

221.   Boman, F. C.; Musorrafiti, M. J.; Gibbs, J. M.; Stepp, B. R.; Salazar, A. M.; Nguyen, S. B. T.; Geiger, F. M., DNA Single Strands Tethered to Fused Quartz/Water Interfaces Studied by Second Harmonic Generation. *J. Am. Chem. Soc.* **2005**, *127*, 15368-15369.

222.   Holland, J. G.; Geiger, F. M., Importance of Length and Sequence Order on Magnesium Binding to Surface-Bound Oligonucleotides Studied by Second Harmonic Generation and Atomic Force Microscopy. *J. Phys. Chem. B* **2012**, *116*, 6302-6310.

223.   Holland, J. G.; Geiger, F. M., Y(III) Interactions with Guanine Oligonucleotides Covalently Attached to Aqueous/Solid Interfaces. *J. Phys. Chem. B* **2013**, *117*, 825-832.

224.   Holland, J. G.; Jordan, D. S.; Geiger, F. M., Divalent Metal Cation Speciation and Binding to Surface-Bound Oligonucleotide Single Strands Studied by Second Harmonic Generation. *J. Phys. Chem. B* **2011**, *115*, 8338-8345.

225.   Holland, J. G.; Malin, J. N.; Jordan, D. S.; Geiger, F. M., Specific and Nonspecific Metal Ion-Nucleotide Interactions at Aqueous/Solid Interfaces Functionalized with Adenine, Thymine, Guanine, and Cytosine Oligomers. *J. Am. Chem. Soc.* **2011**, *133*, 2567-2570.

226.   Walter, S. R.; Young, K. L.; Holland, J. G.; Gieseck, R. L.; Mirkin, C. A.; Geiger, F. M., Counting the Number of Magnesium Ions Bound to the Surface-Immobilized Thymine Oligonucleotides That Comprise Spherical Nucleic Acids. *J. Am. Chem. Soc.* **2013**, *135*, 17339-17348.

227.   Doughty, B.; Rao, Y.; Kazer, S. W.; Kwok, S. J. J.; Turro, N. J.; Eisenthal, K. B., Binding of the Anti-Cancer Drug Daunomycin to DNA Probed by Second Harmonic Generation. *J. Phys. Chem. B* **2013**, *117*, 15285-15289.

228.   Asanuma, H.; Noguchi, H.; Uosaki, K.; Yu, H.-Z., Metal Cation-Induced Deformation of DNA Self-Assembled Monolayers on Silicon: Vibrational Sum Frequency Generation Spectroscopy. *J. Am. Chem. Soc.* **2008**, *130,* 8016-8022.

229.   Stokes, G. Y.; Gibbs-Davis, J. M.; Boman, F. C.; Stepp, B. R.; Condie, A. G.; Nguyen, S. T.; Geiger, F. M., Making "Sense" of DNA. *J. Am. Chem. Soc.* **2007**, *129*, 7492-7493.

230.   Howell, C.; Schmidt, R.; Kurz, V.; Koelsch, P., Sum-Frequency-Generation Spectroscopy of DNA Films in Air and Aqueous Environments. *Biointerphases* **2008**, *3*, FC47.

231.   Howell, C.; Zhao, J. L.; Koelsch, P.; Zharnikov, M., Hybridization in ssDNA Films-a Multi-Technique Spectroscopy Study. *Phys. Chem. Chem. Phys.* **2011**, *13*, 15512-15522.

232.   Qing, G.; Xiong, H.; Seela, F.; Sun, T., Spatially Controlled DNA Nanopatterns by "Click" Chemistry Using Oligonucleotides with Different Anchoring Sites. *J. Am. Chem. Soc.* **2010**, *132*, 15228-15232.

233.   Wampler, R. D.; Moad, A. J.; Moad, C. W.; Heiland, R.; Simpson, G. J., Visual Methods for Interpreting Optical Nonlinearity at the Molecular Level. *Acc. Chem. Res.* **2007**, *40*, 953-960.

234.   Richter, L. J.; Petralli-Mallow, T. P.; Stephenson, J. C., Vibrationally Resolved Sum-Frequency Generation with Broad-Bandwidth Infrared Pulses. *Opt. Lett.* **1998**, *23*, 1594-1596.

235.   van der Ham, E. W. M.; Vrehen, Q. H. F.; Eliel, E. R., Self-Dispersive Sum-Frequency Generation at Interfaces. *Opt. Lett.* **1996**, *21*, 1448-1450.

236.   Erickson, D.; Li, D.; Krull, U. J., Modeling of DNA Hybridization Kinetics for Spatially Resolved Biochips. *Anal. Biochem.* **2003**, *317*, 186-200.

237.   Tyrode, E.; Hedberg, J., A Comparative Study of the CD and CH Stretching Spectral Regions of Typical Surfactants Systems Using VSFS: Orientation Analysis of the Terminal CH_3 and CD_3 Groups. *J. Phys. Chem. C* **2011**, *116*, 1080-1091.

238.   Miranda, P. B.; Xu, L.; Shen, Y. R.; Salmeron, M., Icelike Water Monolayer Adsorbed on Mica at Room Temperature. *Phys. Rev. Lett.* **1998**, *81*, 5876-5879.

239.   Jena, K. C.; Hore, D. K., Variation of Ionic Strength Reveals the Interfacial Water Structure at a Charged Mineral Surface. *J. Phys. Chem. C* **2009**, *113*, 15364-15372.

240.   Li, Z.; Weeraman, C. N.; Gibbs-Davis, J. M., Following the Azide-Alkyne Cycloaddition at the Silica/Solvent Interface with Sum Frequency Generation. *ChemPhysChem* **2014**, *15*, 2247-2251.

241.   Colarusso, P.; Zhang, K.; Guo, B.; Bernath, P. F., The Infrared Spectra of Uracil, Thymine, and Adenine in the Gas Phase. *Chem. Phys. Lett.* **1997**, *269*, 39-48.

242.   Graindourze, M.; Smets, J.; Zeegers-Huyskens, T.; Maes, G., Fourier Transform-Infrared Spectroscopic Study of Uracil Derivatives and Their Hydrogen Bonded Complexes with Proton Donors: Part I. Monomer Infrared Absorptions of Uracil and Some Methylated Uracils in Argon Matrices. *J. Mol. Struct.* **1990**, *222*, 345-364.

243.   Mathlouthi, M.; Seuvre, A.-M.; L. Koenig, J., F.T.-I.R. And Laser-Raman Spectra of Thymine and Thymidine. *Carbohydr. Res.* **1984**, *134*, 23-38.

244.   Szczepaniak, K.; Szczesniak, M. M.; Person, W. B., Raman and Infrared Spectra of Thymine. A Matrix Isolation and Dft Study. *J. Phys. Chem. A* **2000**, *104*, 3852-3863.

245.   Zhang, S. L.; Michaelian, K. H.; Loppnow, G. R., Vibrational Spectra and Experimental Assignments of Thymine and Nine of Its Isotopomers. *J. Phys. Chem. A* **1998**, *102*, 461-470.

246.   Mathlouthi, M.; Seuvre, A. M.; Koenig, J. L., F.T.-I.R. And Laser-Raman Spectra of D-Ribose and 2-Deoxy-D-*Erythro*-Pentose ("2-Deoxy-D-Ribose"). *Carbohydr. Res.* **1983**, *122*, 31-47.

247.   Marky, L. A.; Breslauer, K. J., Calculating Thermodynamic Data for Transitions of Any Molecularity from Equilibrium Melting Curves. *Biopolymers* **1987**, *26*, 1601-1620.

248.   Vainrub, A.; Deluge, N.; Zhang, X.; Zhou, X.; Gao, X., Predicting DNA Duplex Stability on Oligonucleotide Arrays. *Methods Mol. Biol.* **2007**, *382*, 393-403.

249.   Backus, E. H. G.; Abrakhi, S.; Péralta, S.; Teyssié, D.; Fichet, O.; Cantin, S., Sum-Frequency Generation Spectroscopy of Cinnamate Modified Cellulosic Polymer at the Air-Water Interface. *J. Phys. Chem. B* **2012**, *116*, 6041-6049.

250.   Rivera, C. A.; Bender, J. S.; Manfred, K.; Fourkas, J. T., Persistence of Acetonitrile Bilayers at the Interface of Acetonitrile/Water Mixtures with Silica. *J. Phys. Chem. A* **2013**, *117*, 12060-12066.

251.   Amiri, A. A.; Hemmateenejad, B.; Safavi, A.; Sharghi, H.; Beni, A. R. S.; Shamsipur, M., Structure-Retention and Mobile Phase-Retention Relationships for Reversed-Phase High-Performance Liquid Chromatography of Several Hydroxythioxanthone Derivatives in Binary Acetonitrile-Water Mixtures. *Anal. Chim. Acta* **2007**, *605*, 11-19.

252.   Barbosa, J.; SanzNebot, V.; Toro, I., Solvatochromic Parameter Values and pH in Acetonitrile-Water Mixtures. Optimization of Mobile Phase for the Separation of Peptides by High-Performance Liquid Chromatography. *J. Chromatogr. A* **1996**, *725*, 249-260.

253.   Emel′yanova, N. S.; Kurbatova, S. V.; Saifutdinov, B. R.; Yudashkin, A. V., Regularities of the Sorption of Cycloalkenyl-Substituted Thiophenes and 2,2′-Bithiophenes from Water-Acetonitrile Solutions on Hexadecyl Silica Gel under Conditions of High-Performance Liquid Chromatography. *Russ. J. Phys. Chem. A* **2011**, *85*, 1440-1449.

254.   Guillaume, Y.; Cavalli, E. J.; Peyrin, E.; Guinchard, C., A New Approach to Study Benzodiazepine Separation and the Differences between a Methanol/Water and Acetonitrile/Water Mixture on Column Efficiency in Liquid Chromatography. *J. Liq. Chromatogr. R. T.* **1997**, *20*, 1741-1756.

255.   Hemmateenejad, B.; Shamsipur, M.; Safavi, A.; Sharghi, H.; Amiri, A. A., Reversed-Phase High Performance Liquid Chromatography (RP-HPLC) Characteristics of Some 9,10-

Anthraquinone Derivatives Using Binary Acetonitrile-Water Mixtures as Mobile Phase. *Talanta* **2008**, *77*, 351-359.

256.   Kukusamude, C.; Burakham, R.; Chailapakul, O.; Srijaranai, S., High Performance Liquid Chromatography for the Simultaneous Analysis of Penicillin Residues in Beef and Milk Using Ion-Paired Extraction and Binary Water-Acetonitrile Mixture. *Talanta* **2012**, *92*, 38-44.

257.   Saifutdinov, B. R.; Emel'yanova, N. S.; Kurbatova, S. V.; Pimerzin, A. A., The Adsorption of Hetero- and Alicyclic Thiophene Derivatives from Water-Acetonitrile Solutions on the Surface of Porous Graphitic Carbon under High-Performance Liquid Chromatography Conditions. *Russ. J. Phys. Chem. A* **2012**, *86*, 1152-1160.

258.   Subirats, X.; Bosch, E.; Roses, M., Retention of Ionisable Compounds on High-Performance Liquid Chromatography XVI. Estimation of Retention with Acetonitrile/Water Mobile Phases from Aqueous Buffer pH and Analyte pK_a. *J. Chromatogr. A* **2006**, *1121*, 170-177.

259.   Cheng, L.; Morrone, J. A.; Berne, B. J., Structure and Dynamics of Acetonitrile Confined in a Silica Nanopore. *J. Phys. Chem. C* **2012**, *116*, 9582-9593.

260.   Gulmen, T. S.; Thompson, W. H., Grand Canonical Monte Carlo Simulations of Acetonitrile Filling of Silica Pores of Varying Hydrophilicity/Hydrophobicity. *Langmuir* **2009**, *25*, 1103-1111.

261.   Hu, Z.; Weeks, J. D., Acetonitrile on Silica Surfaces and at Its Liquid-Vapor Interface: Structural Correlations and Collective Dynamics. *J. Phys. Chem. C* **2010**, *114*, 10202-10211.

262.   Loughnane, B. J.; Farrer, R. A.; Fourkas, J. T., Evidence for the Direct Observation of Molecular Exchange of a Liquid at the Solid/Liquid Interface. *J. Phys. Chem. B* **1998**, *102*, 5409-5412.

263.   Loughnane, B. J.; Farrer, R. A.; Scodinu, A.; Fourkas, J. T., Dynamics of a Wetting Liquid in Nanopores: An Optical Kerr Effect Study of the Dynamics of Acetonitrile Confined in Sol-Gel Glasses. *J. Chem. Phys.* **1999**, *111*, 5116-5123.

264.   Morales, C. M.; Thompson, W. H., Simulations of Infrared Spectra of Nanoconfined Liquids: Acetonitrile Confined in Nanoscale, Hydrophilic Silica Pores. *J. Phys. Chem. A* **2009**, *113*, 1922-1933.

265.   Mountain, R. D., Molecular Dynamics Simulation of Water-Acetonitrile Mixtures in a Silica Slit. *J. Phys. Chem. C* **2013**, *117*, 3923-3929.

266.   Iler, R. K., *The Chemistry of Silica: Solubility, Polymerization, Colloid and Surface Properties, and Biochemistry*; New York: Wiley, 1979.

267.   Wang, J.; Chen, C.; Buck, S. M.; Chen, Z., Molecular Chemical Structure on Poly(Methyl Methacrylate) (PMMA) Surface Studied by Sum Frequency Generation (SFG) Vibrational Spectroscopy. *J. Phys. Chem. B* **2001**, *105*, 12118-12125.

268.   Hirose, C.; Akamatsu, N.; Domen, K., Formulas for the Analysis of Surface Sum‐Frequency Generation Spectrum by CH Stretching Modes of Methyl and Methylene Groups. *J. Chem. Phys.* **1992**, *96*, 997-1004.

269.   Hirose, C.; Yamamoto, H.; Akamatsu, N.; Domen, K., Orientation Analysis by Simulation of Vibrational Sum Frequency Generation Spectrum: CH Stretching Bands of the Methyl Group. *J. Phys. Chem.* **1993**, *97*, 10064-10069.

270.   Hatch, S. R.; Polizzotti, R. S.; Dougal, S.; Rabinowitz, P., Surface Vibrational Spectroscopy of the Vapor/Solid and Liquid/Solid Interface of Acetonitrile on ZrO_2. *Chem. Phys. Lett.* **1992**, *196*, 97-102.

271.   Hatch, S. R.; Polizzotti, R. S.; Dougal, S.; Rabinowitz, P., In Situ Surface Vibrational Spectroscopy of the Vapor/Solid and Liquid/Solid Interfaces of Acetonitrile on ZrO_2. *Vac. Sci. Technol.* **1993**, *11*, 2232-2238.

272.   Strunk, M. R.; Williams, C. T., Aliphatic Nitrile Adsorption on Al_2O_3 and ZrO_2 as Studied by Total Internal Reflection Sum-Frequency Spectroscopy. *Langmuir* **2003**, *19*, 9210-9215.

273.   Ostroverkhov, V.; Waychunas, G. A.; Shen, Y. R., Vibrational Spectra of Water at Water/α -Quartz(0001) Interface. *Chem. Phys. Lett.* **2004**, *386*, 144-148.

274.   Darlington, A. K.; Gibbs-Davis, J. M., Bimodal or Trimodal?: The Influence of Starting pH on Site Identity and Distribution at the Low Salt Aqueous/Silica Interface. *J. Phys. Chem. C* **2015**, Early view.

275.   Huang, Y.; Xu, S.; Lin, V. S. Y., Bifunctionalized Mesoporous Materials with Site-Separated Brønsted Acids and Bases: Catalyst for a Two-Step Reaction Sequence. *Angew. Chem. Int. Ed.* **2011**, *50*, 661-664.

276.   Huh, S.; Chen, H.-T.; Wiench, J. W.; Pruski, M.; Lin, V. S. Y., Controlling the Selectivity of Competitive Nitroaldol Condensation by Using a Bifunctionalized Mesoporous Silica Nanosphere-Based Catalytic System. *J. Am. Chem. Soc.* **2004**, *126*, 1010-1011.

277.   Margelefsky, E. L.; Bendjériou, A.; Zeidan, R. K.; Dufaud, V.; Davis, M. E., Nanoscale Organization of Thiol and Arylsulfonic Acid on Silica Leads to a Highly Active and Selective Bifunctional, Heterogeneous Catalyst. *J. Am. Chem. Soc.* **2008**, *130*, 13442-13449.

278.   Margelefsky, E. L.; Zeidan, R. K.; Davis, M. E., Cooperative Catalysis by Silica-Supported Organic Functional Groups. *Chem. Soc. Rev.* **2008**, *37*, 1118-1126.

279. Margelefsky, E. L.; Zeidan, R. K.; Dufaud, V.; Davis, M. E., Organized Surface Functional Groups: Cooperative Catalysis Via Thiol/Sulfonic Acid Pairing. *J. Am. Chem. Soc.* **2007**, *129*, 13691-13697.

280. Sharma, K. K.; Buckley, R. P.; Asefa, T., Optimizing Acid-Base Bifunctional Mesoporous Catalysts for the Henry Reaction: Effects of the Surface Density and Site Isolation of Functional Groups. *Langmuir* **2008**, *24*, 14306-14320.

281. Zeidan, R. K.; Davis, M. E., The Effect of Acid-Base Pairing on Catalysis: An Efficient Acid-Base Functionalized Catalyst for Aldol Condensation. *J. Catal.* **2007**, *247*, 379-382.

282. Zeidan, R. K.; Dufaud, V.; Davis, M. E., Enhanced Cooperative, Catalytic Behavior of Organic Functional Groups by Immobilization. *J. Catal.* **2006**, *239*, 299-306.

283. Zeidan, R. K.; Hwang, S.-J.; Davis, M. E., Multifunctional Heterogeneous Catalysts: SBA-15-Containing Primary Amines and Sulfonic Acids. *Angew. Chem. Int. Ed.* **2006**, *45*, 6332-6335.

284. Heller, A.; Koch, T.; Schmeck, J.; van Ackern, K., Lipid Mediators in Inflammatory Disorders. *Drugs* **1998**, *55*, 487-496.

285. Kassis, J.; Moellinger, J.; Lo, H.; Greenberg, N. M.; Kim, H. G.; Wells, A., A Role for Phospholipase C-γ-Mediated Signaling in Tumor Cell Invasion. *Clin. Cancer Res.* **1999**, *5*, 2251-2260.

286. Anglin, T. C.; Conboy, J. C., Lateral Pressure Dependence of the Phospholipid Transmembrane Diffusion Rate in Planar-Supported Lipid Bilayers. *Biophys. J.* **2008**, *95*, 186-193.

287. Brown, K. L.; Conboy, J. C., Lipid Flip-Flop in Binary Membranes Composed of Phosphatidylserine and Phosphatidylcholine. *J. Phys. Chem. B* **2013**, *117*, 15041-15050.

288.   Conboy, J. C.; Kriech, M. A., Measuring Melittin Binding to Planar Supported Lipid Bilayer by Chiral Second Harmonic Generation. *Anal. Chim. Acta* **2003**, *496*, 143-153.

289.   Liu, J.; Conboy, J. C., Direct Measurement of the Transbilayer Movement of Phospholipids by Sum-Frequency Vibrational Spectroscopy. *J. Am. Chem. Soc.* **2004**, *126*, 8376-8377.

290.   Liu, J.; Conboy, J. C., Structure of a Gel Phase Lipid Bilayer Prepared by the Langmuir-Blodgett/Langmuir-Schaefer Method Characterized by Sum-Frequency Vibrational Spectroscopy. *Langmuir* **2005**, *21*, 9091-9097.

291.   Liu, J.; Conboy, J. C., 1,2-Diacyl-Phosphatidylcholine Flip-Flop Measured Directly by Sum-Frequency Vibrational Spectroscopy. *Biophys. J.* **2005**, *89*, 2522-2532.

292.   Salamon, Z.; Tollin, G., Surface Plasmon Resonance Studies of Complex Formation between Cytochrome C and Bovine Cytochrome C Oxidase Incorporated into a Supported Planar Lipid Bilayer. 1. Binding of Cytochrome C to Cardiolipin/Phosphatidylcholine Membranes in the Absence of Oxidase. *Biophys. J.* **1996**, *71*, 848-857.

293.   Weng, K. C.; Stalgren, J. J. R.; Risbud, S. H.; Frank, C. W., Planar Bilayer Lipid Membranes Supported on Mesoporous Aerogels, Xerogels, and Vycor(R) Glass: An Epifluorescence Microscopy Study. *J. Non-Cryst. Solids* **2004**, *350*, 46-53.

294.   Li, C.; Key, J. A.; Jia, F.; Dandapat, A.; Hur, S.; Cairo, C. W., Practical Labeling Methodology for Choline-Derived Lipids and Applications in Live Cell Fluorescence Imaging. *Photochem. Photobiol.* **2014**, *90*, 686-695.

295.   Bryant, P. A.; Venter, D.; Robins-Browne, R.; Curtis, N., Chips with Everything: DNA Microarrays in Infectious Diseases. *Lancet Infect. Dis.* **2004**, *4*, 100-111.

296.   Sellheyer, K.; Belbin, T. J., DNA Microarrays: From Structural Genomics to Functional Genomics. The Applications of Gene Chips in Dermatology and Dermatopathology. *J. Am. Acad. Dermatol.* **2004**, *51*, 681-692.

297.   Zhang, P. M.; Briones, N.; Liu, C. G.; Brush, C. K.; Powdrill, T.; Belosludtsev, Y.; Hogan, M., Acceleration of Nucleic Acid Hybridization on DNA Microarrays Driven by pH Tunable Modifications. *Nucleos. Nucleot. Nucl.* **2001**, *20*, 1251-1254.